2003

EXPERIMENTAL INVESTIGATION OF SEPARATION IN A LOW PRESSURE TURBINE BLADE CASCADE MODEL

Brian Hollon
University of Kentucky

ABSTRACT OF THESIS

Brian Hollon

The Graduate School
University of Kentucky
2003

EXPERIMENTAL INVESTIGATION OF SEPARATION IN A LOW PRESSURE TURBINE BLADE CASCADE MODEL

ABSTRACT OF THESIS

A thesis submitted in partial fulfillment of the
requirements for the degree of Master of Science
at the University of Kentucky

By

Brian Hollon

Lexington, Kentucky

Director: Dr. Jamey Jacob, Assistant Professor of Mechanical Engineering

Lexington, Kentucky

2003

The flow field around a low pressure turbine blade is examined using smoke-wire flow visualization, static surface pressure measurements, and particle image velocimetry (PIV). The purpose of the experimental study is to investigate the transition and separation characteristics on low pressure turbine blades under low Reynolds number (Re) and varying freestream turbulence intensity (FSTI). A cascade model consisting of 6 Pratt & Whitney PAK-B low pressure turbine blades was examined in a wind tunnel using PIV and flow visualization. Smoke-wire visualization was performed for test section exit angles of 93°, 95°, and 97°, in the range $Re = 3 \cdot 10^4$ to $9 \cdot 10^4$ and three levels of FSTI varied with a passive grid. The locations of separation and transition were determined to be approximately 45% and 77% of the suction surface length, respectively, based upon the smoke stream lines observed in the images, and appear to be independent of Re, turning angle, and FSTI. The maximum size of the separation bubble was found to decrease with increasing Re, turning angle, and FSTI. PIV images from three camera views were processed for an exit angle of 95° and a Re range of $3.0 \cdot 10^4$ to $30.0 \cdot 10^4$ and three levels of FSTI. Velocity, vorticity, and reversed flow probability field plots were generated along with velocity, vorticity, and RMS velocity profiles. The point of separation point was determined to be from 63% SSL to 67% SSL. The area of reversed flow was computed for each image pair from camera views 1 and 3, as an approxiamtion of the relative size of the separation region. For low Re and FSTI cases the area was much larger than for higher FSTI cases at any Re. The raw PIV images include some of the first clear pictures of the turbulent flow structures forming in the unsteady shear layer over the suction surface of low pressure turbine blades. Several movies are compiled that show how the geometry and location of the shear layer evolve in time for a given set of flow conditions.

Keywords: separation, transition, low pressure turbine blade, cascade, PIV (particle image velocimetry)

EXPERIMENTAL INVESTIGATION OF SEPARATION IN A LOW PRESSURE TURBINE BLADE CASCADE MODEL

By

Brian Hollon

(Director of Thesis)

(Director of Graduate Studies)

(Date)

RULES FOR THE USE OF THESIS

Unpublished Thesis submitted for the Doctor's degree and deposited in the University of Kentucky Library are as a rule open for inspection, but are to be used only with due regard to the rights of the authors. Bibliographical references may be noted, but quotations or summaries of parts may be published only with the permission of the author, and with the usual scholarly acknowledgments.

Extensive copying or publication of the thesis in whole or in part requires also the consent of the Dean of The Graduate School of the University of Kentucky.

THESIS

Brian Hollon

The Graduate School
University of Kentucky
2003

EXPERIMENTAL INVESTIGATION OF SEPARATION IN A LOW PRESSURE TURBINE BLADE CASCADE MODEL

THESIS

A thesis submitted in partial fulfillment of the
requirements for the degree of Master of Science
at the University of Kentucky

By

Brian Hollon

Lexington, Kentucky

Director: Dr. Jamey Jacob, Assistant Professor of Mechanical Engineering

Lexington, Kentucky

2003

Brian acknowledges his family, friends, and anyone he ignored when he was working.

Many thanks also for the support of Kentucky NASA EPSCoR under the direction of Drs. Richard and Karen Hackney and the guidance and Dr. David Ashpis of NASA GRC. We would also like to thank Drs. Robert Butler, Chris Murawksi, and Rolf Sondergaard of WPAFB/AFRL for their helpful discussions.

He is eternally grateful to Dr. Jacob for turning his thesis in and dealing with the Graduate School on his behalf.

This work was partially supported by NASA EPSCoR Grant WKU 522635-00-09.

Table of Contents

List of Tables

List of Figures

List of files included with service -

APS-Med.mov 19.5 MB Quicktime movie with smoke visualization and raw PIV images.

piv1-50-15.avi 6.1 MB AVI file.

piv1-50-75.avi 6.4 MB AVI file.

piv1-50-CLN.avi 11.1 MB AVI file.

smoke30-95.avi 992 KB AVI file.

smoke50-95.avi 676 KB AVI file.

smoke60-95.avi 796 KB AVI file.

smoke70-95.avi 828 KB AVI file.

smoke80-95.avi 584 KB AVI file.

smoke90-95.avi 588 KB AVI file.

Chapter 1

Introduction

1.1 Importance of Work

The gas turbine engine has served as the predominant form of aerospace propulsion in the latter half of the 20th century, and increasing performance requirements for gas turbine engines in military and commercial aerospace applications continue to drive development in specific components of gas turbine engines. Small improvements have been shown to result in significant cost savings in the past, particularly in off-design operating conditions where separation becomes a significant factor in performance degradation such as in the low pressure turbine (LPT). Designed for high reynolds number (Re) operating conditions near sea level, the low-pressure turbine section is prone to separation and transition effects at high altitude cruise where low air density results in a reduced Re. There are several parameters that must be studied in order to develop a comprehensive understanding of the flow behavior around the low-pressure turbine blade, including Re, free-stream turbulence intensity (FSTI), blade geometry, and the prevailing pressure gradient. Laminar separation in particular leads to significant degradation of engine performance due to the presence of large re-circulation zones. A turbulent boundary layer, however, is much less likely to separate in the first place, and previous work has shown that turbulent separation bubbles over turbine blades are smaller and have a less drastic effect on performance. The goal of this study is to explore separation on LPT blades using flow visualization and particle image velocimetry (PIV) measurements to gain both a qualitative and quantitative understanding of the parameters that affect it.

1.2 Previous Work

The following sections summarize previous research on low pressure turbine blades as well as the methodology of smoke-wire flow visualization and PIV.

1.2.1 Low Pressure Turbine Blades

Experiments on LPT blades typically consist of 2-D cascades of 3 or more blades. Difficulties typically arise in control and measurement of flow parameters such as FSTI and exit angle, both of which affect the pressure distribution along a blade's surface. Several studies have guided us in the design and focus of our own experiments.

Mayle reviewed the importance of laminar-to-turbulent transition with respect to gas turbine engine design [9]. He suggested a range of Re from $\mathcal{O}(10^6)$ at the engine inlet to as low as $\mathcal{O}(10^4)$ in the turbine section. Mayle concluded that transition plays a major role in the flow behavior on both sides of a turbine blade, and described several modes of transition and their relation to gas turbine engine design.

Dorney *et al.* examined losses in an 8-blade LPT cascade over a range of Re experimentally and numerically and found increased losses at lower Re due to separation [4]. Illustrating the potential for improvement even at lower Re conditions, the losses were significantly reduced by implementing a trip wire placed on the suction surface of the blade such that the flow remained attached in the region where the flow separated for the same conditions with no trip-wire.

Halstead *et al.* conducted an experimental study of boundary layer flows in a simulated low-pressure turbine section with hot-wire probes [6, 7]. They observed large regions of laminar and transitional flow on the suction surface of the blades. In the wake-induced path entering the nozzle, FSTI was observed from about 1.5% to 2.5-3%, and they found regions of suppressed separation downstream of the turbulent wakes.

Baughn *et al.* also explored the effect of FSTI [3]. Varying the level of FSTI from 1% to 10%, they found that the transition point moved forward with an increase in FSTI. Qiu and Simon investigated transition on the suction side of a turbine blade with hot-wire probes for varying FSTI and Re [12]. They found that increasing Re and/or FSTI resulted in a smaller separation bubble and also prompted earlier transition.

Murawski *et al.* have also conducted experiments on a turbine blade cascade and have observed similar flow behavior in a Re range of 50,000 to 300,000 and FSTI levels of 1.1% and 8.1% [10, 11]. They have explored the effect of trailing edge extensions on blades which alter the upstream pressure gradient and found that up to 6.1% of axial chord, extensions resulted in a marked increase in overall

efficiency. Volino and Hultgren studied flow over a flat plate in a wind tunnel using a contoured upper wall with suction to impose a pressure gradient with the typical PAK-B profile [17]. Using a single-sensor hot-wire probe to measure stream-wise velocity, velocity profiles were obtained at 14 stations on the plate for Re values of 50,000, 100,000, 200,000, and 300,000, and FSTI levels of 0.2% and 7% as controlled with passive turbulence grids. Transition occurred at between 63% and 67% of the suction surface length with increasing Re. They found that Re and FSTI are not a factor with respect to the boundary layer separation unless they are large enough to induce transition upstream of separation. The size and location of the transition region were however found to vary significantly with Re and FSTI. Reattachment is never observed before transition for these cases.

In the current paper, we have attempted to recreate the parameter spaces studied by the previously mentioned studies to allow for comparison of flow visualization and PIV measurements with the published hot-wire measurements [11, 12].

1.2.2 Smoke Wire Flow Visualization

Batill and Mueller used the smoke-wire technique to visualize flow over an airfoil mounted between two end plates in a wind tunnel [2]. A 50 V power source heated stainless steel and tungsten wires with diameters from 0.001 inches to 0.006 inches coated with mineral oil. The local Re number based upon wire diameter was maintained below 20 to avoid 3-D effects in the wire wake. The wires were also pre-stressed to account for sagging during the heating of the wires as the voltage was applied. The most effective liquid used to coat the wire was a model train smoke product consisting of mineral oil, oil of anise and blue dye. The lighting, coating, heating and photography were synchronized with a timing/control circuit. The result was high contrast images of uniform smoke streak-lines over the airfoil, that were used to visualize the boundary layer and the location of transition. The flow visualization experiments in the current study were setup according to the wind tunnel tests of Batill and Mueller, although the timing was controlled manually.

Sieverding and Van Den Bosche have also used smoke in flow visualization experiments of turbine blade flows [14]. The use of several different colors of smoke streak-lines allowed for the visualization of secondary flows at the end walls of a turbine blade cascade. Complex 3-D flow patterns such as leading edge horseshoe vortices were clearly observed through the use of the colored smoke filaments. The experiments presented here focus on 2-D flow characteristics, and white smoke is used herein.

1.2.3 PIV Measurements

PIV (Particle Image Velocimetry) has become a common method for determining the instantaneous velocities of particles in a seeded fluid. The PIV algorithm used herein utilizes the wall adaptive Lagrangian parcel-tracking algorithm (WaLPT) developed by Sholl and Savaş [15]. This algorithm tracks the seeding as fluid parcels and determines their translations and deformations. Fluid parcels registered by CCD pixels are advected with individually estimated velocities and total accelerations. A standard DPIV algorithm is employed to determine the initial velocity field, and the routines in WaLPT allow for accurate measurement of the velocities near the blade surface by essentially mirroring the flow about the wall using an image parity exchange routine [16]. This method has previously been used to examine separation regions on turbine blade models in a tow tank [8].

1.3 Current Study & Outline of Thesis

The study conducted in the Fluid Meschanics Laboratory at the University of Kentucky consists of smoke-wire flow visualization and PIV measurements of flow over a 6-blade cascade of Pratt & Whitney PAK-B turbine blade models mounted in a low-speed wind tunnel with variable exit angle. Pressure measurements for the same test section configurations are also presented for comparison to the flow visualization experiments. The methods employed for the experiments facilitate instantaneous measurements of the unsteady flow field about the blade. This study focuses on the separation region over the suction surface of the LPT, primarily the re-circulating region. The flow field measurements obtained offer a greater understanding of the effects of Re, exit angle and FSTI on the geometry and location of the separation bubble, and novel visualization of unsteady characteristics within the separation region.

The thesis presents first the theoretical background of separated flows over typical turbine blade geometry, including laminar and turbulent boundary layer separation, and how the flow transitions and reattaches to the blade surface in Chapter 2. A detailed description of the experimental design and execution is then presented for flow visualization, pressure, and PIV measurements in Chapter 3. In Chapter 4, the data and results from the flow visualization and pressure measurements is discussed, followed by a detailed discussion of the PIV study in Chapter 5. In Chapter 6, a comparison of these studies with previous work and a summary of possible improvements for future experiments concludes the main body of the thesis. Some discussion of a preliminary PIV study carried out in a tow tank is included along with a method of generating turbine blade pressure

coefficients over a single airfoil in the appendices.

Chapter 2

Theory

This chapter briefly covers some of the theoretical aspects related to this project. The first section discusses the specific operating regimes where separation is likely to occur on a low pressure turbine blade. The second section deals with theoretical considerations of separation, particularly the difference between separation of laminar and turbulent boundary layers and how separated flow transitions and reattaches to the blade.

2.1 Turbine Blade Regimes of Interest

Turbine blades, unlike their counterpart foils in the compressor section of a gas turbine engine, remove pressure from the generated work and thus tend to operate under a favorable pressure gradient. Consequently, high turning angles are possible without significant separation. This typically results in fewer stages than found in a compressor section. (These extreme angles also lead to large loads on the blades which is another significant factor in turbine blade design.) In the case of a low pressure turbine, which drives the fan section of a high bypass jet engine, the pressure decrease is less than that found in high pressure turbine cascades and separation is more likely to occur.

Consider a low pressure turbine blade with an axial chord of 10 cm (about 4 inches), a large but not uncommon size for a turbine blade. If the flow in the turbine section is 100 m/s and the density is approximately that of atmospheric (about 1 kg/m^3) and $\nu = 2 \cdot 10^{-5}$m^2/s, then the Reynolds number based on axial chord becomes 500,000. At high altitudes, density can drop by an order of magnitude thus reducing the axial chord to 50,000, all things remaining equal. Thus, a turbine blade may have a Reynolds number operating range of an order of magnitude or more. As is typical in low Re aerodynamics, separation becomes a significant concern as Re drops below

values of $\mathcal{O}(10^5)$. Particular importance is paid to separation on a low pressure turbine blade and it has been well studied from a variety of standpoints, as discussed in Chapter 1. (For a good discussion of Reynolds number regimes for various components of a gas turbine engine, see Mayle [9]).

2.2 Boundary Layer Separation

Separated flow over the suction surfaces of low pressure turbine blades due to adverse pressure gradients results in a degradation in engine performance. Especially in cases where the separated flow never reattaches to the blade surface, the loss of lift can be significant; the associated losses have been estimated from 2% to 7%, depending upon the conditions of operation [17]. The following sections discuss the mathematical foundations for a study of the separation physics on low pressure turbine blades.

2.2.1 Laminar versus Turbulent Flow & the Effect of Pressure Gradient

The best known instance of separation is that over a flat plate. It has been well studied for many years, first by Prandtl and later by Blasius (see Batchelor or Schlicting for detailed treatments [1, 13]). In the case of a flat plate with zero pressure gradient, the boundary layer can be quantified analytically. In the absence of other information, the boundary layer over many bodies in the presence of a zero pressure gradient can be assumed to behave similar to that as a flat plate with good results. The growth of a laminar boundary layer over a flat plate can be shown to be

$$\delta/x = 5/\sqrt{Re_x} \tag{2.1}$$

while a turbulent boundary layer growth on a flat plate is given by

$$\delta/x = 0.37/Re_x^{0.2} \tag{2.2}$$

where $\delta = y(u = 0.99u_e)$ and $Re_x = Ux/\nu$, the local Reynolds number [13]. At some value of Re_x, the boundary layer will transition from laminar to turbulent flow.

Separation on a flat plate is a special case of a more general problem since a flat plate has a zero pressure gradient. More often, the flow separates due to the presence of an adverse pressure gradient which facilitates separation. This is a common occurance over any body, bluff or streamlined, since flow over any body must first accelerate and then decelerate, resulting in first a favorable and then an adverse pressure gradient. It is this problem that aerodynamicists have been attempting to solve since the invention of the airfoil.

The effect of pressure gradient on separation is particularly important and can be illustrated as follows. The boundary layer equation in the region of interest is given by

$$u\frac{\partial u}{\partial x} + v\frac{\partial u}{\partial y} = -(1/\rho)\frac{\partial p}{\partial x} + \nu\frac{\partial^2 u}{\partial y^2} \tag{2.3}$$

where negligible terms in the Navier-Stokes equations have been eliminated. The pressure gradient can be determined from the external velocity field, since it will remain constant throughout the boundary layer normal to the surface, by the relation

$$\frac{dp}{ds} = -\rho U\frac{du_e}{ds} \tag{2.4}$$

where s is along the surface of the turbine blade so that $s = x$, and u_e is the velocity at the edge of the viscous region. At the blade surface, where $y = 0$, the boundary layer equation becomes

$$\mu\frac{\partial^2 u}{\partial y^2}|_{y=0} = \frac{\partial p}{\partial x} \tag{2.5}$$

or

$$\mu\frac{\partial^2 u}{\partial y^2}|_{y=0} = -\rho u_e\frac{du_e}{dx} \tag{2.6}$$

so that the sign of $\partial^2 u/\partial y^2$ is dependent upon the sign of du_e/dx. Thus, when the flow is accelerating, $du_e/dx < 0$ and hence $dp/dx < 0$. This pressure gradient is *favorable* since

$$\frac{\partial^2 u}{\partial y^2}|_{y=0} < 0 \tag{2.7}$$

and the external velocity profile blends in smoothly with that near the wall and $\partial^2 u/\partial y^2 < 0$ throughout the flow field. When the flow is decelerating, however, $du_e/dx > 0$ and $dp/dx > 0$ and the pressure gradient is *adverse*. At the surface then,

$$\frac{\partial^2 u}{\partial y^2}|_{y=0} > 0 \tag{2.8}$$

but as $\partial^2 u/\partial y^2 < 0$ away from the wall, there must be an inflection point somewhere in the flow where $\partial^2 u/\partial y^2 = 0$. This results in a rapid increase in boundary layer thickness due to both viscous diffusion and advection.

If given enough time, a flow under an adverse pressure gradient will always separate, resulting in a region of reversed flow. The point of separation is determined by

$$\frac{\partial u}{\partial y}|_{y=0} = 0 \tag{2.9}$$

where the shear stress at the wall vanishes and then reverses sign. A laminar boundary layer, given the characteristic parabolic profile, is more likely to separate than a turbulent boundary layer. The

turbulent boundary layer velocity profile, in contrast to that of a laminar boundary layer, is steeper near the wall and thus requires more time for an inflection point to develop into separated flow. Physically, the turbulent boundary has more energy than its laminar counterpart and can thus resist separation more readily. The downside, however, is that since the velocity gradient du/dy is steeper in a turbulent boundary layer, it results in a higher skin friction coefficient.

Once a boundary layer has separated, it forms a separation bubble by reattaching to the wall. At sufficiently low Reynolds numbers the flow may never reattach to the blade surface, but the flow typically transitions to turbulent flow (if the boundary layer is laminar) which quickly reattaches. This is shown in Figure 2.1. If the boundary layer is already turbulent and still happens to separate, then the flow will usually reattach rather rapidly. Transition Reynolds number is a function of freestream turbulence intensity (FSTI) as well as local surface geometry (roughness and curvature, for example). There is no accurate method of predicting transition, separation, and reattachment in a generic flow, though some methods are accurate once properly tuned (see Young, for example [18]).

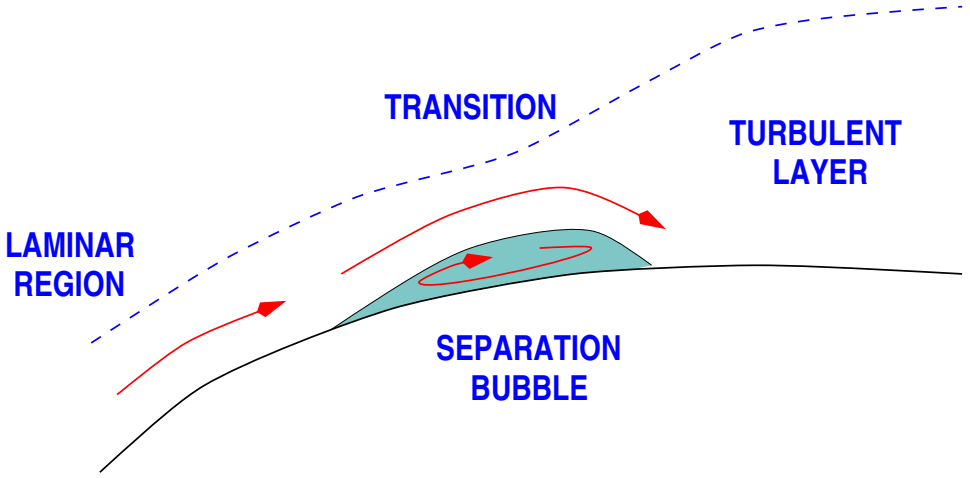

Figure 2.1: Cartoon of separation, transition and reattachment in a laminar boundary layer.

Chapter 3

Experimental Arrangement

3.1 Test Facilities

The experiments were conducted in the Low-Speed Wind Tunnel (LSWT), which is a low-turbulence, open-circuit, blow-down wind tunnel with a computer controlled, 7.5 hp motor driving a radial fan. Upstream of the nozzle, a vibration damper, flow straightener and turbulence damping screens condition the flow. The nozzle has a contraction ratio of 6.7, and the test section has a cross-section of 0.2 m×0.4 m. The test section is constructed from 1/4" thick clear polycarbonate, with movable exit walls that allow for variations in the exit angle, β, from 80° to 100° as illustrated in Figure 3.1. A movable grid can be placed upstream of the blade region to generate higher turbulence intensities. The grid consists of 9 vertical and 5 horizontal square polycarbonate ribs that are 9.525 mm wide and spaced 38.1 mm apart. Placed at 190 mm (1.25% SSL) and 380 mm (2.5% SSL) upstream, the grid generates approximately 10% and 5% FSTI, respectively at the leading edge of the test blade, though these values are not verified, while the nominal FSTI without the grid was measured to be $\sim 0.5\%$. For simplicity, the three FSTI conditions are referred to throughout in the figures and text as test case A, B, and C, in order of increasing FSTI and are shown in Figure 3.3. The maximum velocity in the test section is 35 m/s, resulting in a maximum Re_{SSL} of approximately $3 \cdot 10^5$ based on exit velocity and suction surface length (SSL).

3.2 Turbine Blade Models & Pressure Measurements

A set of identical turbine blade models with a chord length of 114 mm, a span of 203 mm and a suction surface length of 152 mm have been constructed using a stereo-lithography apparatus (SLA). The Pratt & Whitney PAK-B profile is used for the blade geometry. Six blade models

were produced for the wind tunnel cascade as shown in Figure 3.2 and placed in the test section to provide a nominal exit angle of 95°. For pressure measurements along the suction surface of the blade, another SLA model was constructed with 24 pressure tap stations at mid-span as shown in Figure 3.4. Static pressure on the blade was measured with a transducer with a range of ±0.5 inches H_20. 4000 data points were recorded at a sampling rate of 50 Hz for each run. The pressure coefficient is determined using the relation

$$C_p = \frac{\triangle p}{1/2\rho_{\text{air}} U_{\text{exit}}^2} = \frac{p - p_{\text{ref}}}{1/2\rho_{\text{air}} U_{\text{exit}}^2} \tag{3.1}$$

where the static reference pressure p_{ref} was measured at the entrance of the test section approximately 800 mm upstream of the instrumented location, and U_{exit} is the velocity at the exit of the test section as measured with a pitot probe. Some difficulty in keeping the small holes and passages clear in the SLA material resulted in inconsistent readings in three of the taps, and inaccurate measurements due to blocked taps are omitted from the plots of pressure included in Chapter 4.

3.3 Smoke-wire Flow Visualization

Flow visualization is utilized in the tunnel to obtain qualitative information about the separation region. The smoke wire technique as described previously is setup in the wind tunnel as shown in Figure 3.1. A 0.005 inch steel wire is stretched across the tunnel section and coated with a dyed oil, as described by Batill and Mueller [2]. The wire is heated using a 50 VDC supply and fine streaks of smoke are momentarily produced. The flow speed is limited by the wire Re_d which must be kept low (typically $Re_d < 50$) to prevent shedding. A camera and illumination source are positioned to isolate a 2 dimensional region of interest at mid-span of the test blade. The flow is illuminated from the side using a 750 W lamp and the streak-lines are digitally recorded with a CCD camera and frame grabbing software connected to a PC in real-time. The frame grabbing software used to capture image pairs is XCAP v.2.1 (EPIX, Inc.). Resulting movies made from the captured images may be used to deduce the separation location and separation bubble size. Since the upstream flow is nominally laminar, the point at which the streak-lines nearest the surface begin to break down may be used to determine the transition location. In the increased FSTI cases, the grid resulted in diffusion of the smoke streak-lines at lower flow speeds, further constraining the Re range for the flow visualization experiments.

3.4 PIV Measurements

The configuration of the equipment used to acquire PIV measurements is essentially the same as shown in Figure 3.1, but the light bulb is replaced with a laser sheet. The flow is seeded upstream of the tunnel inlet with smoke particles on the order of 1 micron in diameter. A 2-D light sheet is projected in the plane of the tunnel at the mid-span blade height using a dual-head Nd:YAG laser from New Wave Research pulsed in sync with a 50 mJ/pulse Kodak Megaplus ES 1.0 10-bit CCD camera, with 1018×1008 pixels resolution and double trigger capability, using a timing control unit from Taitech allowing image timing from 10 μs to 1 ms. The camera is placed at three locations above the cascade resulting in three flow regions covering the last half of the test blade as shown in Figure 3.5. The first camera view covers the length of the blade from about 40% SSL to 70% SSL, the second from about 53% SSL to 84% SSL, and the third from about 73% SSL to 103% SSL. Epix frame grabbing hardware and software is used to acquire binary image pairs for processing using the algorithm as discussed previously. For each run, 112 images were captured at a time at a rate of 10 Hz and the velocity and vorticity fields obtained in post-processing were ensemble averaged.

Velocity and vorticity are calculated as part of the PIV algorithm and are scaled accordingly; vorticity is determined spectrally and does not suffer from typical numerical differentiation problems [15]. In post-processing, the forward flow probability (FFP) or reversed flow probability (RFP) are determined by examining the percentage of time a vector is facing forward (downstream) or backward (upstream), respectively. For $FFP = 1$, the vector is facing downstream 100% of the time regardless of the value of the vertical velocity component. For $FFP = 0$, the vector is facing upstream 100% of the time. Mathematically, this can be written for a single point as

$$\text{FFP} = \frac{1}{N}\sum_{1}^{N}\frac{\mathbf{u}}{|\mathbf{u}|} \tag{3.2}$$

where N is the total number of realized velocity fields. FFP and RFP values, different only in sign and not magnitude as based upon direction, may be used interchangeably to determine where the flow is most often reattaching at the wall, and also to study the unsteadiness of the flow. A value of $FFP = 0.5$ would indicate maximum unsteadiness by this criterion.

A rough estimate of the turbulence intensity of the flow is determined by the RMS (root mean square) velocity, as determined by the relation

$$\text{rms} = \frac{1}{N}\sqrt{\Sigma(\mathbf{u}')^2} \tag{3.3}$$

where N in this case is the number of acquired velocity fields and $\mathbf{u}'$ is the unsteady velocity

component as given by

$$\mathbf{u} = \mathbf{U} + \mathbf{u}' \tag{3.4}$$

where $\mathbf{U}$ is the time-averaged velocity. As a caveat, it should be noted that since the PIV measurements are taken at a nominal sampling rate of 10 Hz, any measure of turbulence will be under-resolved. This calculation does provide accurate measurements of the variation in the velocity over a moderate time scale, however.

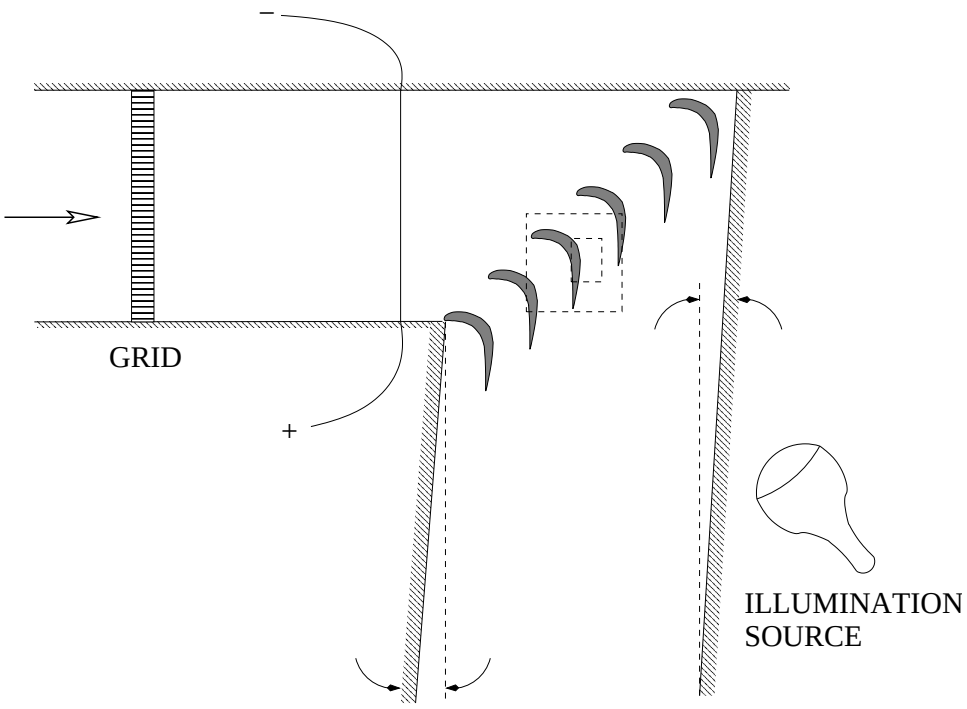

Figure 3.1: Wind tunnel test section with smoke-wire setup illustration.

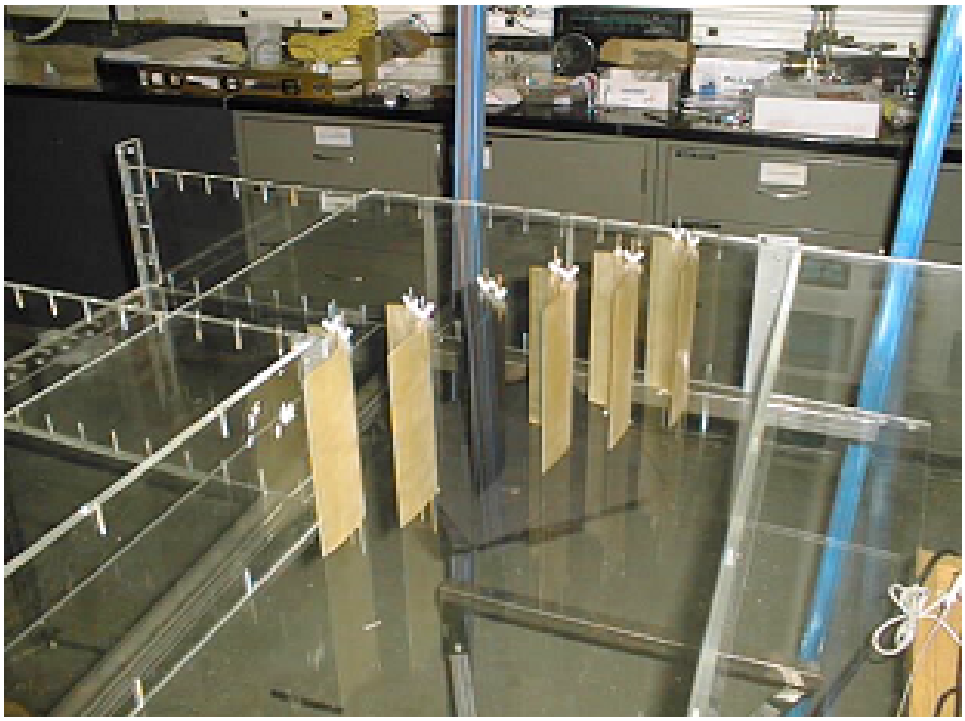

Figure 3.2: Wind tunnel test section with adjustable turning angle and 6 blade cascade.

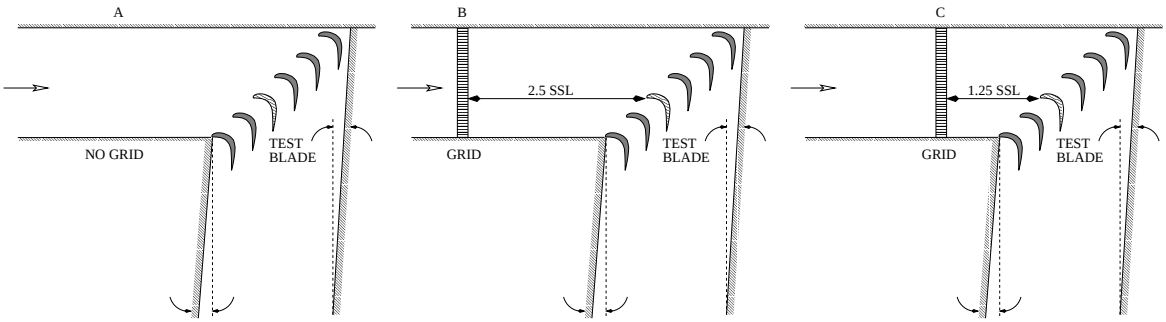

(a) Case A (b) Case B (c) Case C

Figure 3.3: Three test section configurations for varying FSTI levels.

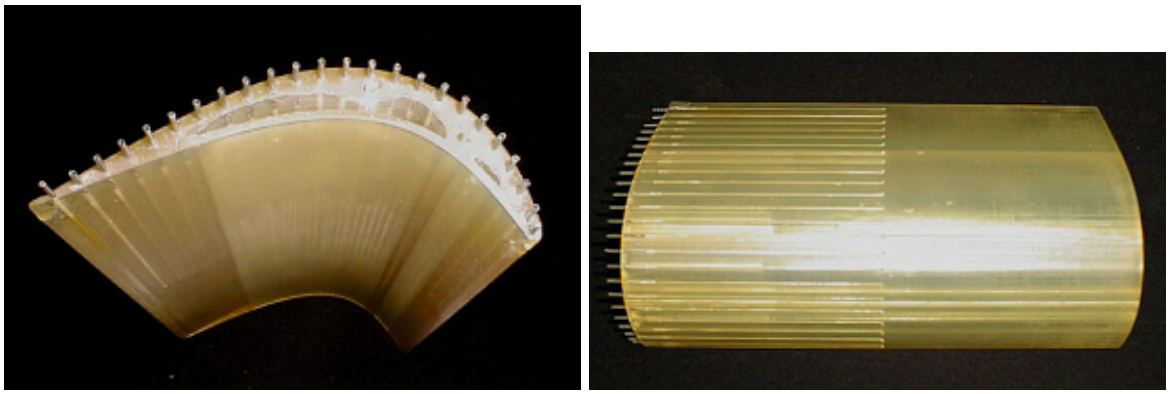

(a) (b)

Figure 3.4: SLA PAK-B turbine blade model with 24 pressure taps

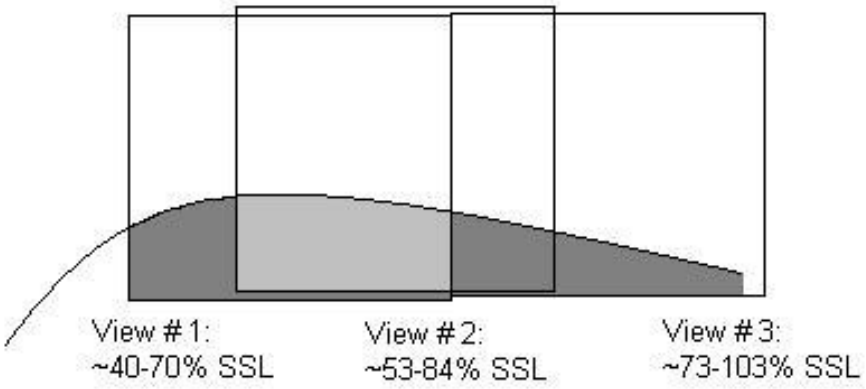

Figure 3.5: Three camera views and relative position over blade for PIV.

Chapter 4

Flow Visualization & Pressure Measurements

4.1 Results

4.1.1 Data Acquisition

In the preliminary smoke-wire runs Re is varied from $1.0 \cdot 10^4$ to $9.5 \cdot 10^4$ in increments of 5000, with an exit angle of 95° in the clean tunnel (no turbulence generating grid), corresponding to a FSTI of approximately 0.5%. These first images were used to determine optimal camera angle and lighting as well as the practical Re range for the flow visualization images. The frequency invertor on the wind tunnel motor is not consistent below 5 Hz, corresponding to a Re of $1.0 \cdot 10^4$; above a Re of $9.0 \cdot 10^4$ the streamlines begin to diffuse so that individual smoke streaks are indistinguishable. The Re range for the flow visualization and supporting pressure measurement experiments is therefore limited to $1.0 \cdot 10^4$ to $9.0 \cdot 10^4$.

The clean tunnel experiments for Re from $1.0 \cdot 10^4$ to $9.0 \cdot 10^4$ in increments of $1.0 \cdot 10^4$ with the adjusted camera yield high quality images. These conditions are studied for exit angles of 93°, 95° and 97°. For each run 60 images are acquired of which 5 to 10 images with clear streak-lines are recorded and saved. A second set of flow visualization experiments includes the addition of the turbulence generating grid upstream of the test blade. Varying Re from $1.0 \cdot 10^4$ to $9.0 \cdot 10^4$ and holding β at 95 degrees, smoke images are acquired for each of the three turbulence grid configuarations shown in Figure 3.3. Selected images for variable β are shown in Figures 4.1, 4.2, 4.3, and 4.4 while images for variable FSTI are shown in Figure 4.5.

Static pressure measurements are presented as acquired in the wind tunnel with a test blade

designed with 24 pressure taps spaced evenly along mid-span of the blade. Static pressure measurements are presented for Re of $10.0 \cdot 10^4$, $20.0 \cdot 10^4$, and $30.0 \cdot 10^4$ and β of 93°, 95°, and 97° in a clean tunnel, to compare with the clean smoke-wire experiments. The pressure coefficient is determined and plotted in Figures 4.6(a), 4.6(b), and 4.6(c).

4.2 Discussion

After proper adjustments of lighting and camera position, images of very clear smoke streaks tracing the flow over the cascade may be obtained at a capture rate of 30 Hz. In a typical image of highest smoke content, around 15 streak-lines are observed between the test blade and the pressure side of the next blade in the cascade. These images are then loaded in a photo editor and contrast and brightness adjusted for optimal clarity. With increasing Re there are fewer images from a given run with distinct streamlines, and the quality of those images is also poorer due to increased diffusion. Even with the turbulence grid placed 380 mm upstream, however, the separation region is visible.

The smoke wire images from the wind tunnel runs are shown in Figures 4.1 through 4.5. The sequences are arranged with increasing Re_{SSL} from $3.0 \cdot 10^4$ to $9.0 \cdot 10^4$ for exit angles of 93°, 95° and 97°, respectively, in Figures 4.1, 4.2, and 4.3. An approximate scale for the suction surface length is overlayed on one image from each run for analysis as shown in Figure 4.4.

Two trends are noted from the flow visualization. As Re is increased, the separation region decreases in size. A monotonic decrease in the region of separation height at a particular Re with an increase in the exit angle is also observed as shown in the averaged values in Table 4.1. The trend clearly shows the effect of the higher turning angle on the size of the separation region. There is little observed movement of the points of separation and transition over the entire range as discussed below.

The location of separation is difficult to pin down based upon the smoke-wire images, because most runs in the clean tunnel result in only a couple images with a clear streak line defining the boundary of the separation region. When several images from a given run show a clear separation point, the values are averaged and non-dimensionalized by the suction surface length. The transition point is also a somewhat amorphous entity in the smoke images. The breakdown of a smoke-streak close to the wall is considered to be the location of the onset of transition. Based upon observation of the smoke streaks, this breakdown point moves upstream and downstream, and also toward and away from the blade wall for a given run. The size of the separation region is also determined by measuring the distance to the nearest streamline at the point of transition. Viewing the images

from a run in an animator also makes it possible to observe reversed flow within the separation region. Toward the end of a run, diffused smoke from the transition region is often drawn back upstream into the separation region. The reversed smoke narrows as it flows toward the separation point and then dissipates.

For the clean tunnel flow visualization runs, the location of separation is approximately 57% SSL for all Re and exit angles tested. The transition point seems to vary independent of these parameters as well, consistently between 70% and 78% SSL for all runs. Only the size of the separation region suggests a clear trend. With increasing exit angle, the size of the separation region decreases. For a given exit angle, the size of the separation region further decreases with increasing Re. The largest separation region observed is 8.3% SSL for $Re = 3 \cdot 10^4$ at both $\beta = 93°$ and $\beta = 95°$, and the smallest is 3.1% SSL for $Re = 3 \cdot 10^4$ at $\beta = 97°$. These values are presented in Table 4.1.

With the grid placed 380 mm upstream of the cascade, the smoke streamlines shown in Figure 4.5 show the size of the separation region to be decreased by the increased FSTI, from a clean value of 8.3% SSL to 6.25% SSL. The partial diffusion of the smoke streaks due to the increased FSTI makes transition and separation more difficult to track, but the images do not appear to indicate significant movement of the location of transition for increased FSTI at $Re = 3 \cdot 10^4$. The separation point, however, moves upstream with the increased FSTI to approximately 45% SSL. With the turbulence grid placed 190 mm upstream of the cascade, the smoke streak-lines diffuse into one sheet over the suction surface, essentially hiding any flow structures observed in the lower FSTI cases.

The plots generated from the static pressure measurements on the surface of the blade are shown in Figures 4.6(a), 4.6(b), and 4.6(c). An XFoil calculation at these low Re numbers indicates a similar break from the design curve anmd is discussed in more detail in Appendix B. A sharp drop immediately followed by a plateau behind the point of maximum pressure coefficient indicates the location of separation near 60% SSL. The subsequent descent toward the theoretical pressure distribution near the trailing edge of the blade suggests the flow may be approaching reattachment, though the plots do not fully recover to the theoretical curve. As suggested by the smoke-wire flow visualization runs, separation as determined from the pressure distribution occurs near 60% SSL for $Re = 10 \cdot 10^4$, $20 \cdot 10^4$, and $30 \cdot 10^4$ for each of the exit angles tested. (Only 95° is shown in the plots. Note that C_p could not be accurately measured for $Re < 10 \cdot 10^4$ due to the low static pressures encountered and low sensitivity and resolution of the pressure transducer used in the experiment.)

Re	Separation Height in % SSL		
$\cdot 10^4$	$\beta = 93°$	$\beta = 95°$	$\beta = 97°$
3	8.25	8.25	6.25
5	7.4	7.4	5.7
6	6.75	5.7	5.2
7	5.75	5.6	5.2
8	5.25	4.75	4.25
9	4.7	4.25	3.1

Table 4.1: Separation thickness in terms of SSL for the clean tunnel (case A) flow visualization runs.

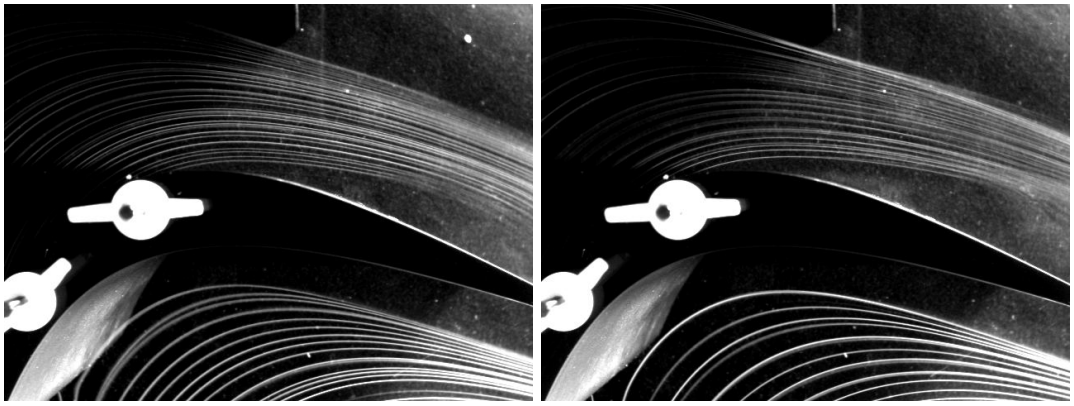

(a) $Re_{SSL} = 3 \cdot 10^4$.

(b) $Re_{SSL} = 5 \cdot 10^4$.

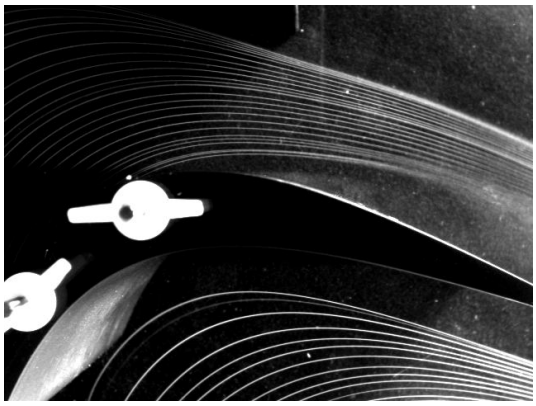

(c) $Re_{SSL} = 6 \cdot 10^4$.

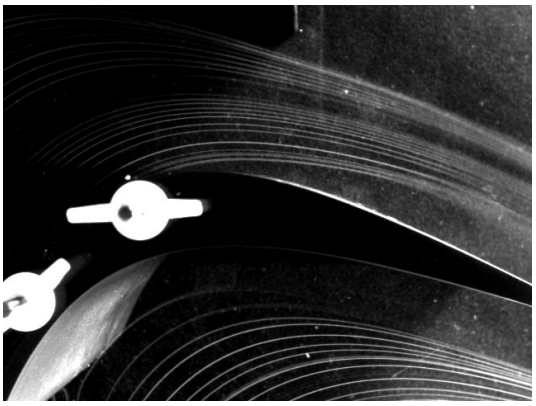

(d) $Re_{SSL} = 7 \cdot 10^4$.

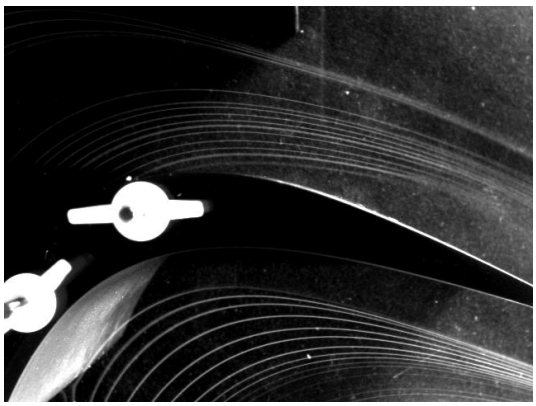

(e) $Re_{SSL} = 8 \cdot 10^4$.

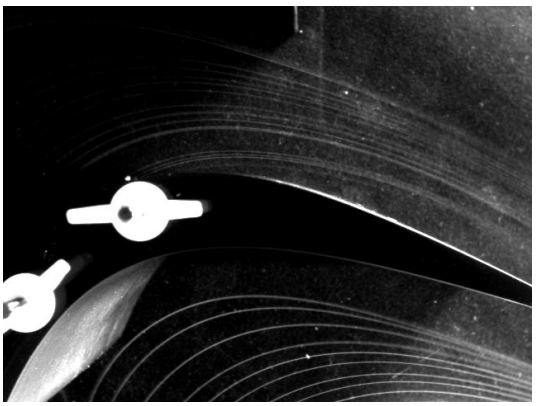

(f) $Re_{SSL} = 9 \cdot 10^4$.

Figure 4.1: Images of separation region for various Re at $\beta = 93°$ and FSTI case A.

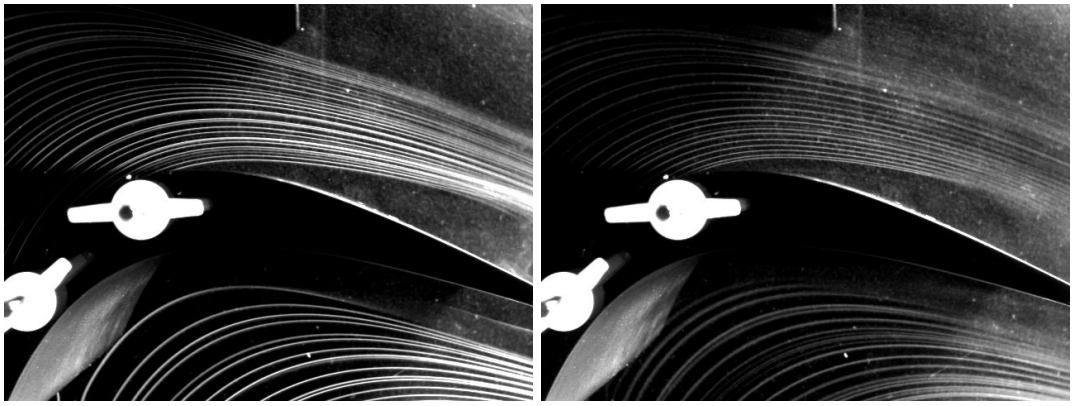

(a) $Re_{SSL} = 3 \cdot 10^4$.

(b) $Re_{SSL} = 5 \cdot 10^4$.

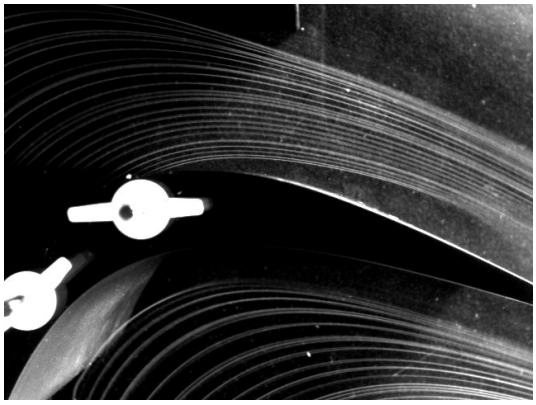

(c) $Re_{SSL} = 6 \cdot 10^4$.

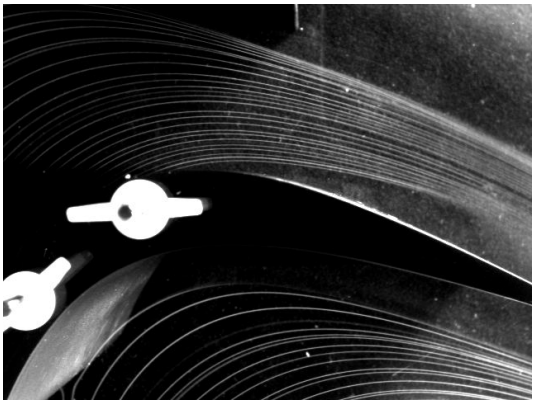

(d) $Re_{SSL} = 7 \cdot 10^4$.

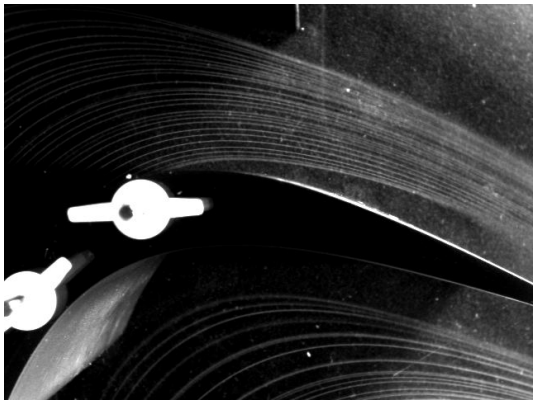

(e) $Re_{SSL} = 8 \cdot 10^4$.

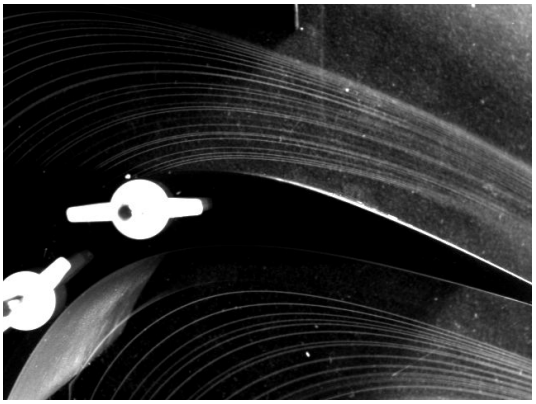

(f) $Re_{SSL} = 9 \cdot 10^4$.

Figure 4.2: Images of separation region for various Re at $\beta = 95°$ and FSTI case A.

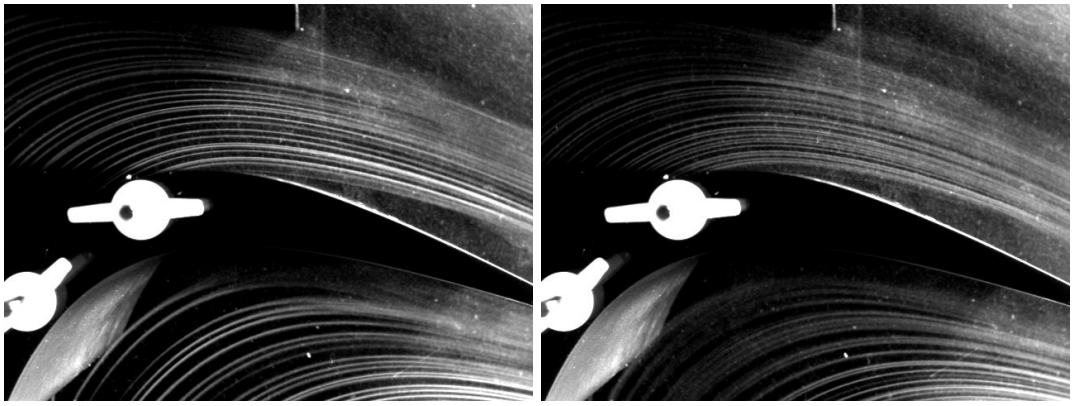

(a) $Re_{SSL} = 3 \cdot 10^4$.

(b) $Re_{SSL} = 5 \cdot 10^4$.

(c) $Re_{SSL} = 6 \cdot 10^4$.

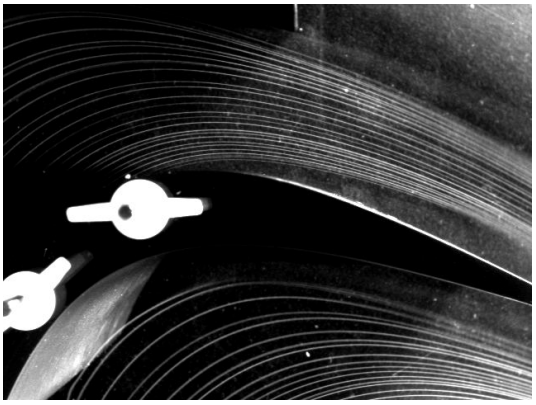

(d) $Re_{SSL} = 7 \cdot 10^4$.

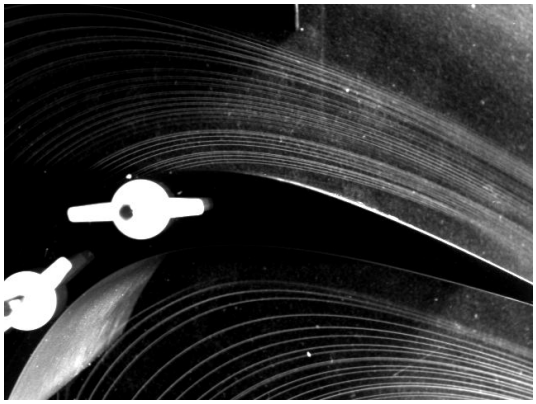

(e) $Re_{SSL} = 8 \cdot 10^4$.

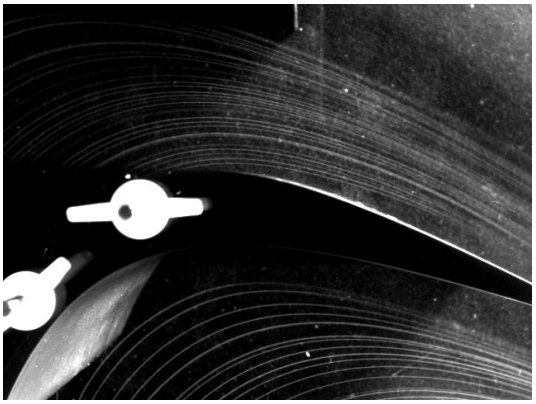

(f) $Re_{SSL} = 9 \cdot 10^4$.

Figure 4.3: Images of separation region for various Re at $\beta = 97°$ and FSTI case A.

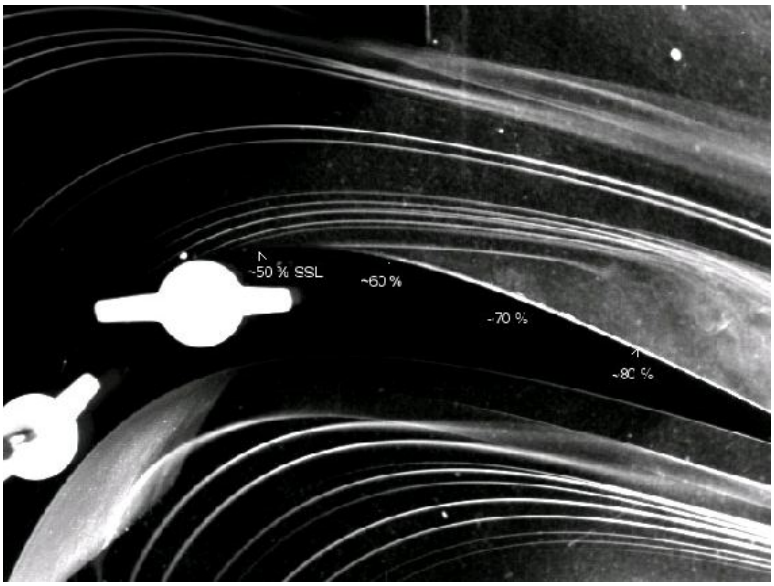

(a) $\beta = 93°$.

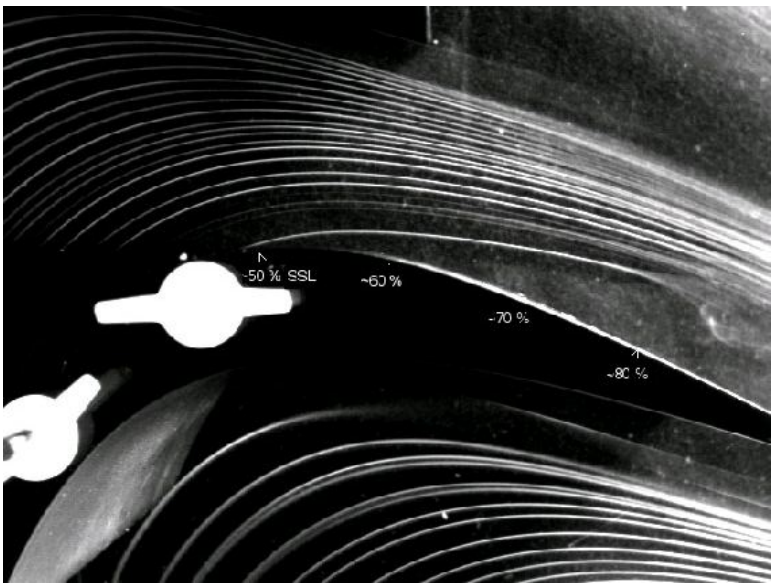

(b) $\beta = 95°$.

Figure 4.4: Comparison of 2 runs at $Re = 3 \cdot 10^4$ and FSTI case A. Note that the $\beta = 93°$ case clearly transitions first.

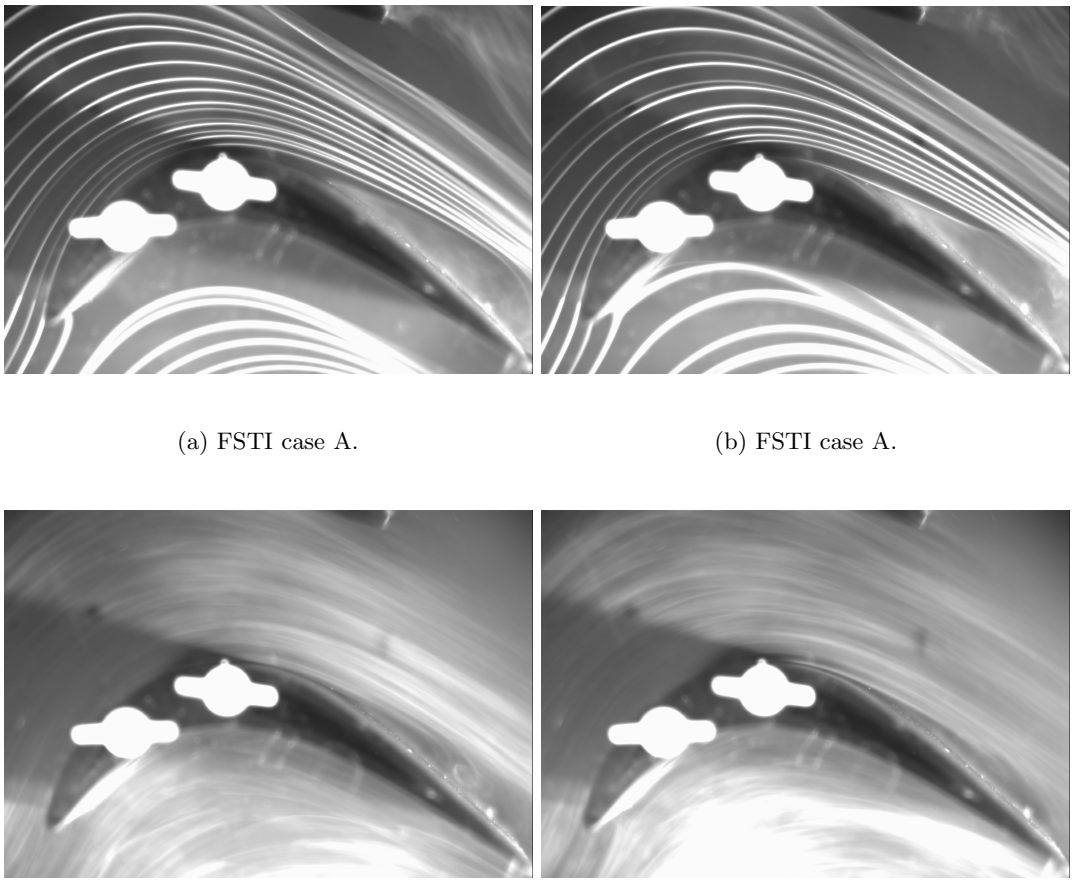

(a) FSTI case A.

(b) FSTI case A.

(c) FSTI case B.

(d) FSTI case B.

Figure 4.5: Comparison of 2 runs at $Re = 3 \cdot 10^4$ for two different turbulence intensities.

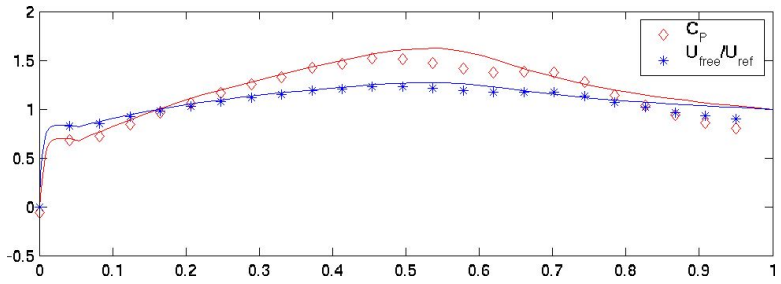

(a) $Re = 100,000$.

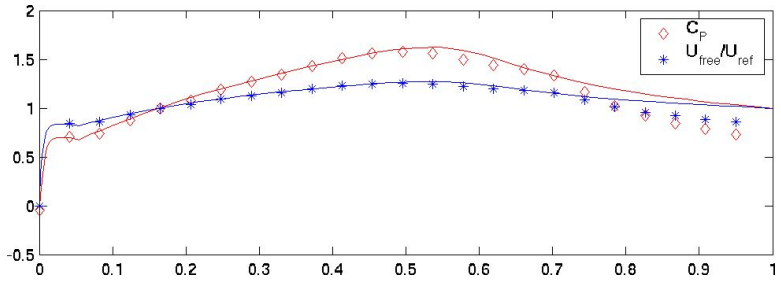

(b) $Re = 200,000$.

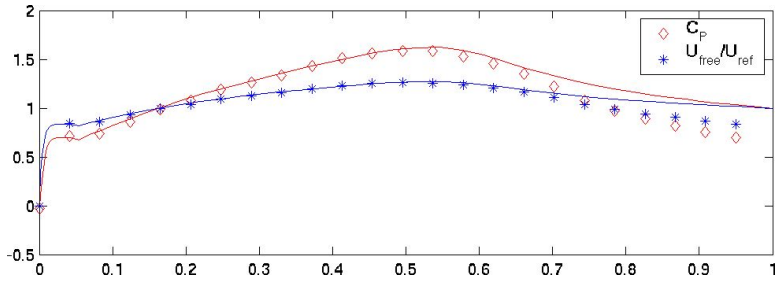

(c) $Re = 300,000$.

Figure 4.6: Pressure coefficient on suction surface for 3 Reynolds numbers for FSTI case A. The inviscid design curve for the blade is denoted by the solid lines for comparison.

Chapter 5

PIV Measurements

5.1 Results

5.1.1 Preliminary Measurements

For diagnostic purposes, initial PIV runs were conducted in the wind tunnel for a Re of $3.0 \cdot 10^4$ and an exit angle of 95°. These Re values are chosen for direct comparison with the flow-visualization results. The turbulence grid is placed 190 mm and 380 mm upstream of the test blade, corresponding to the earlier smoke-wire runs. For the clean tunnel and the two higher FSTI runs at least 20 images are saved for processing. Two runs from different camera configurations are used to acquire flow field images near the expected locations of separation and transition as shown in Figure 5.1, based upon the smoke-wire images. From these images velocity profiles along the surface of the blade are obtained along with contour plots of the forward flow probability as shown in Figures 5.2 to 5.3, in order to test the PIV configuration.

5.1.2 Comprehensive Measurements

Since PIV only requires two consecutive seeded images with a small time interval, the PIV experiments in the low speed wind tunnel allows for a study of a broadened range of Re. Five Re values are studied from $3.0 \cdot 10^4$ to $30.0 \cdot 10^4$ in order to compare the data with the smoke-wire flow visualization and previous wind tunnel studies of Murawski and others [10, 11, 17]. Due to storage and computing constraints, the tunnel exit angle is held constant at 95°, parallel to the cascade exit angle. Along with the clean tunnel configuration, the turbulence grid is again placed 190 mm and 380 mm upstream of the test blade for the two increased FSTI cases as in the smoke-wire runs. The pulse rate and triggered pulse delay are 100 μs and 255 μs, respectively, for the cases of

Re below $10.0 \cdot 10^4$ and 10 μs and 210 μs, respectively, for cases of Re equal or above $10.0 \cdot 10^4$. For each of the three camera views two runs are recorded for each flow condition with the XCAP frame grabber, resulting in a total of 5040 binary image pairs (roughly 20 GB total). A mask is then generated in XCAP for each camera view and then edited in MATLAB and stored as an 8-bit binary image. Input files are generated for each flow condition and camera view with a window size of 32 and a step size of 12. The processing of the images with the WaLPT algorithm and IPX on with a 1 GHz, Pentium III PC takes about 1 day for each camera view.

The 5040 resulting tensor files are processed with several MATLAB routines in order to obtain velocity vector fields, vorticity contours and reversed flow probability contours based upon the averaged tensors for each run. The velocity vector plots are simply a MATLAB quiver plot of the averaged resultant vectors from the u and v components of velocity calculated from WaLPT. The vorticity plots show the averaged vorticity contours as calculated with the WaLPT algorithm. The reversed flow probability is determined by averaging the sign of the u component of velocity for a given run (§3.4).

The location of the separation point and the relative size of the separation region are also determined, based upon a single tensor output file from each pair of images. The separation point is determined by finding the left-most negative u-velocity component for each image pair from the first camera view. When separation is clearly observed, the point of separation is always in the first view. The point of separation is then averaged and output with the standard deviation for each run. The relative size of the separation region is determined by finding the number of negative u-velocity components in the field, then dividing by the field size. Based upon a pixels:length ratio of 216.2 and a camera resolution of 1018×1008 pixels, the total image size is roughly a 5×5 cm square. The area of the separation region in each image pair is approximated by finding that portion of the image area which is reversed flow. The first and third camera view completely contain the separation regions observed in this study, so the separation area is drawn from these views. Note that there is some overlap between each camera view, so the total separation area is not simply a summation of those determined from the first and third views. As with the point of separation, the average area and the standard deviation are output for each run.

The tangential velocity, vorticity, and RMS velocity profiles are determined in another set of MATLAB routines based upon the averaged output files. The total velocity is first interpolated to expand it to an array equal in size to the image files. Points equally spaced along the suction surface are selected as local origins, and the global coordinates of the points falling on normal rays projected from the blade surface at these local origins are determined. The global components of

the interpolated values of velocity, vorticity, and RMS velocity are then mapped into components normal and tangential to the blade surface. The tangential components are non-dimensionalized by the exit velocity and plotted. The number and spacing of these local normals may be varied such that variations in the profiles are clearly illustrated along the blade from 45% SSL to just downstream of the trailing edge. Ten profiles are generated from normals offset from the extents of each camera view to minimize overlap between the three views shown.

Transition is more difficult to determine based upon the PIV output files. To approximate the point of transition for a given run, a movie is compiled from the 112 image pairs for each condition and the location of the observed shedding vortices is observed. The transition point can therefore be determined visually from the raw PIV images for a greater range in Re than the smoke-wire runs. In general, RMS velocity does not appear to be a direct indicator of transition at low temporal resolution, but in several cases for the clean tunnel a marked increase in the size of the vorticity layer corresponds to a sudden change in the RMS velocity. Further investigation is necessary to confirm whether or not these changes in vorticity and RMS velocity suggest that transition has occurred just upstream.

5.2 Discussion

The initial PIV runs yield promising results. The uniform particle distribution near the wall, recorded with a high resolution camera focused on the separation and transition regions result in some of the first such detailed images of the flow in the separation region over low pressure turbine blades. The raw PIV images are shown in Figure 5.1 while velocity profiles corresponding to each image are shown in Figure 5.2. The velocity profiles obtained show the component of velocity parallel to the blade surface. The profiles are superimposed to show the decrease in velocity near the wall and the emergence of reversed flow downstream along the suction surface. The size of the separation region observed in this camera view is about 1.1% SSL. The second view, further downstream, shows that the region of reversed flow extends downstream and that the size remains near 1% SSL. The contour plots of forward flow probability indicate very clearly the region of separation and the reversed flow direction within as shown in Figure 5.3. From the second camera view, the average flow velocity is observed to be less reversed as we move along the surface. The most negative velocity profiles are therefore closer to the trailing edge, as the size of the separation region increases downstream. The intermittency of the positive and negative values of velocity nearest the trailing edge suggest an unsteady transition region where the flow may reattach and detach with time. For these preliminary runs, the locations of separation and transition compare

well to the smoke- wire images, though the height of the separation region does not. The results of the more comprehensive PIV experiments below yield a more detailed quantitative analysis of separated flows over low pressure turbine blades.

The velocity vector, vorticity, and reversed flow probability field plots are shown for each camera view in Figures 5.4 through 5.18. These plots clearly illustrate the location and size of the separation region. The contour plots are especially illuminating as evidence of how the separation region is changing in time. (Refer to Figure 3.5 for the relative location of the views.)

Another method of tracking the size and location of the separation region is to study the tangential velocity and vorticity profiles along the blade surface. The averaged tangential velocity, vorticity, and RMS velocity profiles are shown in Figures 5.19 through 5.33 for each camera view. For the cases with the earliest and largest separation, the inflection points in the tangential velocity profiles clearly trace the boundary of the separation region. Note that the referenced inflection points are those observed in the profile plots, and not measured points where the velocity gradient is zero ($\frac{\partial^2 u}{\partial y^2} = 0$). For higher Re and FSTI cases, the inflection point comes back toward the blade surface indicating that the flow is approaching reattachment for those conditions. For the higher Re and FSTI cases a typical turbulent boundary layer results and the velocity profiles show no signs of separation along the blade wall. The vorticity profiles show a marked increase in vorticity near the blade wall, with a maximum value at the interface of the freestream and reversed flow regions. The vorticity profiles indicate that the higher Re and FSTI cases result in a shear layer tightly constrained to the near-wall region. The RMS velocity profiles simply indicate how much the total velocity is changing on a normal extended from the blade wall. Separation is indicated by large variations *far* from the blade wall.

The location of the onset of transition is difficult to determine based upon the raw images, but an image pair for each Re with FSTI=1% is included in Figures 5.34 to 5.38 as an illustration of the types of turbulent structures visible. The movies from which these image pairs are taken are included in the electronic submission of the current study. No attempt has yet been made to tabulate the location of the onset of transition or reattachment length based on these images.

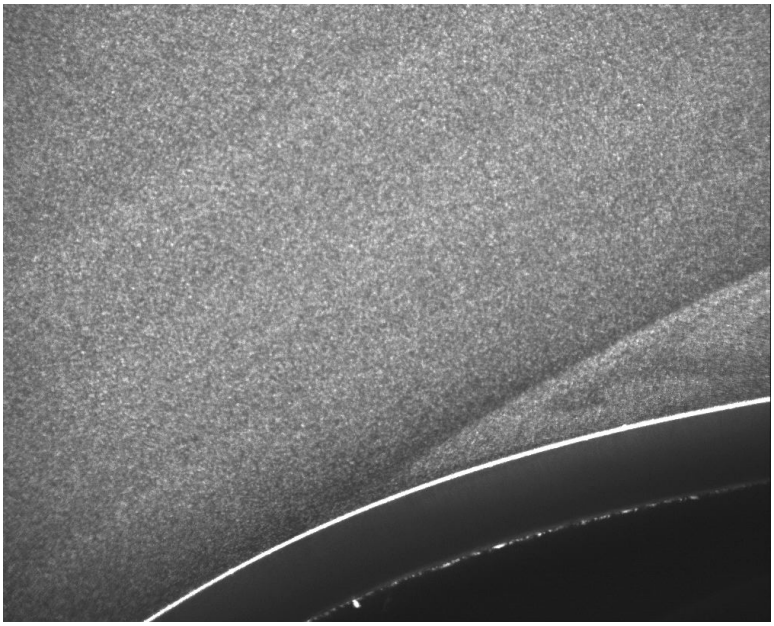

(a) **At separation point.**

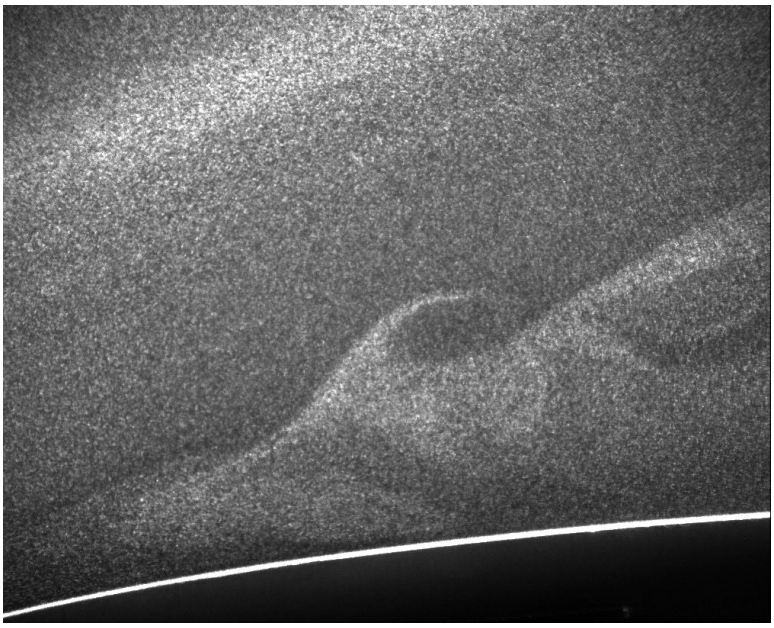

(b) **Downstream of separation, near transition.**

Figure 5.1: Separation region visualized by 1 micron oil droplets and laser sheet for use in PIV.

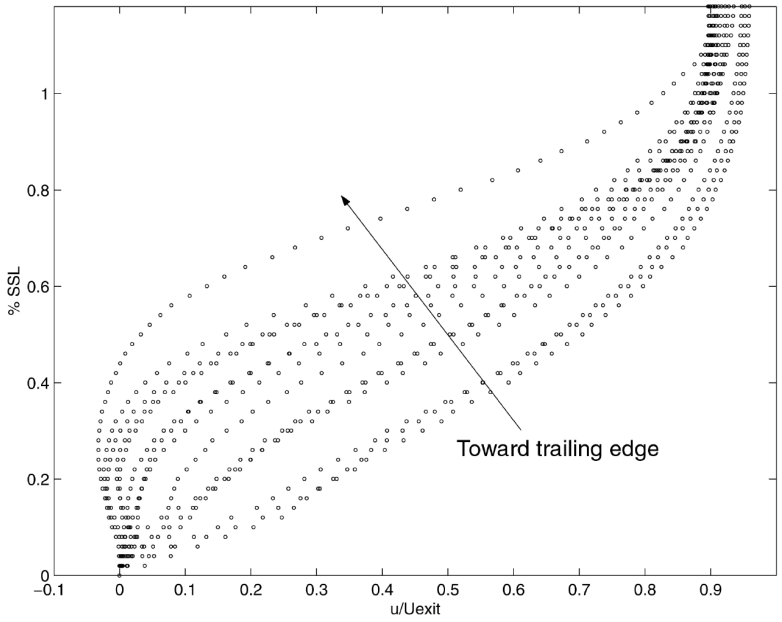

(a) **At separation point.**

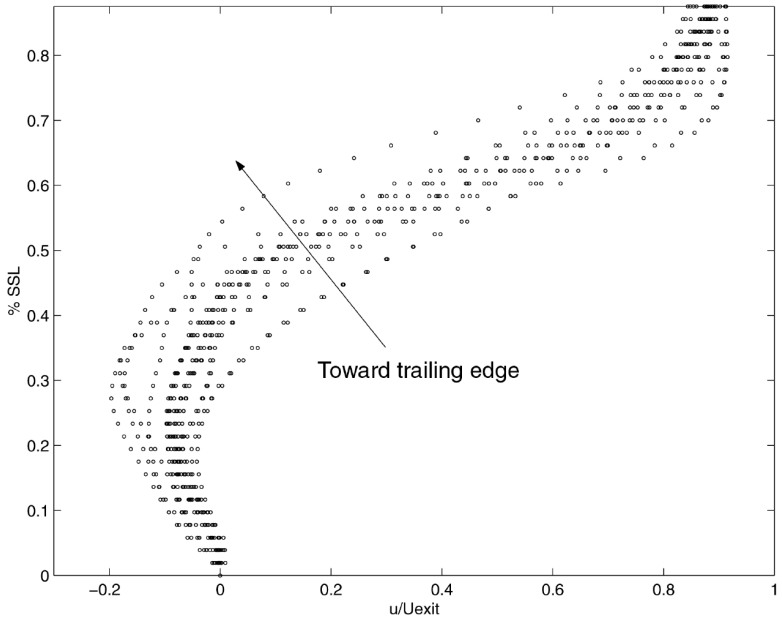

(b) **Downstream of separation, near transition.**

Figure 5.2: Velocity profiles determined from PIV.

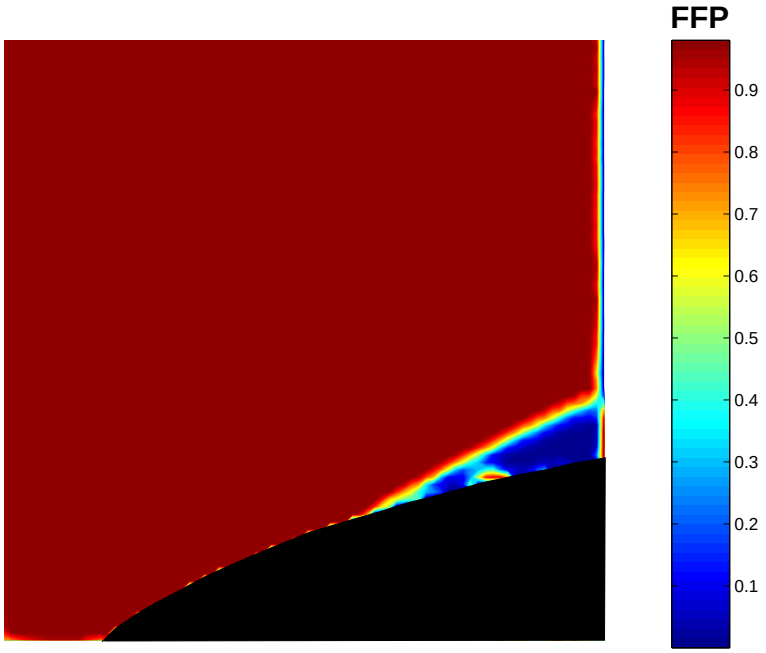

(a) **At separation point.**

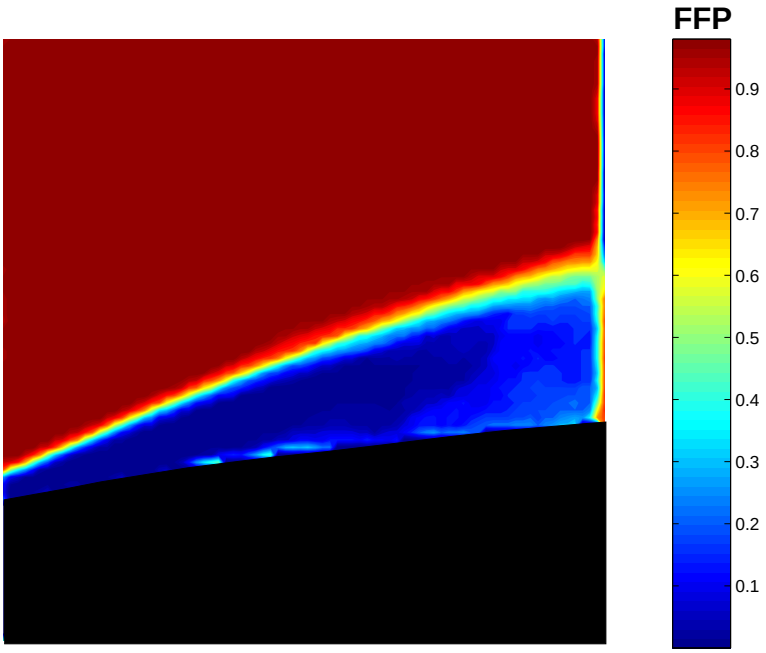

(b) **Downstream of separation, near transition.**

Figure 5.3: Forward flow probability of the separation region as determined by PIV.

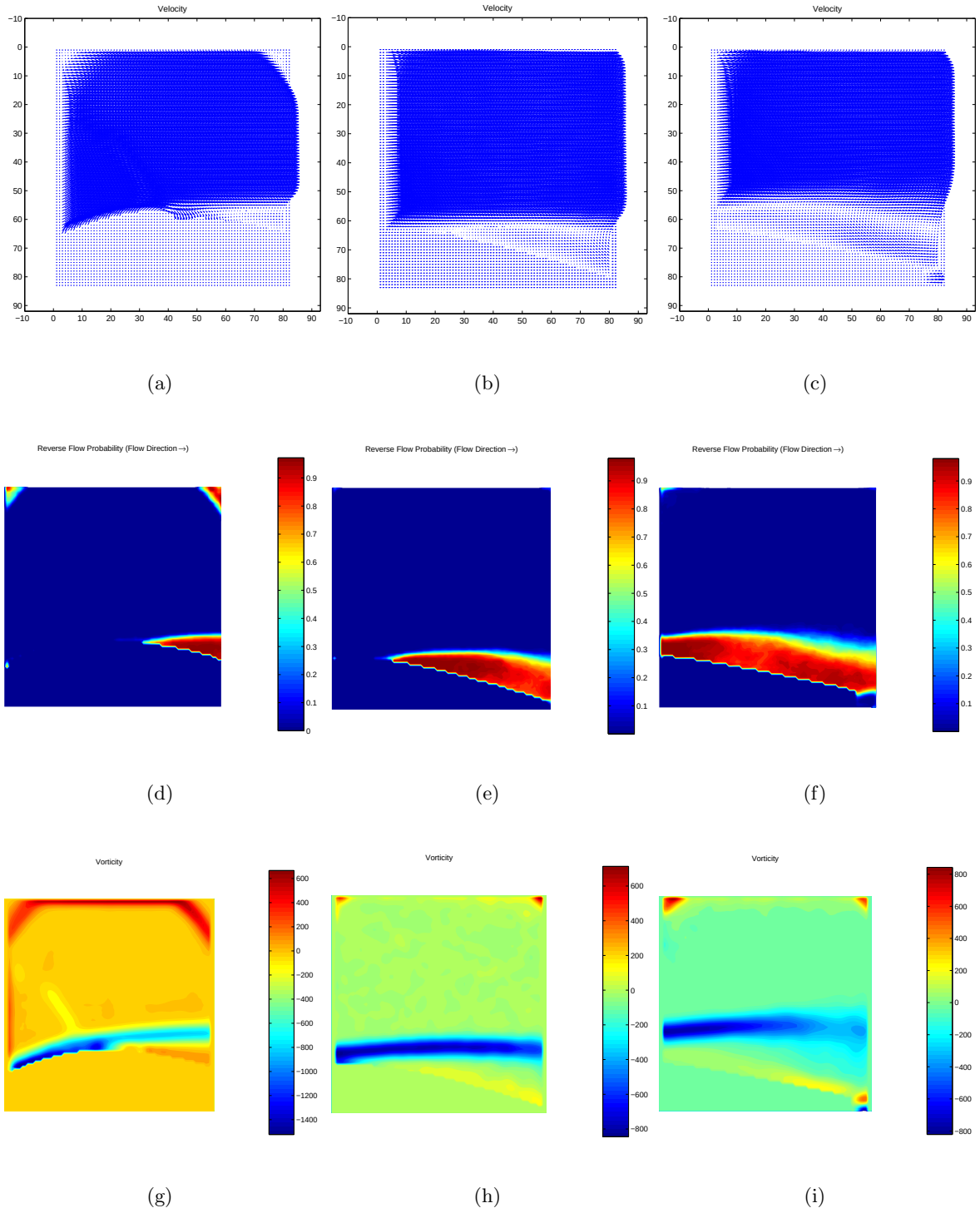

Figure 5.4: Velocity, RFP, and Vorticity fields for each view at $Re = 3.0 \cdot 10^4$, FSTI case A

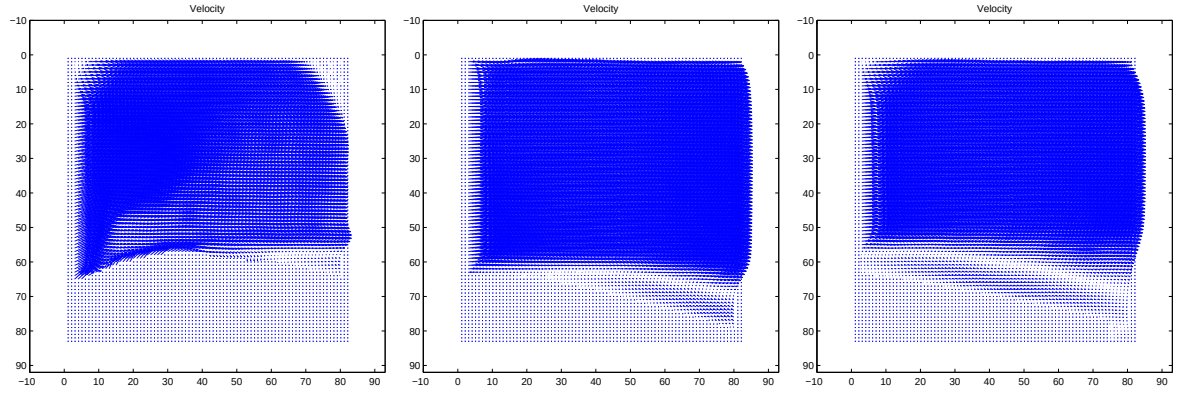

(a) (b) (c)

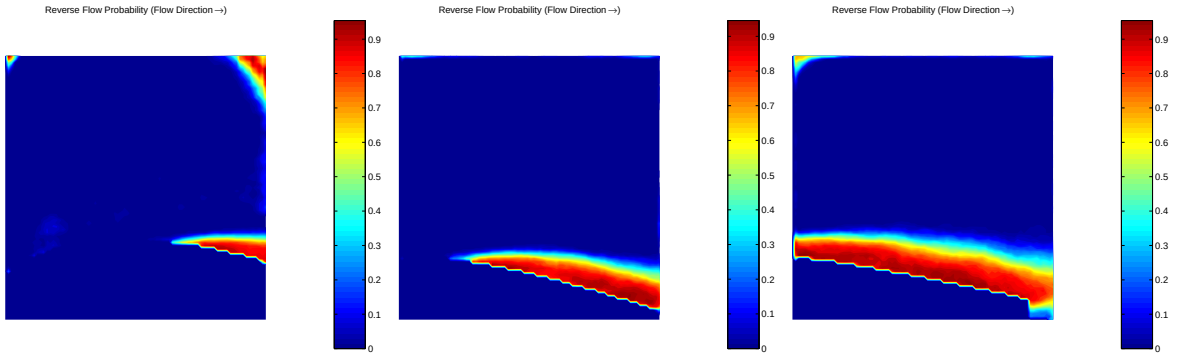

(d) (e) (f)

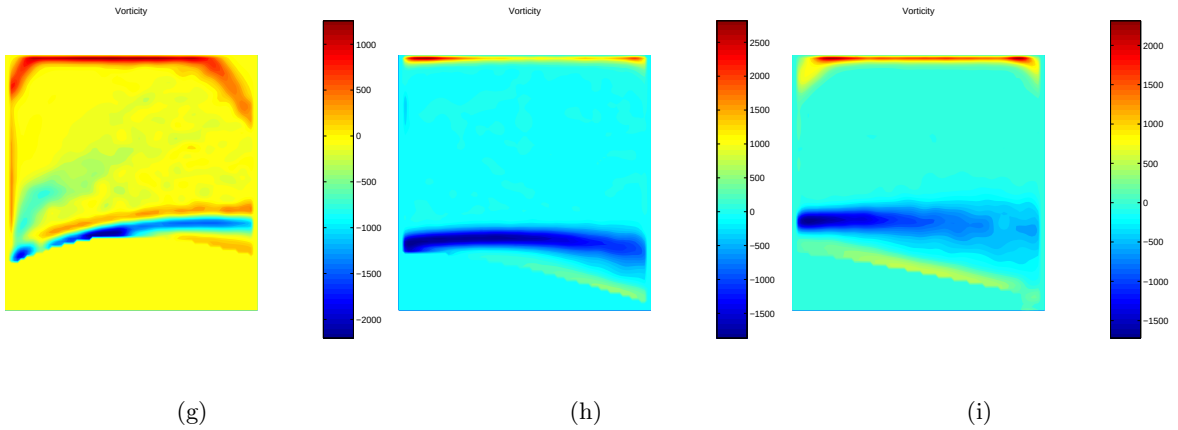

(g) (h) (i)

Figure 5.5: Velocity, RFP, and Vorticity fields for each view at $Re = 5.0 \cdot 10^4$, FSTI case A

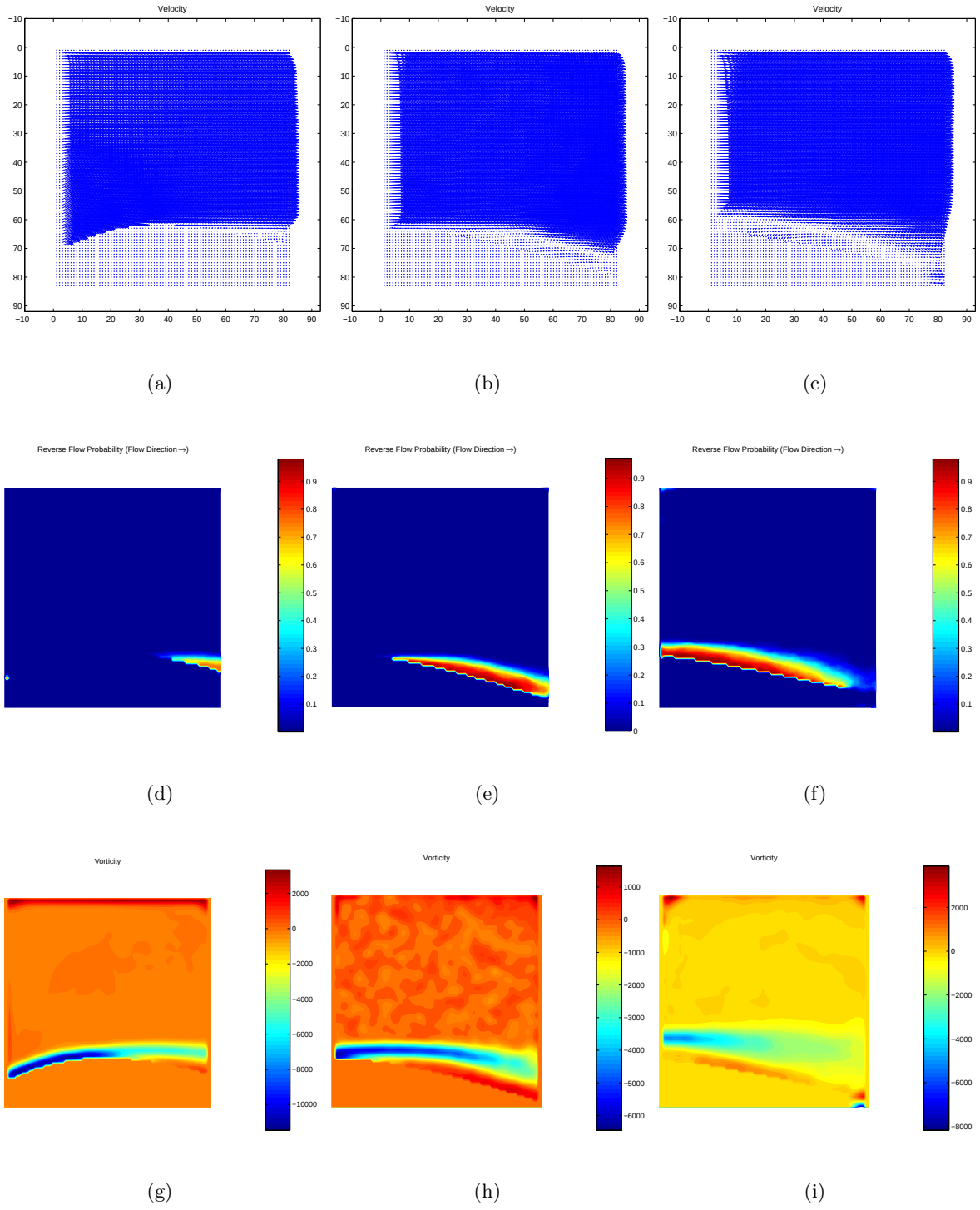

Figure 5.6: Velocity, RFP, and Vorticity fields for each view at $Re = 10.0 \cdot 10^4$, FSTI case A

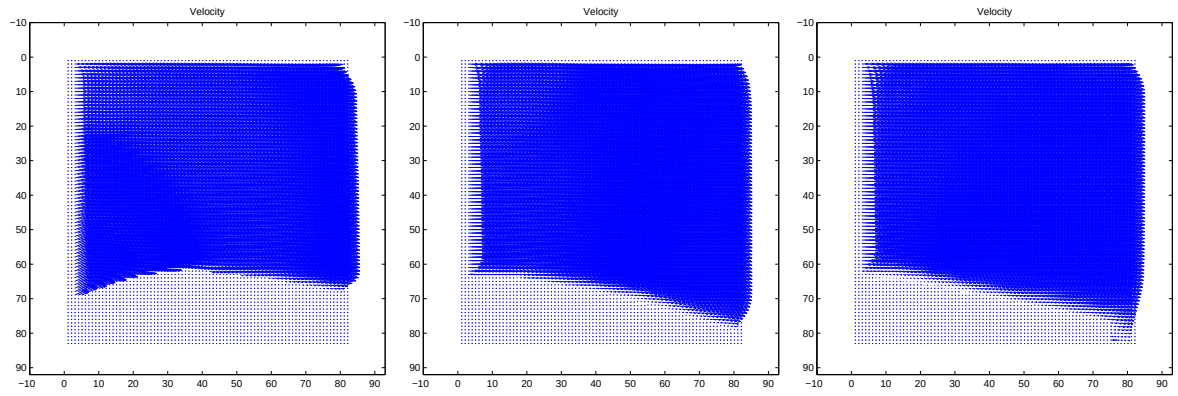

(a) (b) (c)

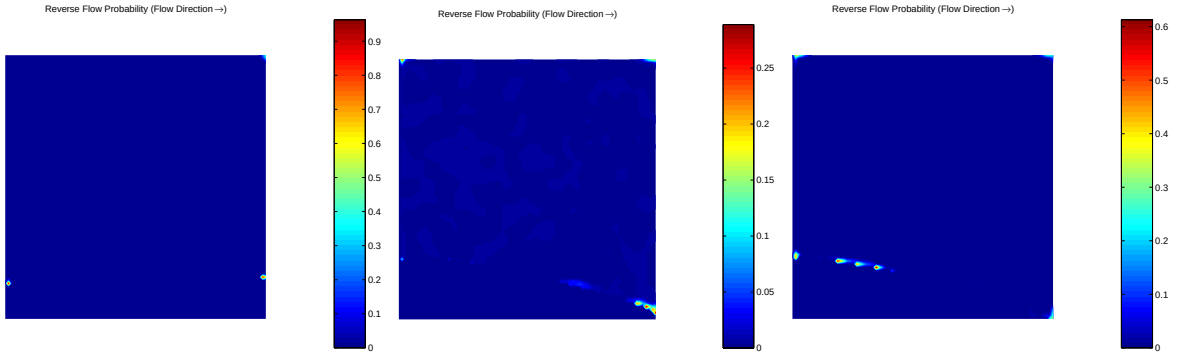

(d) (e) (f)

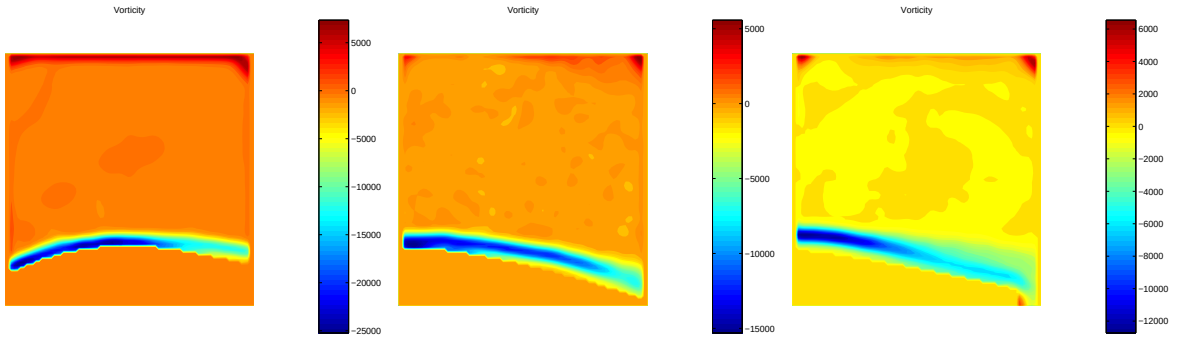

(g) (h) (i)

Figure 5.7: Velocity, RFP, and Vorticity fields for each view at $Re = 20.0 \cdot 10^4$, FSTI case A

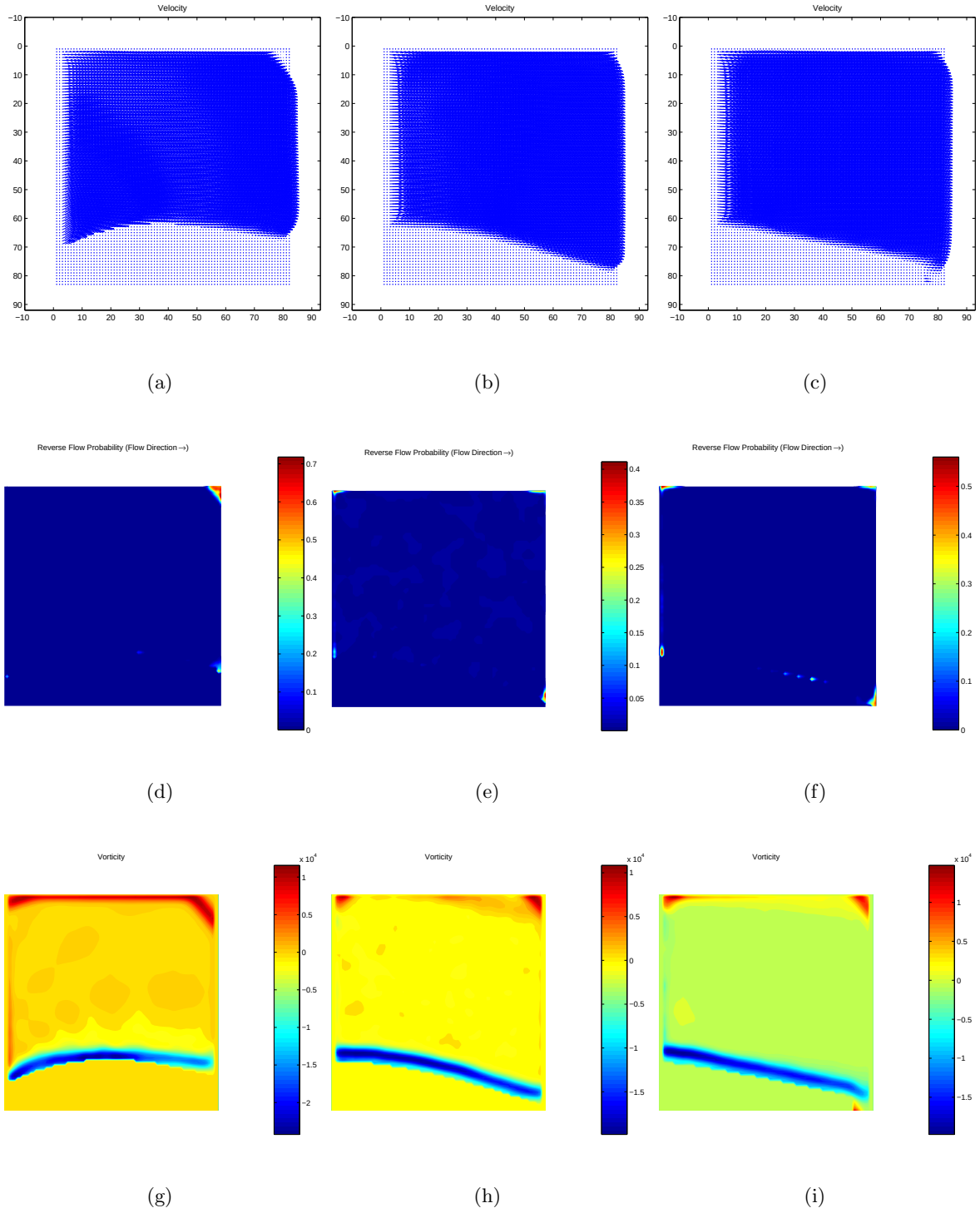

Figure 5.8: Velocity, RFP, and Vorticity fields for each view at $Re = 30.0 \cdot 10^4$, FSTI case A

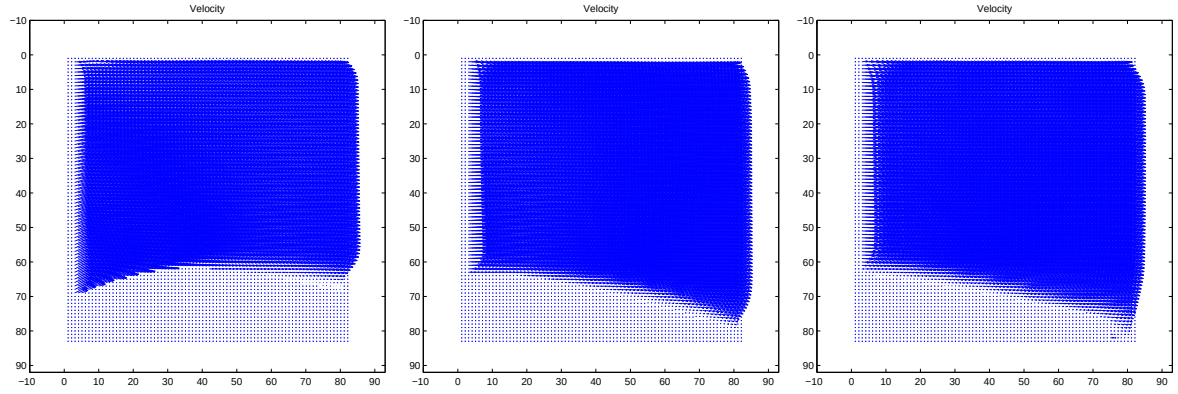

(a) (b) (c)

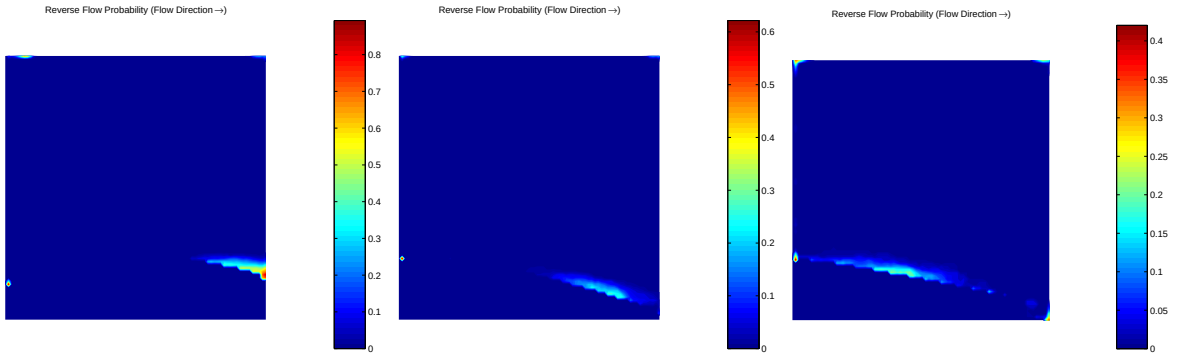

(d) (e) (f)

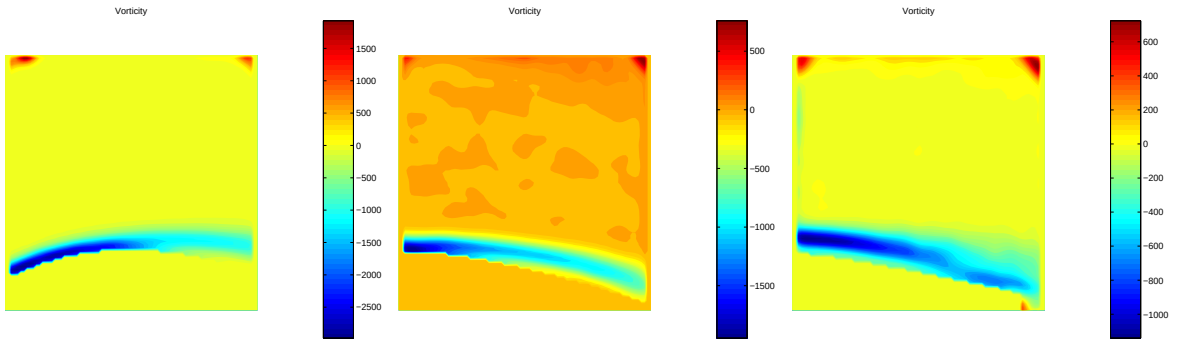

(g) (h) (i)

Figure 5.9: Velocity, RFP, and Vorticity fields for each view at $Re = 3.0 \cdot 10^4$, FSTI case B

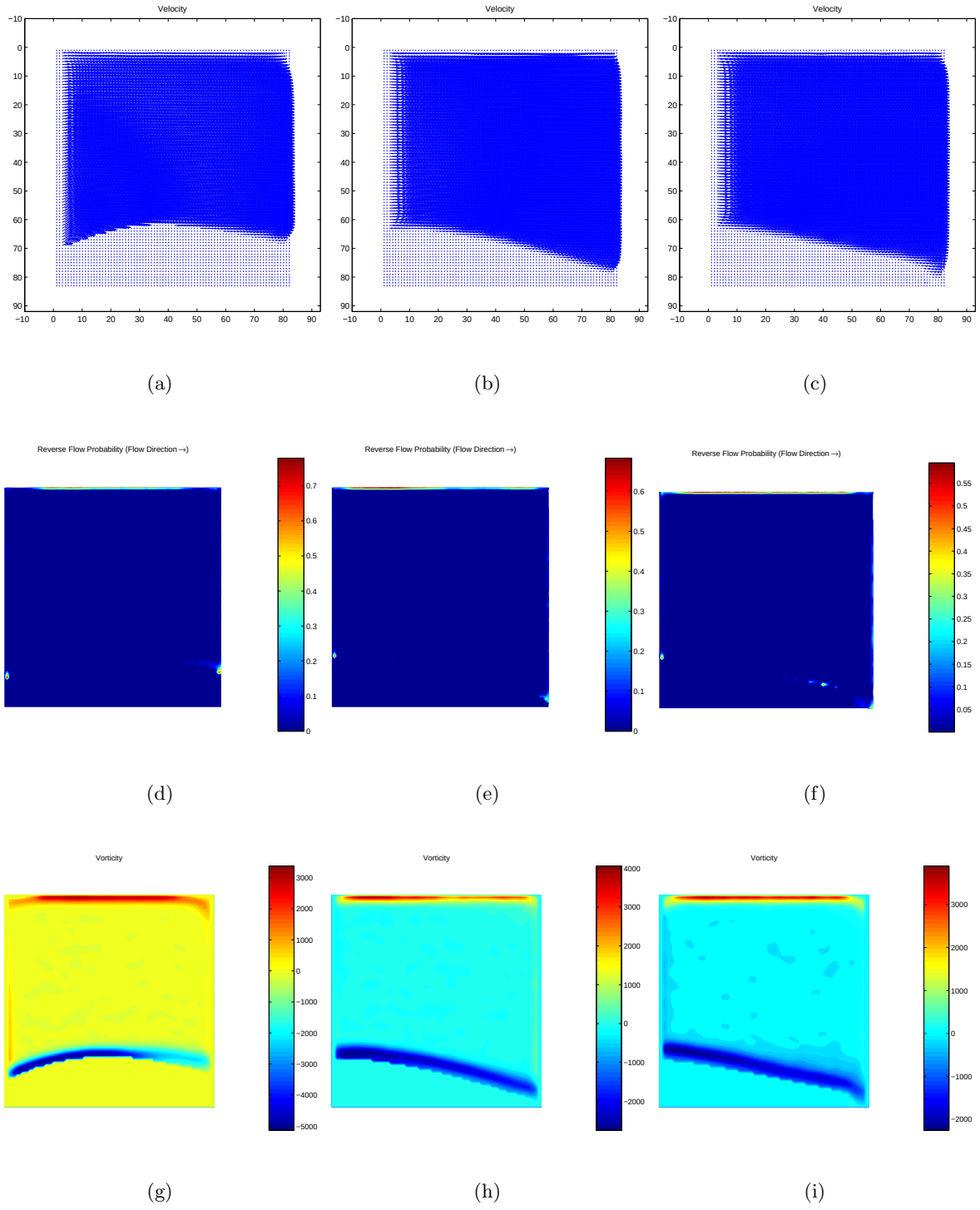

Figure 5.10: Velocity, RFP, and Vorticity fields for each view at $Re = 5.0 \cdot 10^4$, FSTI case B

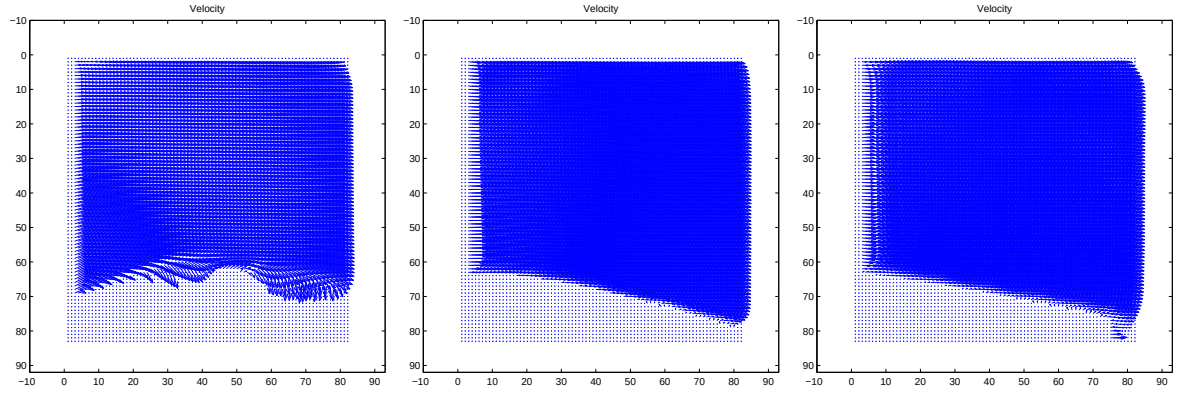

(a) (b) (c)

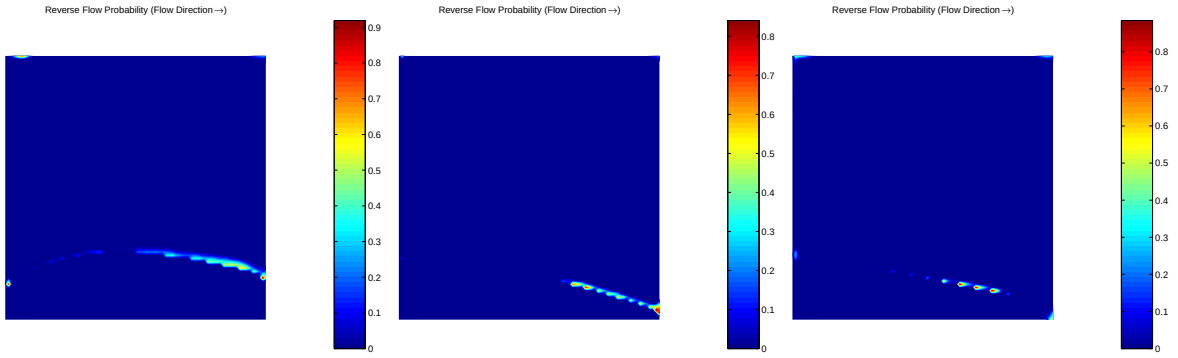

(d) (e) (f)

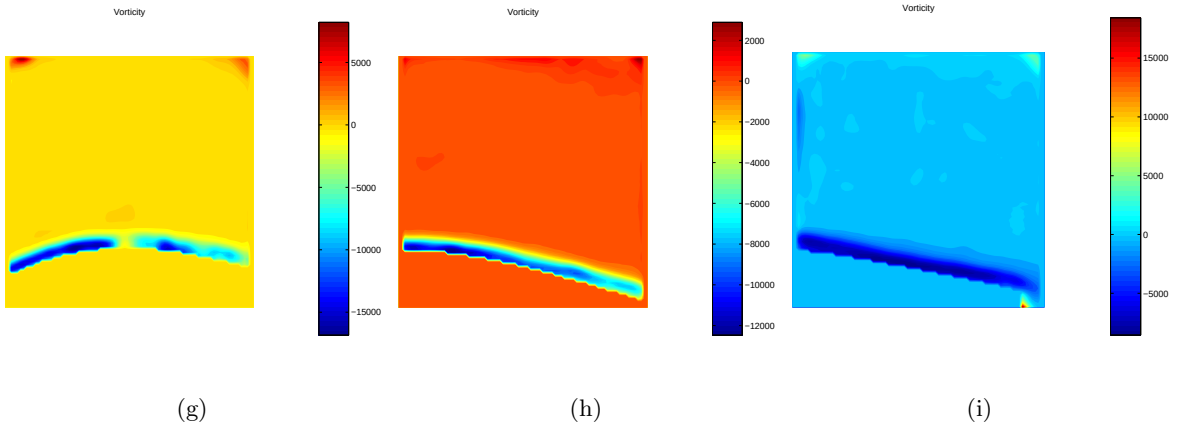

(g) (h) (i)

Figure 5.11: Velocity, RFP, and Vorticity fields for each view at $Re = 10.0 \cdot 10^4$, FSTI case B

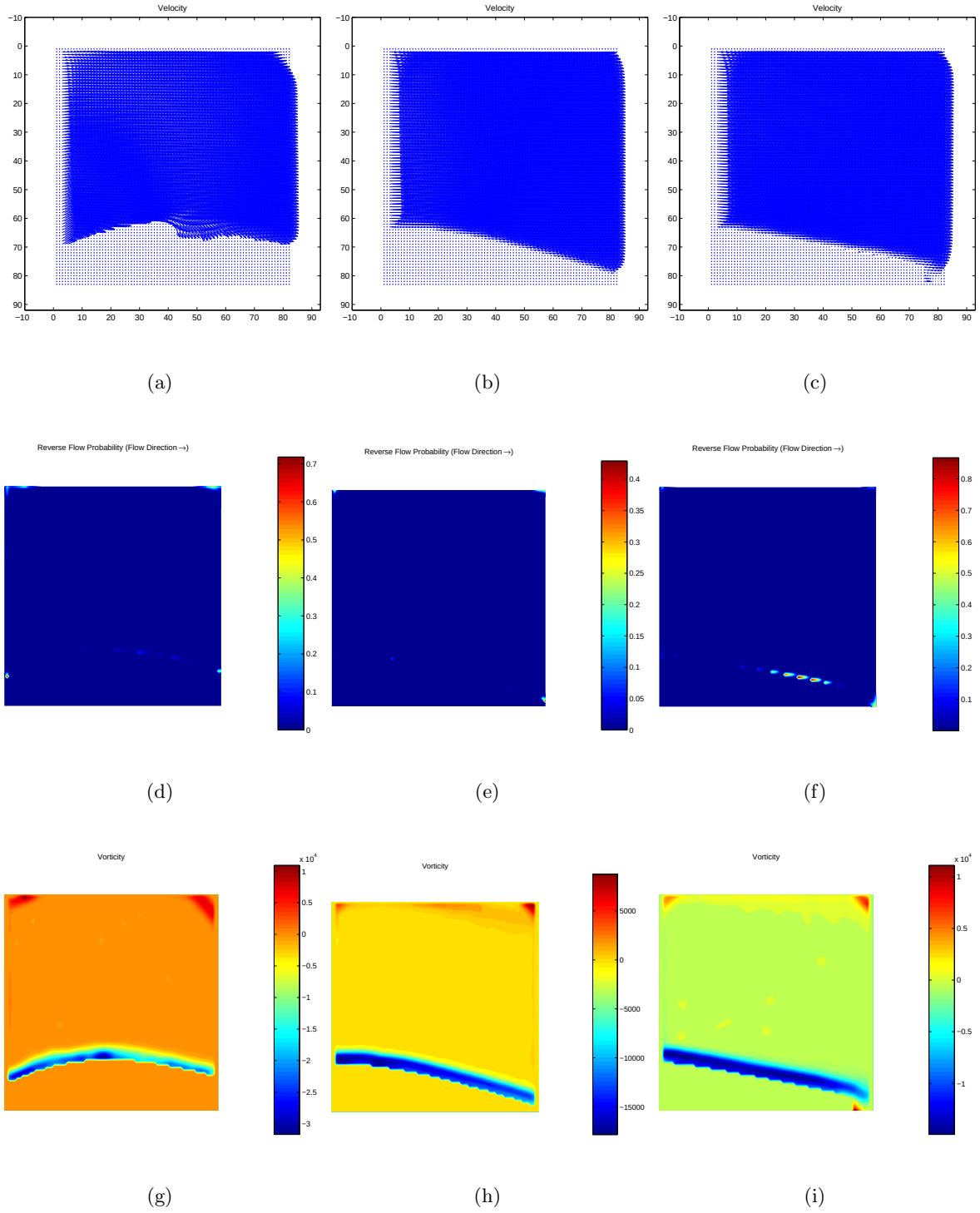

Figure 5.12: Velocity, RFP, and Vorticity fields for each view at $Re = 20.0 \cdot 10^4$, FSTI case B

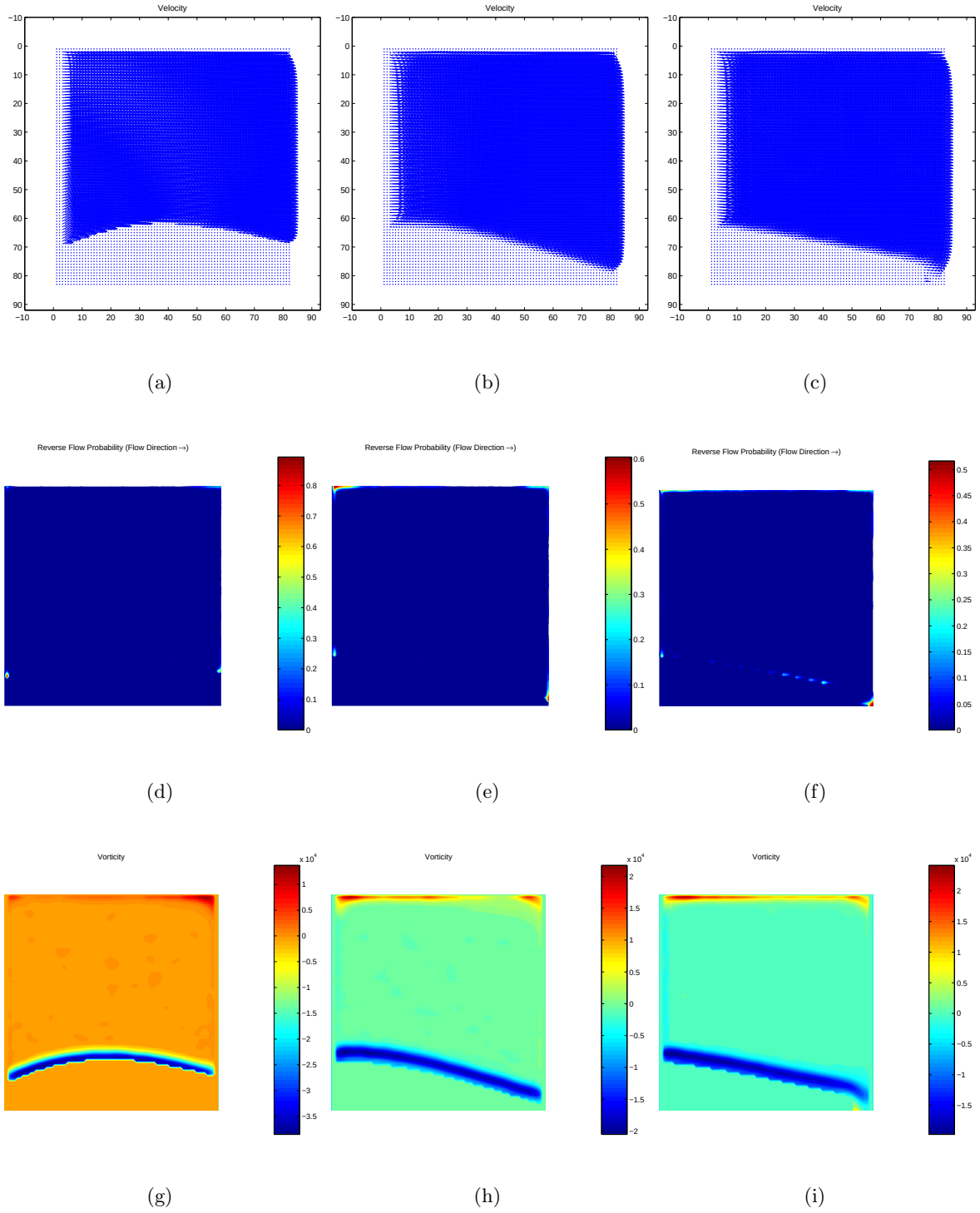

Figure 5.13: Velocity, RFP, and Vorticity fields for each view at $Re = 30.0 \cdot 10^4$, FSTI case B

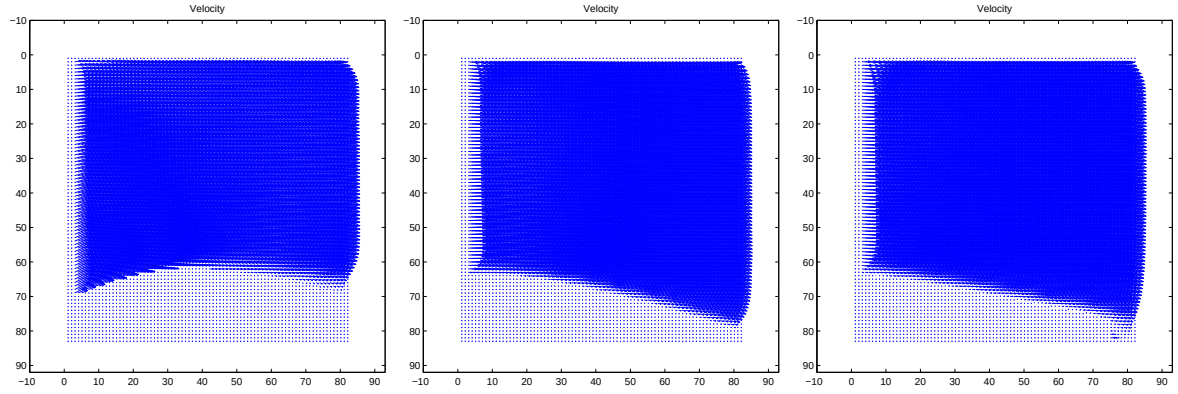

(a) (b) (c)

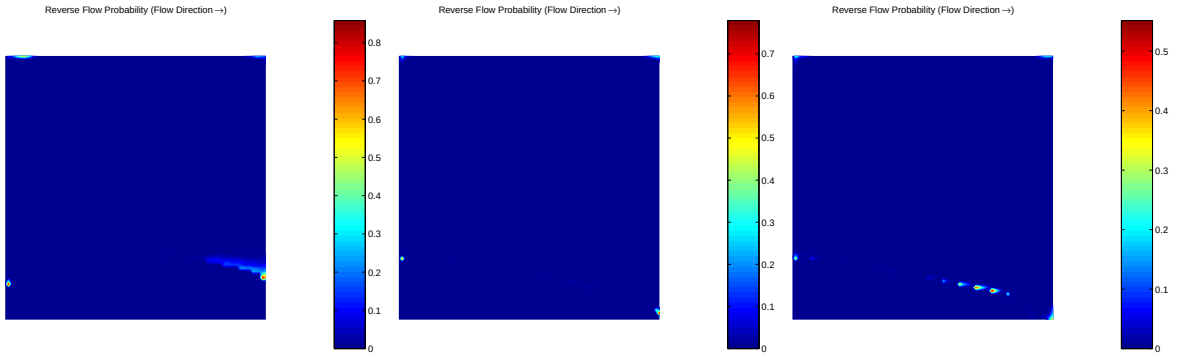

(d) (e) (f)

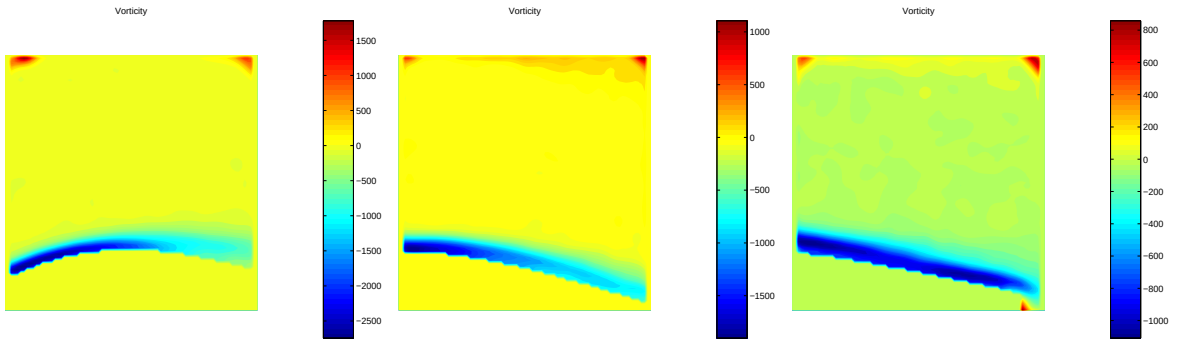

(g) (h) (i)

Figure 5.14: Velocity, RFP, and Vorticity fields for each view at $Re = 3.0 \cdot 10^4$, FSTI case C

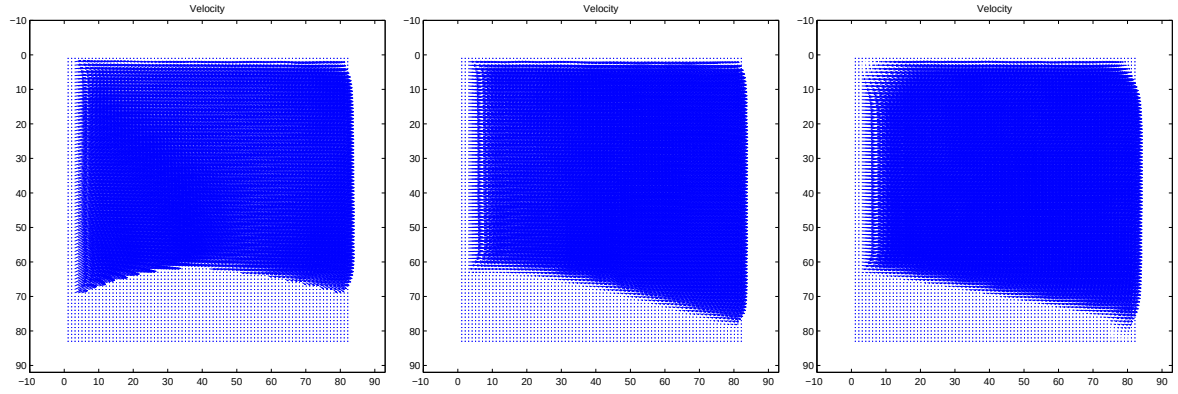

(a) (b) (c)

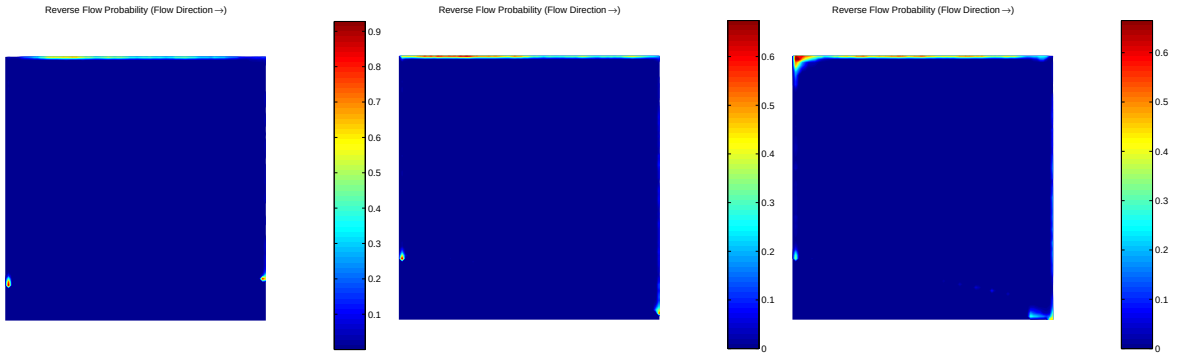

(d) (e) (f)

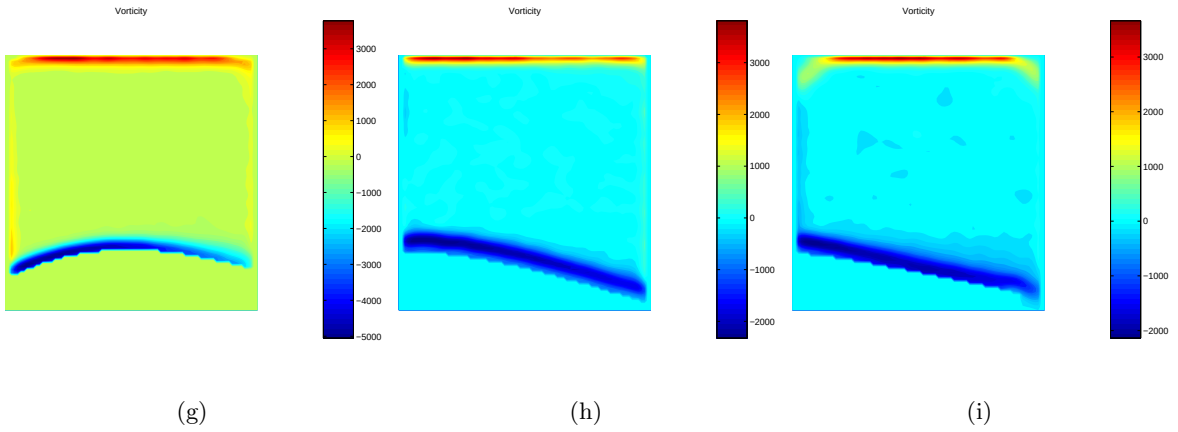

(g) (h) (i)

Figure 5.15: Velocity, RFP, and Vorticity fields for each view at $Re = 5.0 \cdot 10^4$, FSTI case C

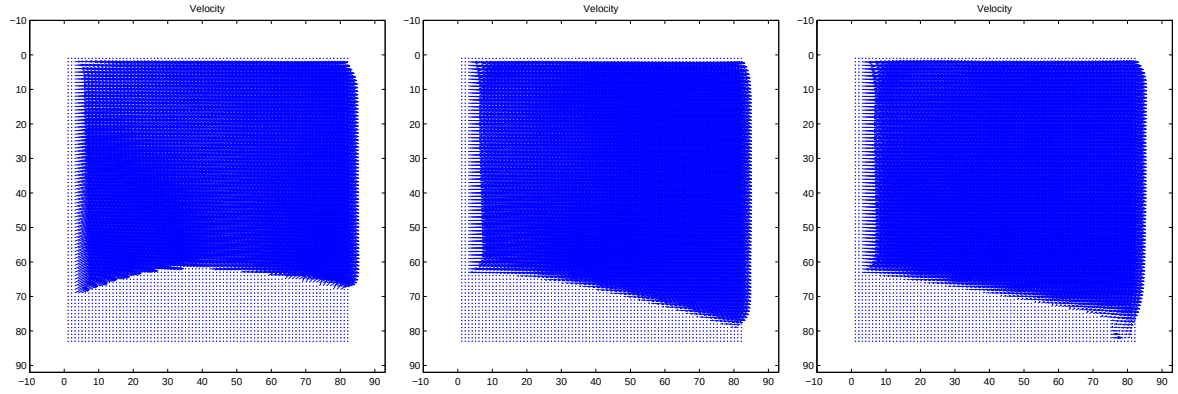

(a) (b) (c)

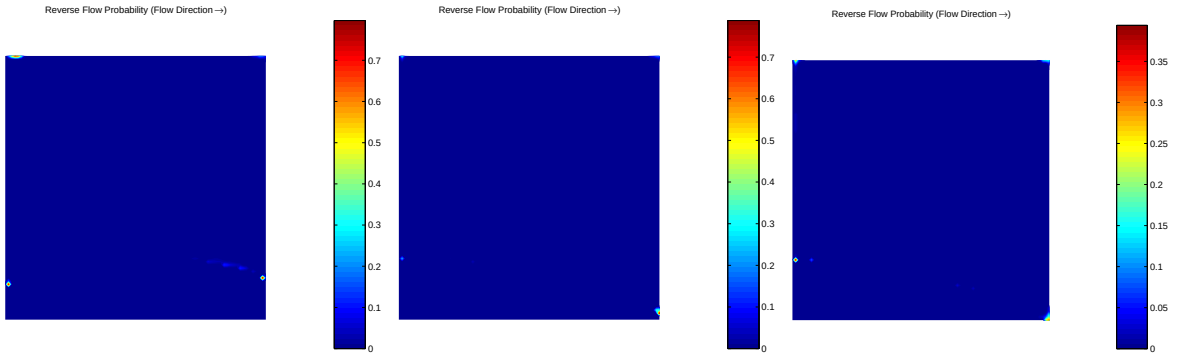

(d) (e) (f)

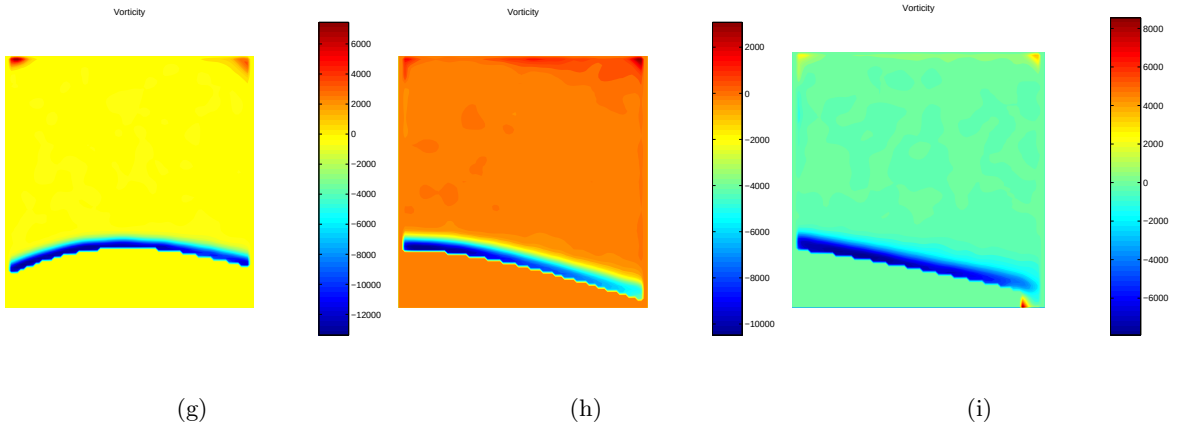

(g) (h) (i)

Figure 5.16: Velocity, RFP, and Vorticity fields for each view at $Re = 10.0 \cdot 10^4$, FSTI case C

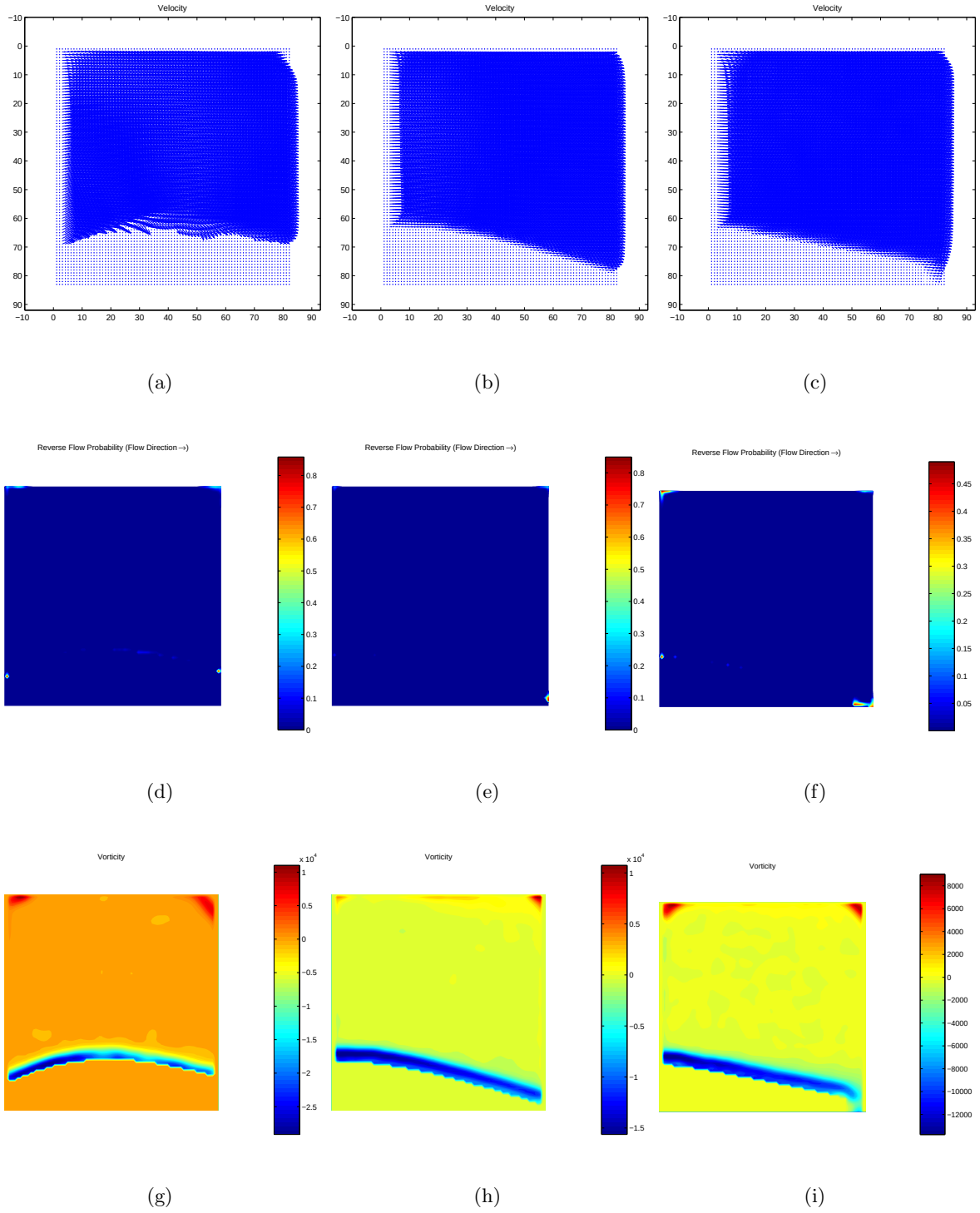

Figure 5.17: Velocity, RFP, and Vorticity fields for each view at $Re = 20.0 \cdot 10^4$, FSTI case C

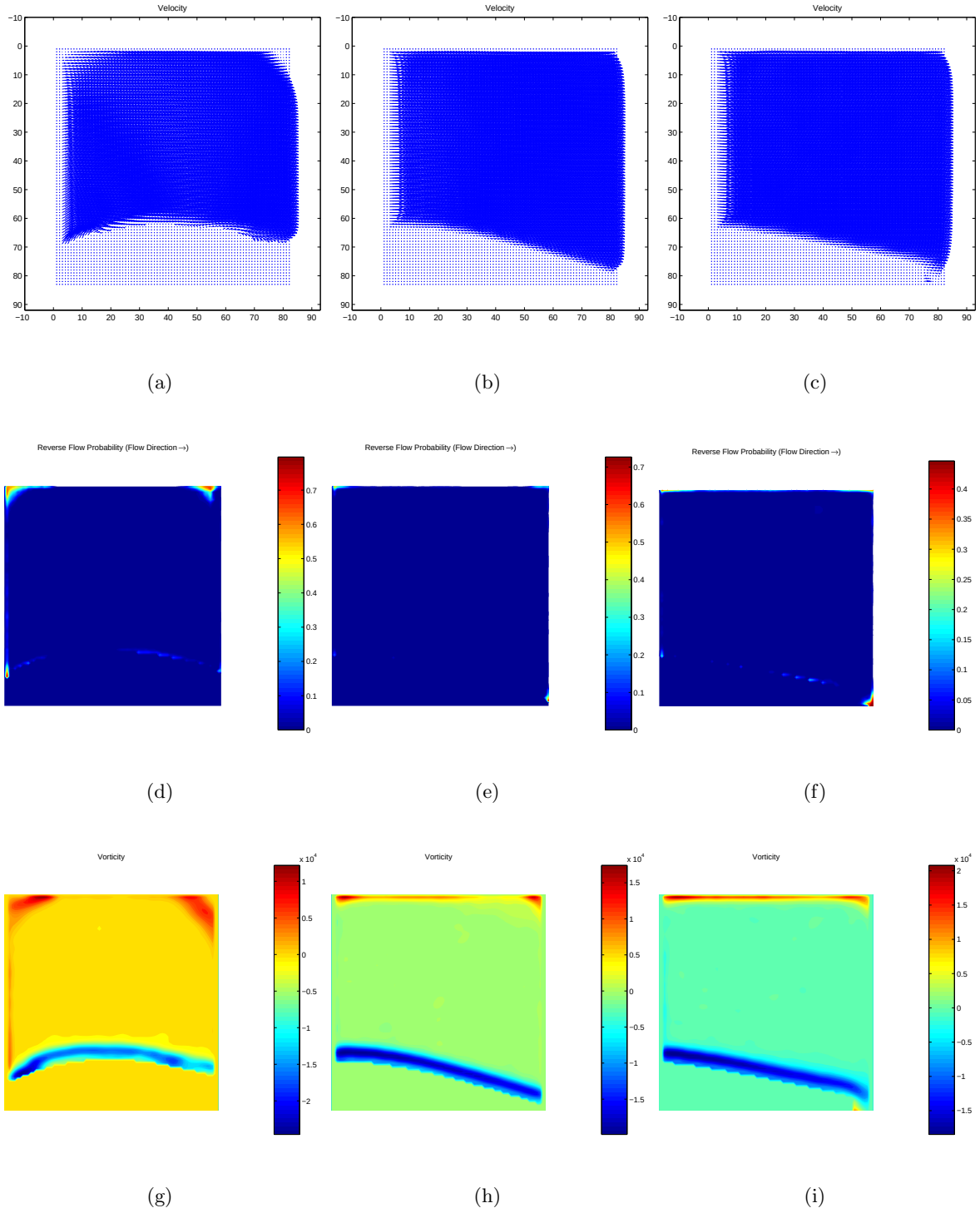

Figure 5.18: Velocity, RFP, and Vorticity fields for each view at $Re = 30.0 \cdot 10^4$, FSTI case C

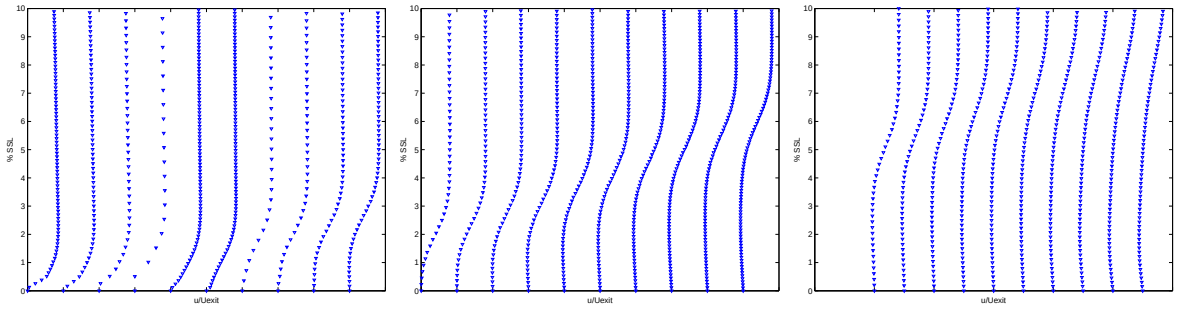

(a) (b) (c)

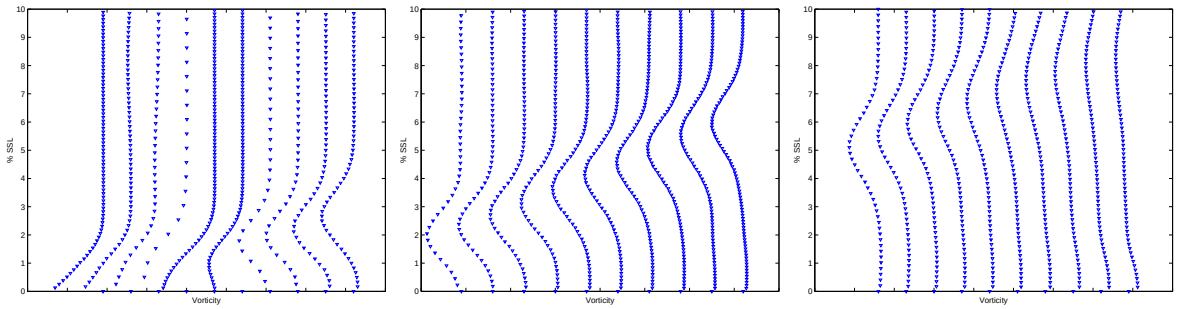

(d) (e) (f)

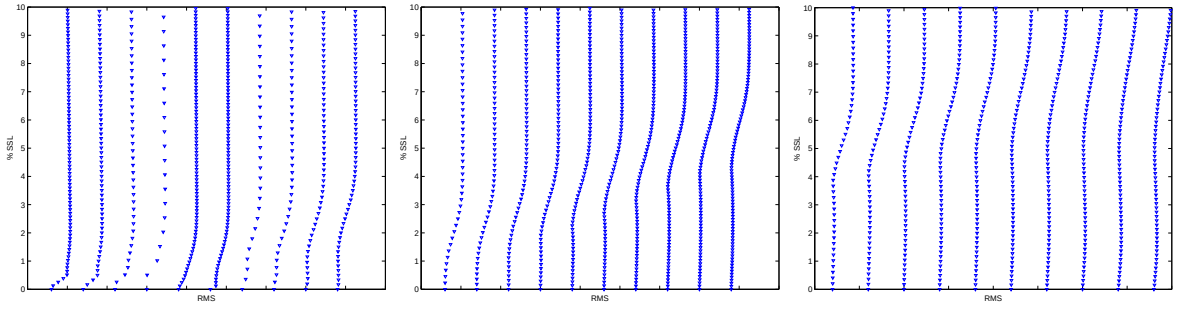

(g) (h) (i)

Figure 5.19: Velocity, Vorticity, and RMS velocity profiles for each view at $Re = 3.0 \cdot 10^4$, FSTI case A

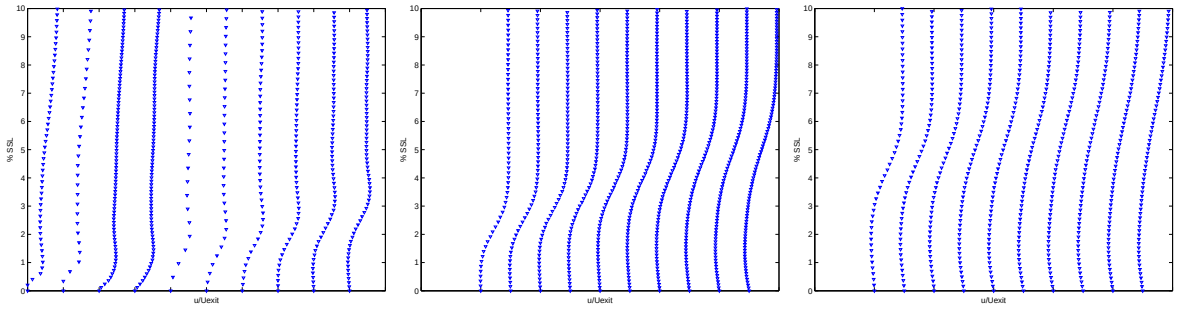

(a) (b) (c)

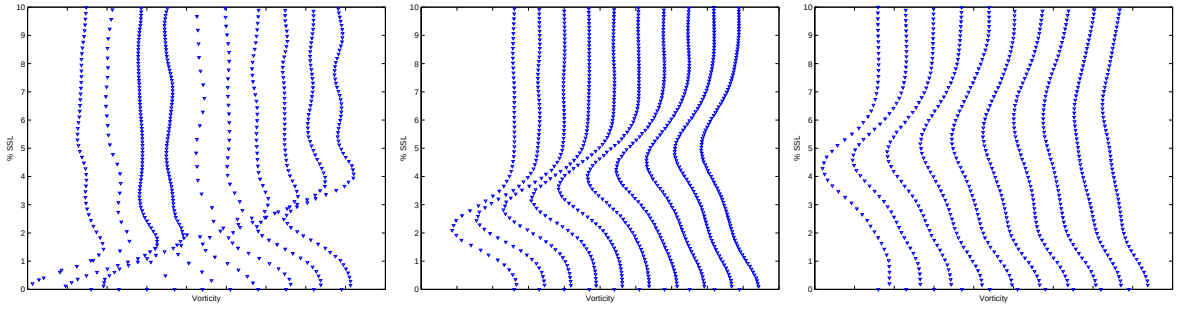

(d) (e) (f)

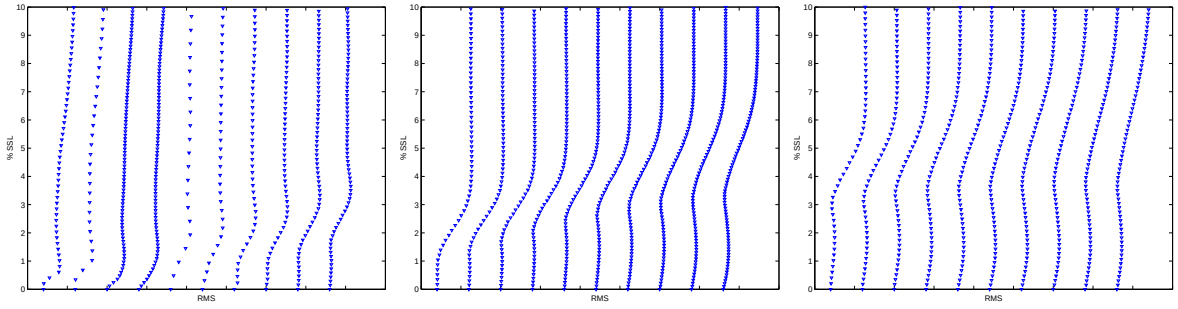

(g) (h) (i)

Figure 5.20: Velocity, Vorticity, and RMS velocity profiles for each view at $Re = 5.0 \cdot 10^4$, FSTI case A

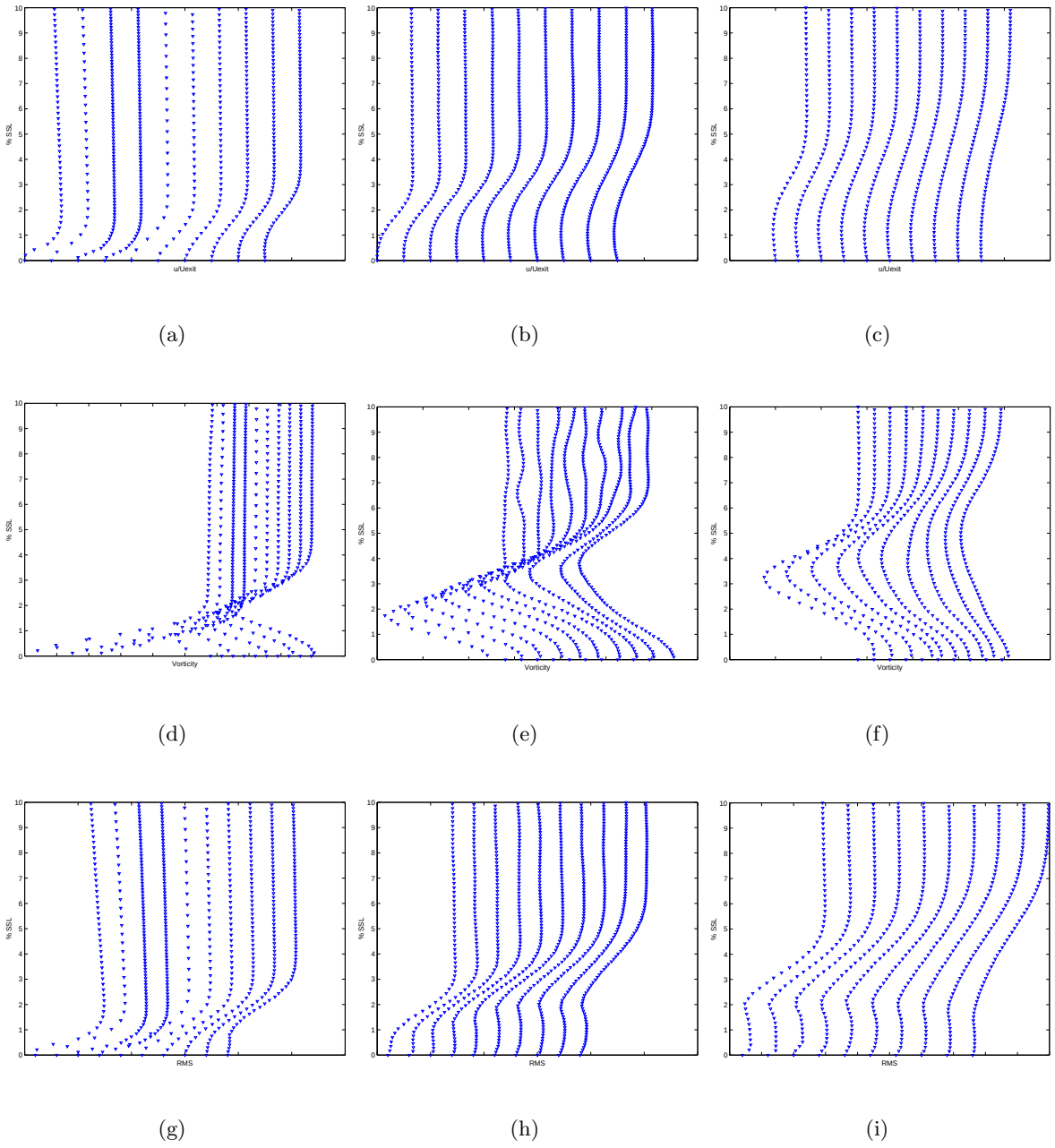

(a) (b) (c)

(d) (e) (f)

(g) (h) (i)

Figure 5.21: Velocity, Vorticity, and RMS velocity profiles for each view at $Re = 10.0 \cdot 10^4$, FSTI case A

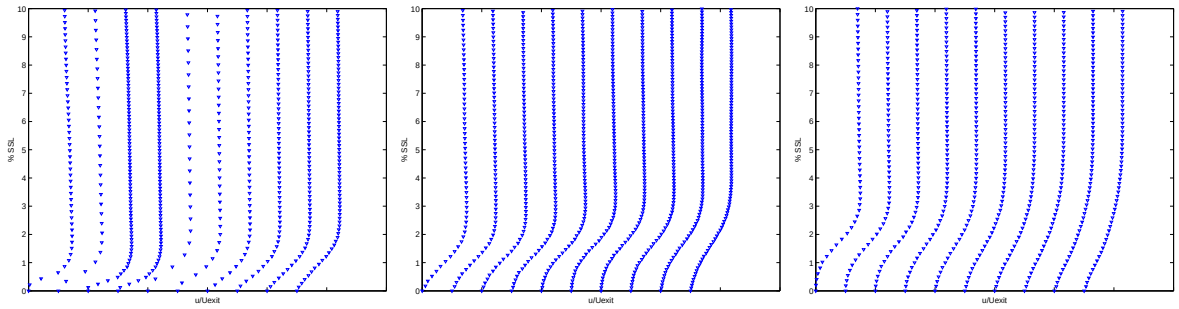

(a) (b) (c)

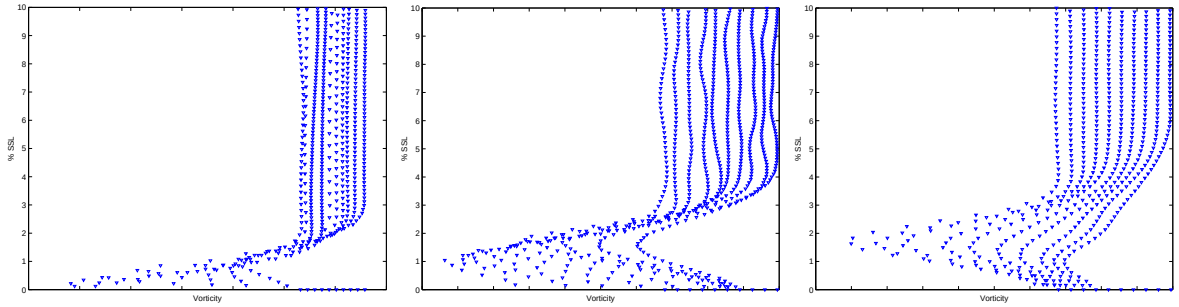

(d) (e) (f)

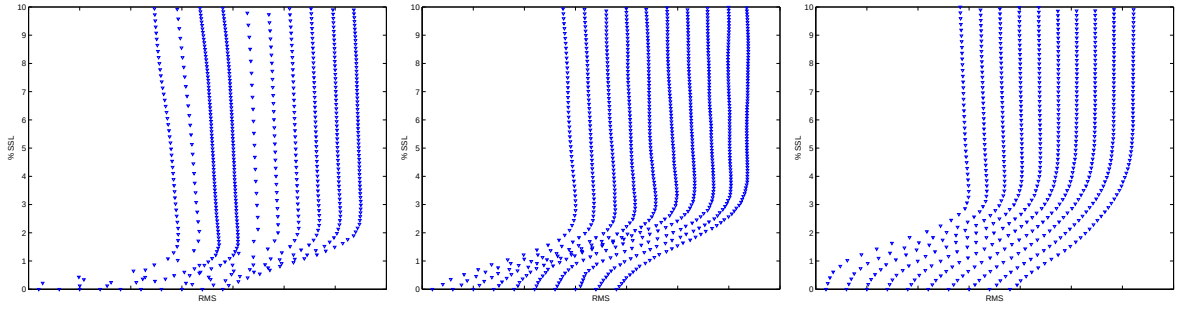

(g) (h) (i)

Figure 5.22: Velocity, Vorticity, and RMS velocity profiles for each view at $Re = 20.0 \cdot 10^4$, FSTI case A

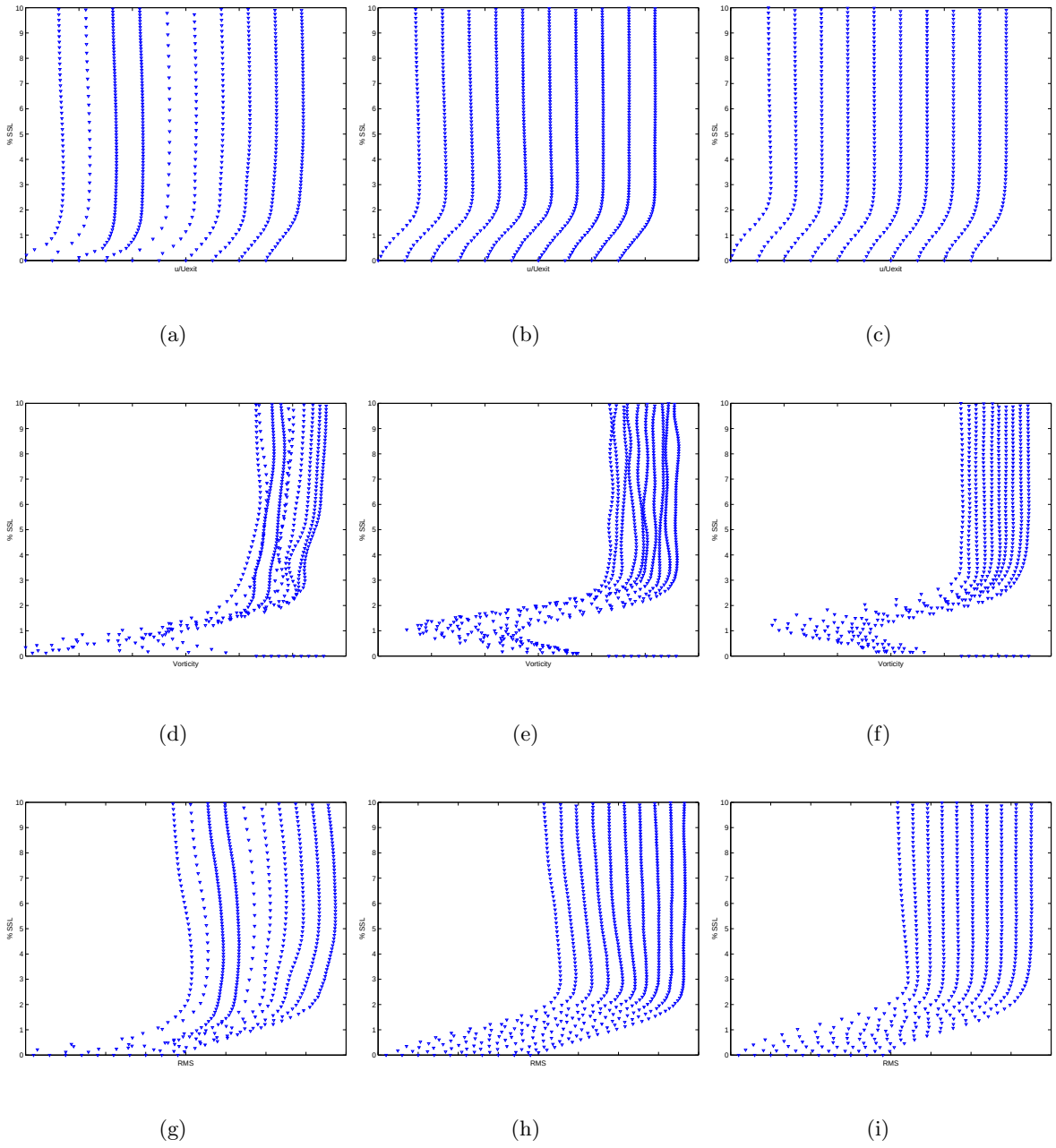

(a) (b) (c)

(d) (e) (f)

(g) (h) (i)

Figure 5.23: Velocity, Vorticity, and RMS velocity profiles for each view at $Re = 30.0 \cdot 10^4$, FSTI case A

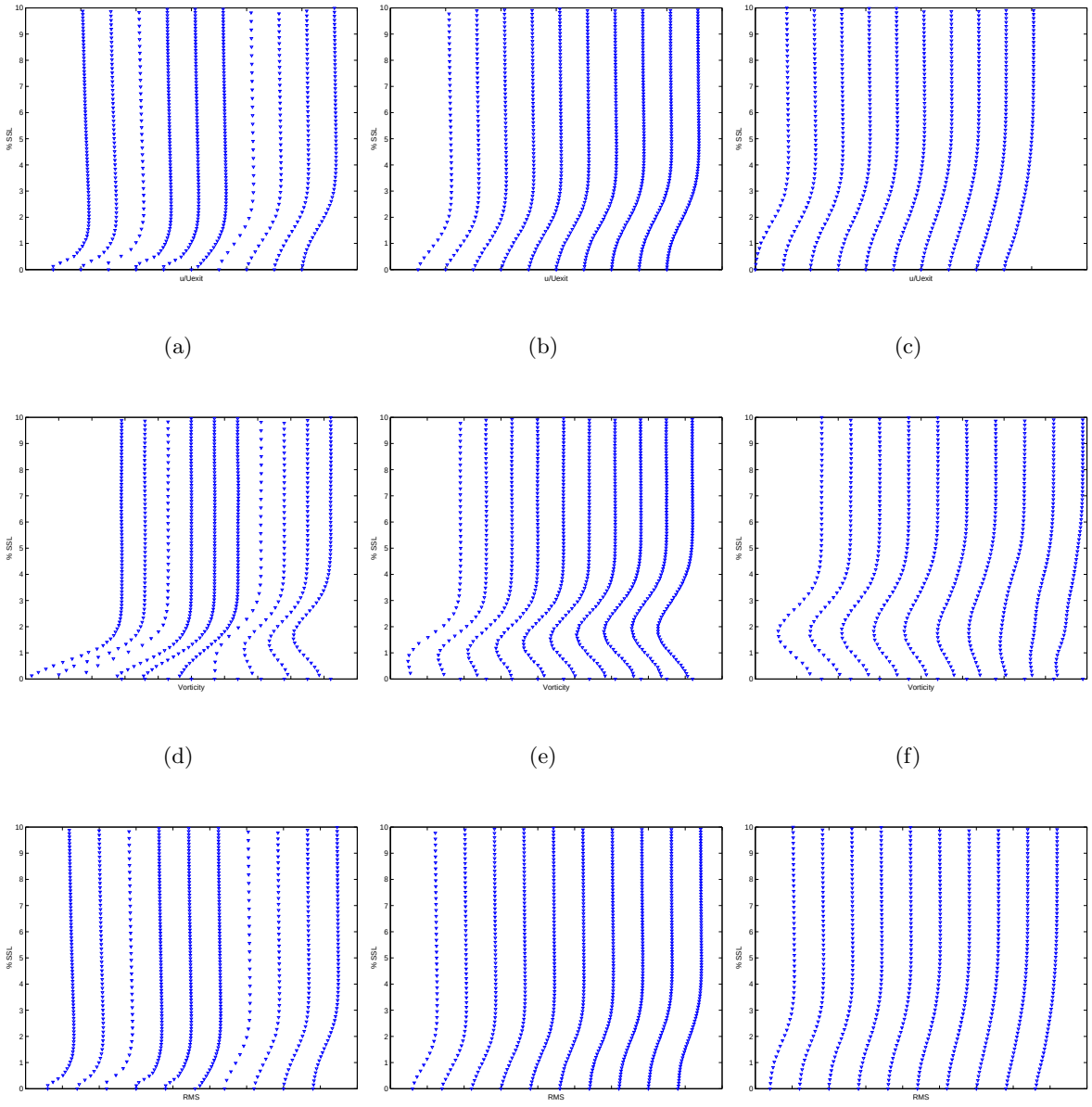

(a) (b) (c)

(d) (e) (f)

(g) (h) (i)

Figure 5.24: Velocity, Vorticity, and RMS velocity profiles for each view at $Re = 3.0 \cdot 10^4$, FSTI case B

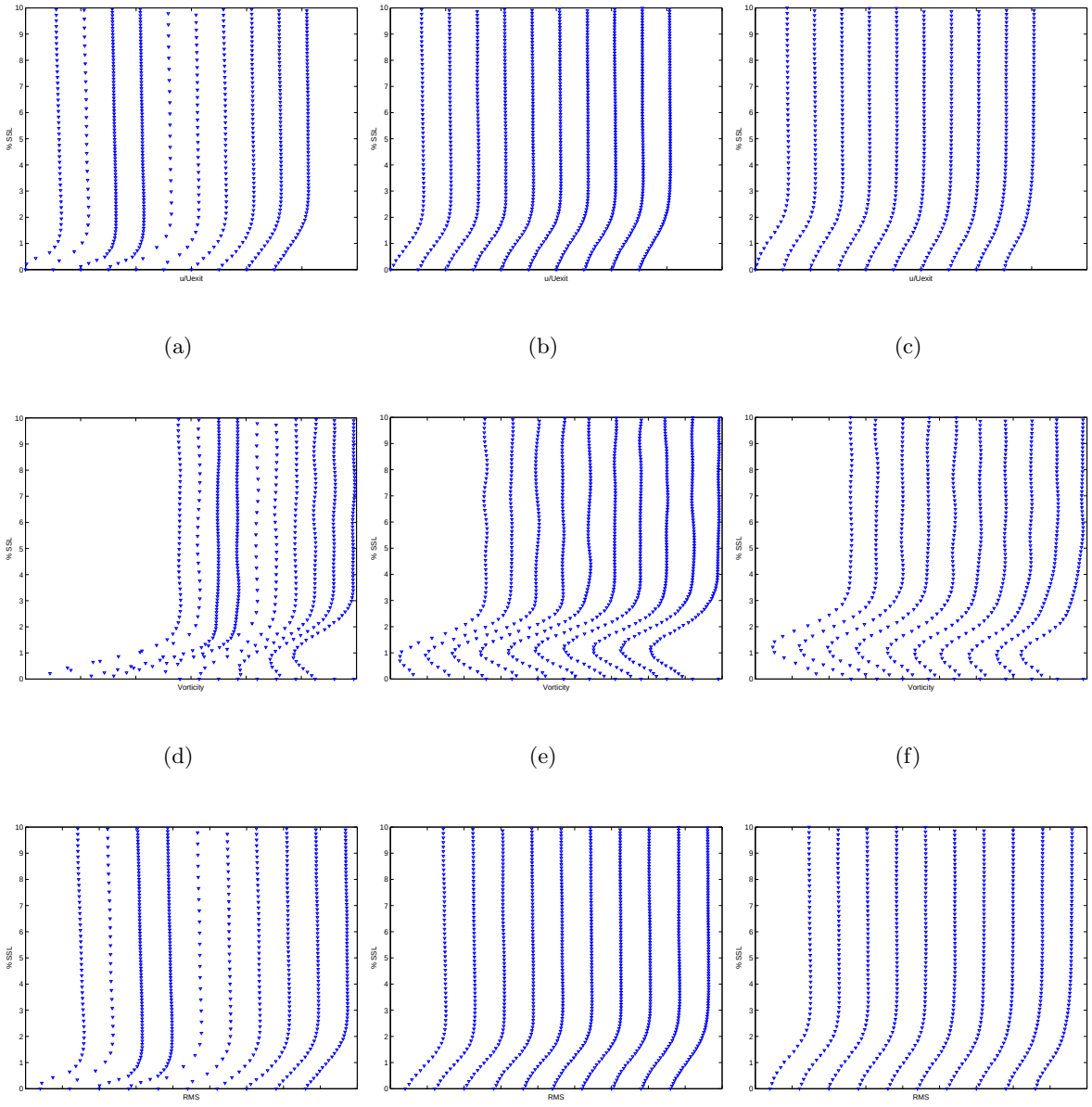

(a) (b) (c)

(d) (e) (f)

(g) (h) (i)

Figure 5.25: Velocity, Vorticity, and RMS velocity profiles for each view at $Re = 5.0 \cdot 10^4$, FSTI case B

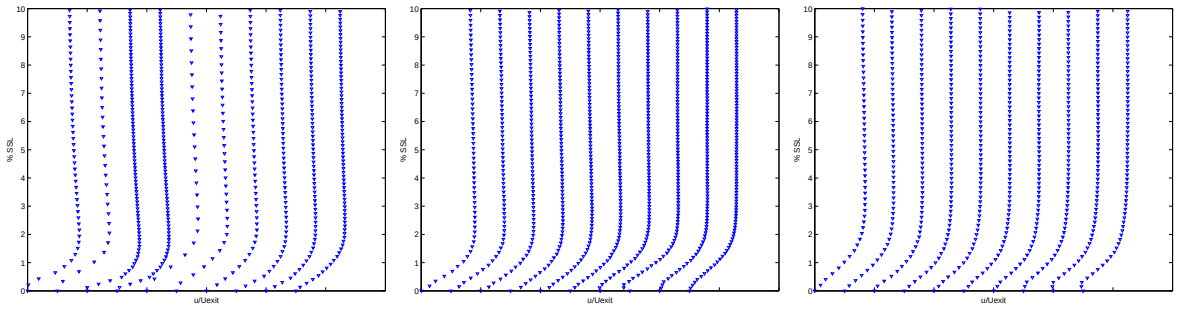

(a) (b) (c)

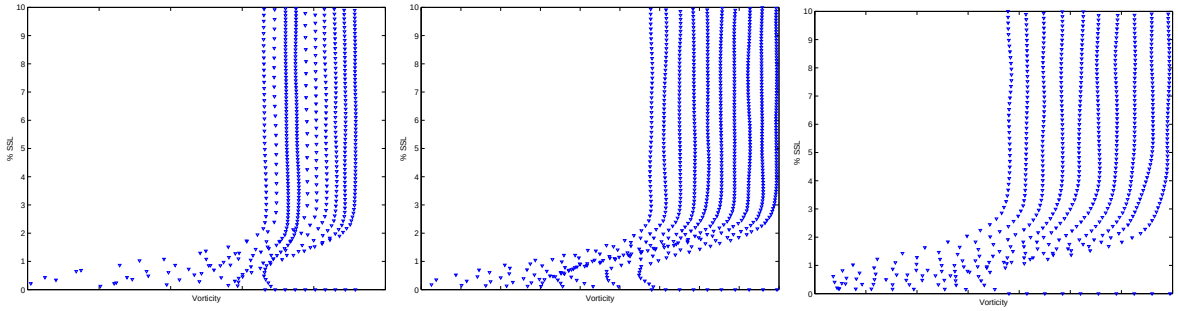

(d) (e) (f)

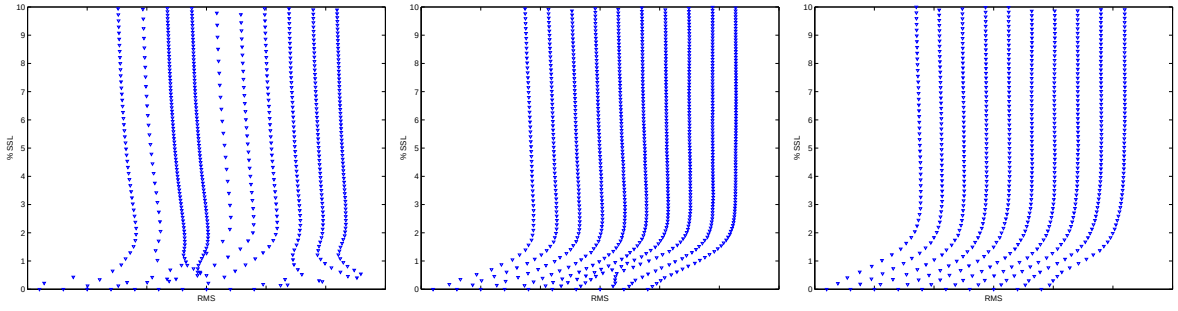

(g) (h) (i)

Figure 5.26: Velocity, Vorticity, and RMS velocity profiles for each view at $Re = 10.0 \cdot 10^4$, FSTI case B

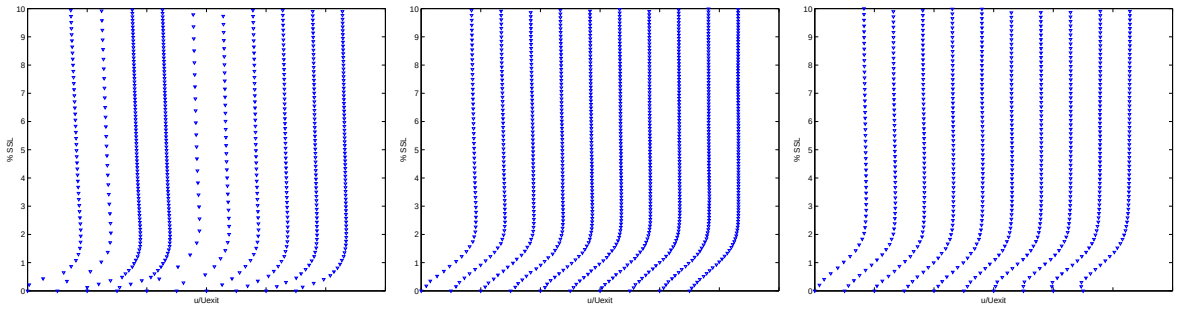

(a) (b) (c)

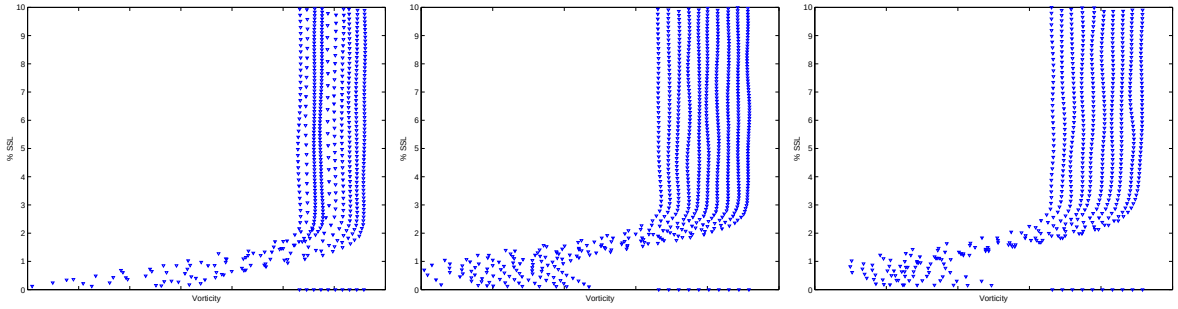

(d) (e) (f)

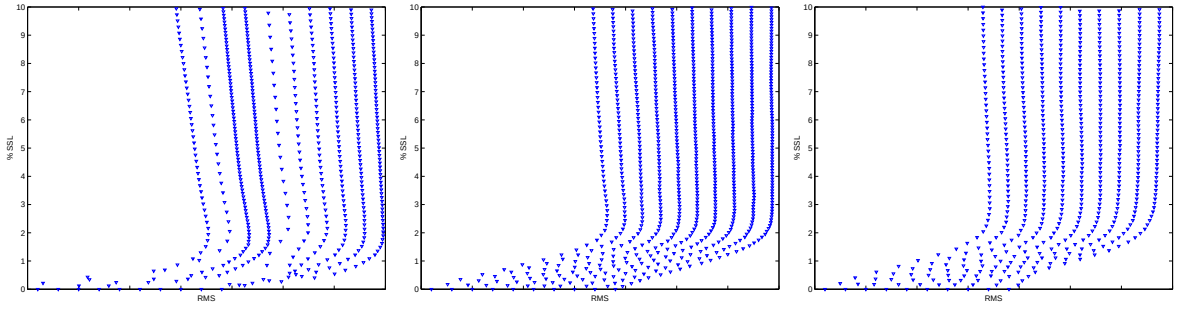

(g) (h) (i)

Figure 5.27: Velocity, Vorticity, and RMS velocity profiles for each view at $Re = 20.0 \cdot 10^4$, FSTI case B

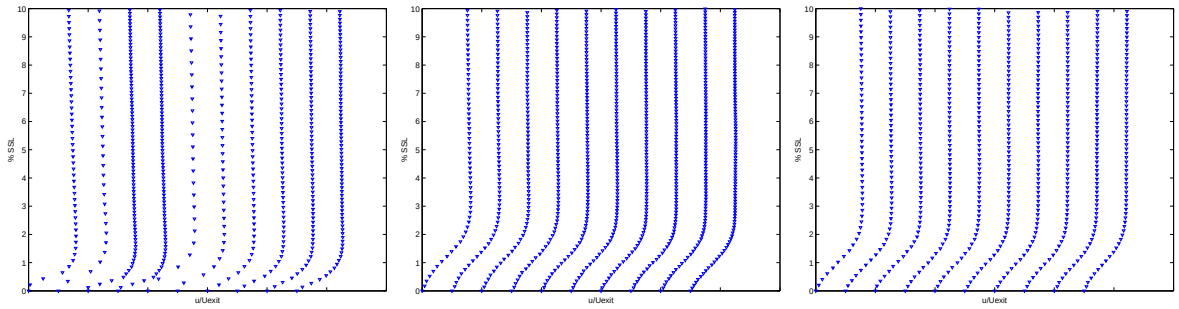

(a) (b) (c)

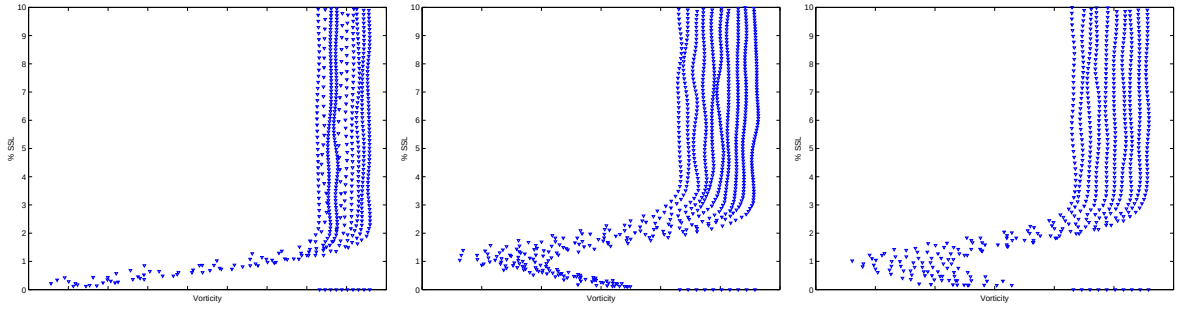

(d) (e) (f)

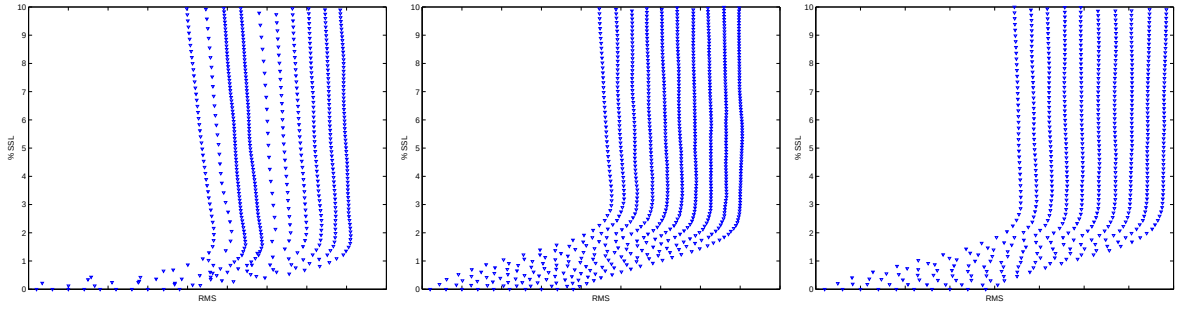

(g) (h) (i)

Figure 5.28: Velocity, Vorticity, and RMS velocity profiles for each view at $Re = 30.0 \cdot 10^4$, FSTI case B

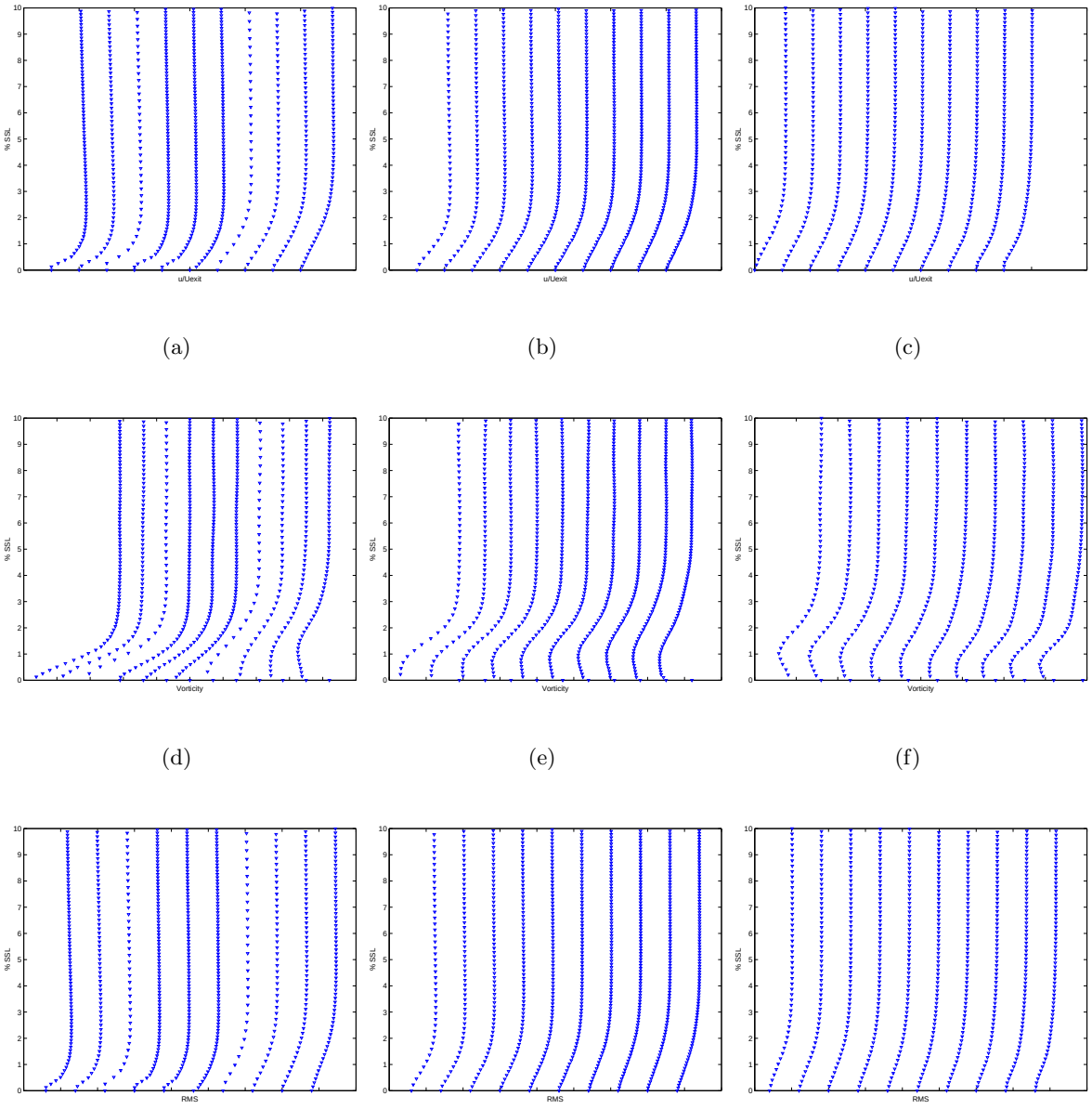

(a) (b) (c)

(d) (e) (f)

(g) (h) (i)

Figure 5.29: Velocity, Vorticity, and RMS velocity profiles for each view at $Re = 3.0 \cdot 10^4$, FSTI case C

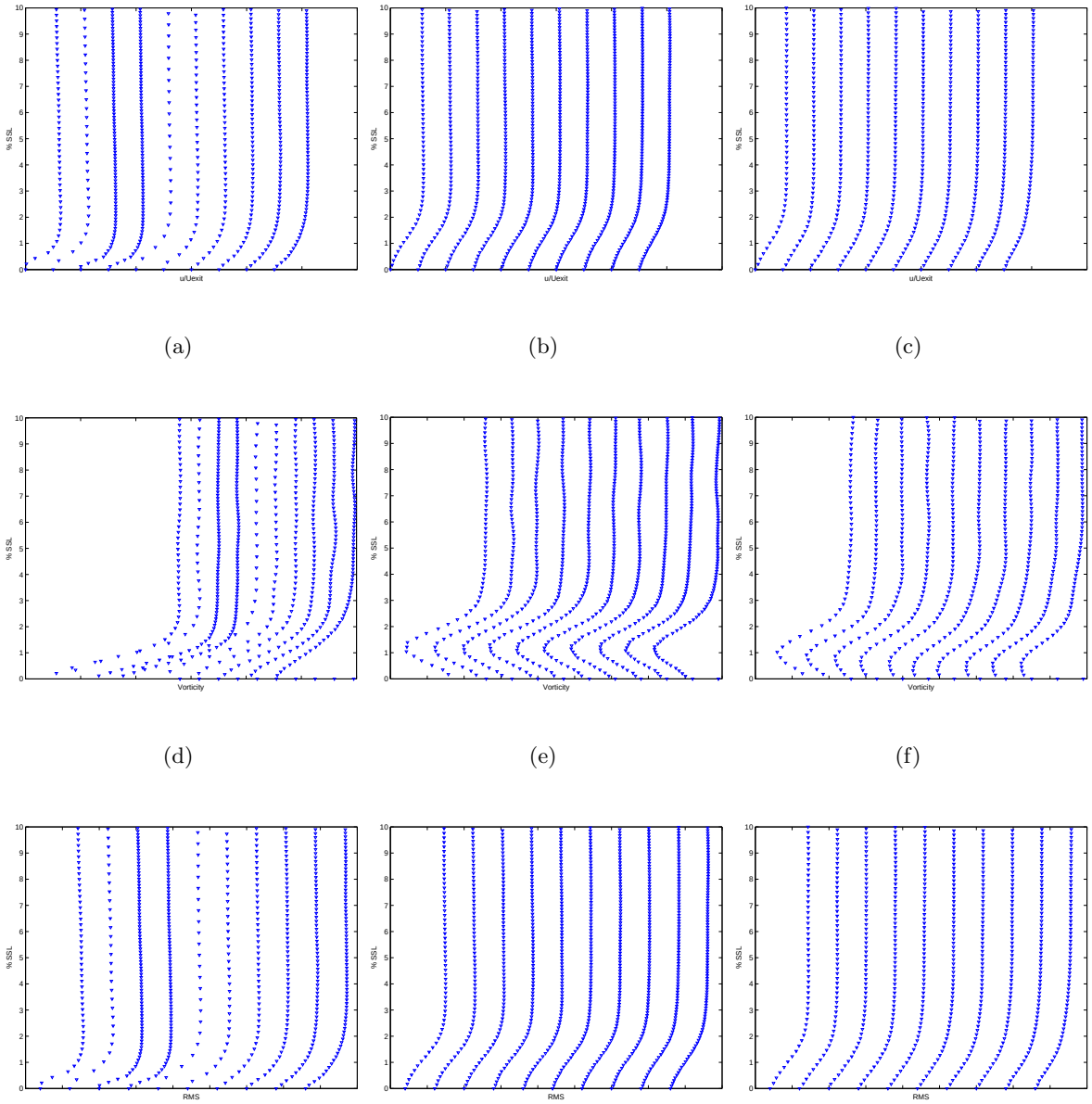

(a) (b) (c)

(d) (e) (f)

(g) (h) (i)

Figure 5.30: Velocity, Vorticity, and RMS velocity profiles for each view at $Re = 5.0 \cdot 10^4$, FSTI case C

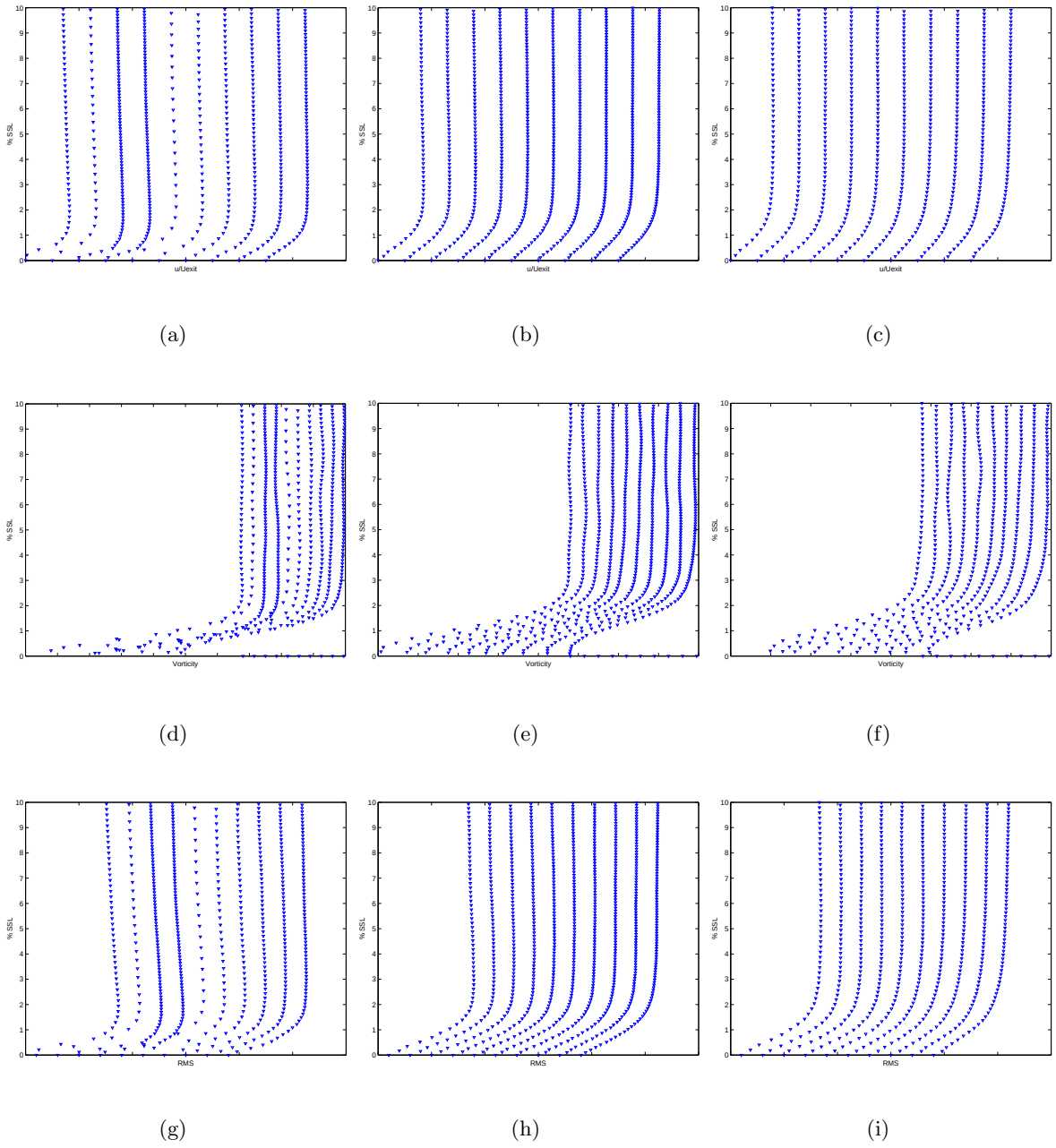

(a) (b) (c)

(d) (e) (f)

(g) (h) (i)

Figure 5.31: Velocity, Vorticity, and RMS velocity profiles for each view at $Re = 10.0 \cdot 10^4$, FSTI case C

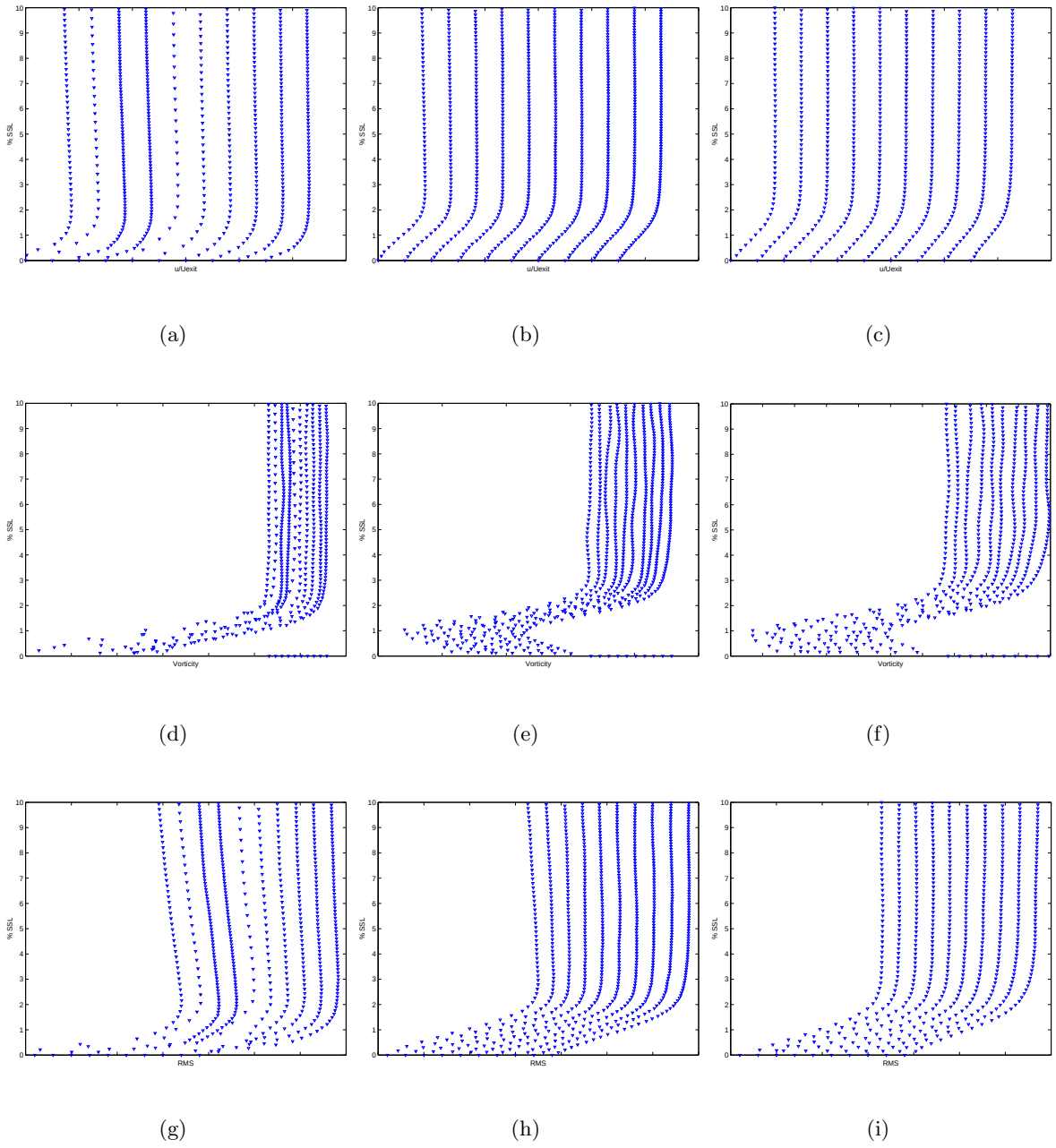

(a) (b) (c)

(d) (e) (f)

(g) (h) (i)

Figure 5.32: Velocity, Vorticity, and RMS velocity profiles for each view at $Re = 20.0 \cdot 10^4$, FSTI case C

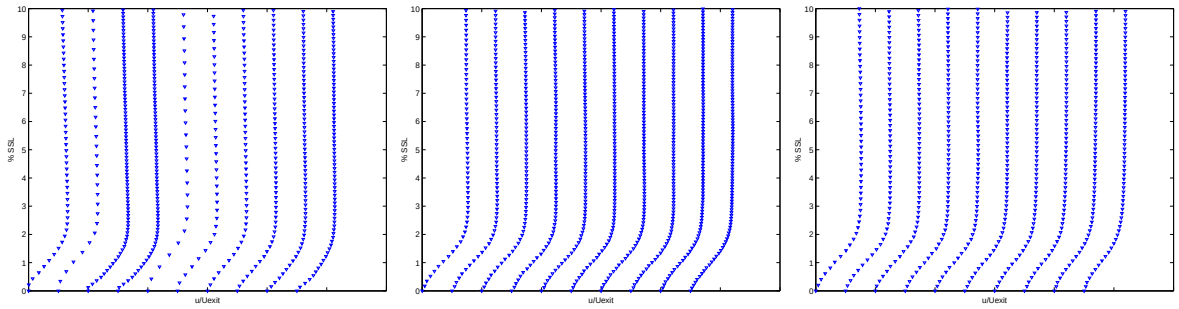

(a) (b) (c)

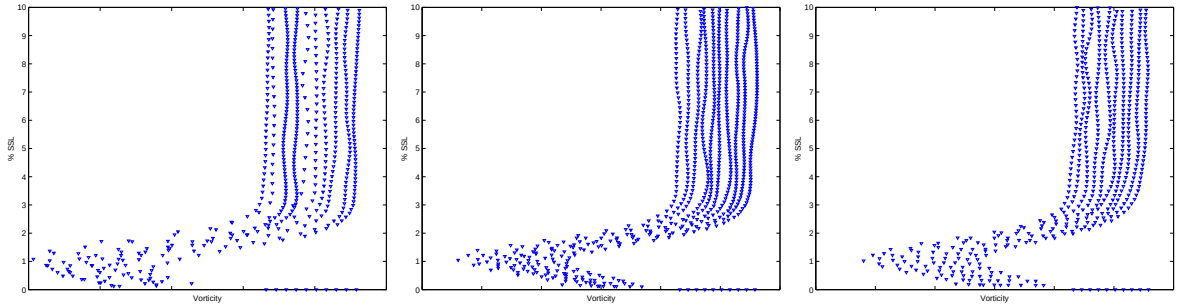

(d) (e) (f)

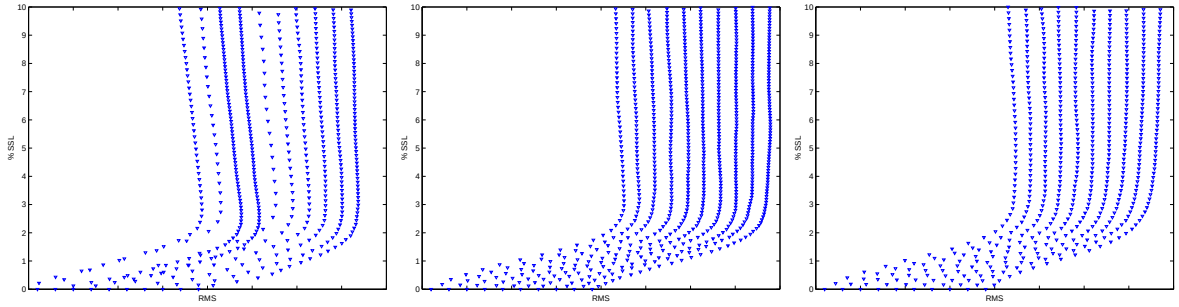

(g) (h) (i)

Figure 5.33: Velocity, Vorticity, and RMS velocity profiles for each view at $Re = 30.0 \cdot 10^4$, FSTI case C

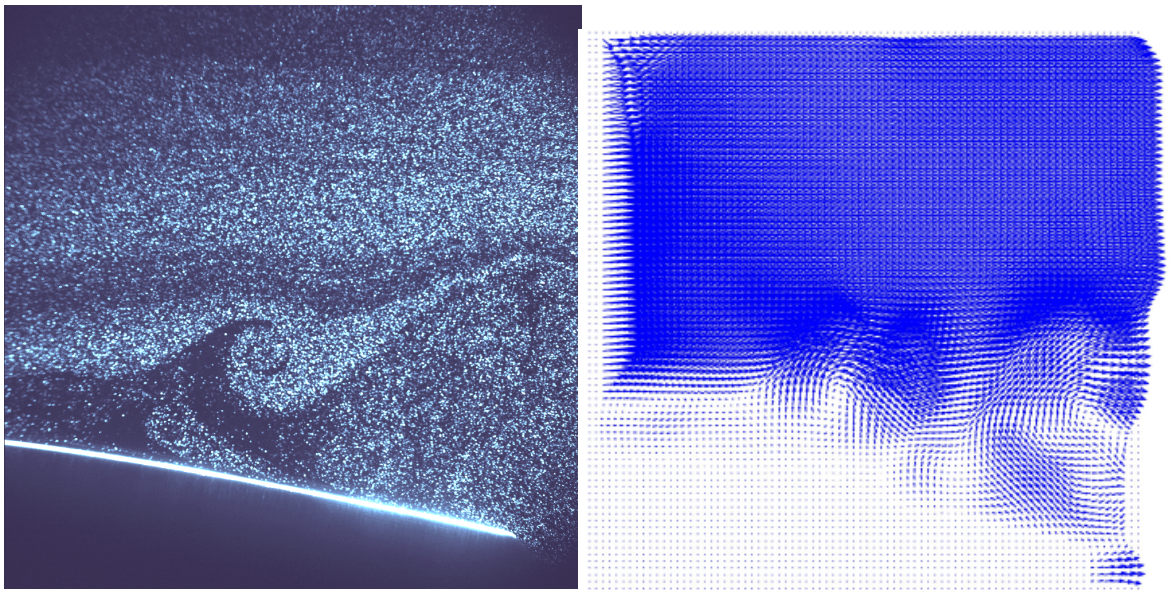

(a) Raw PIV image (false color).

(b) Velocity vector plot.

Figure 5.34: Turbulent flow structures in raw image and field plot for View # 3, $Re = 3.0 \cdot 10^4$, FSTI case A.

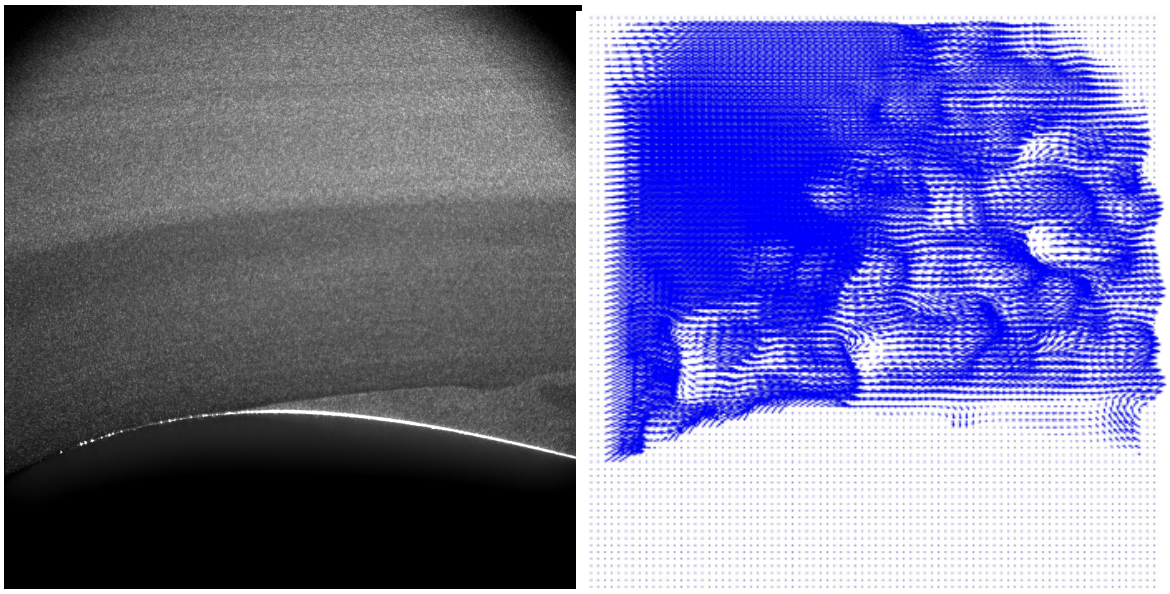

(a) Raw PIV image.

(b) Velocity vector plot.

Figure 5.35: Turbulent flow structures in raw image and field plot for View # 1, $Re = 5.0 \cdot 10^4$, FSTI case A.

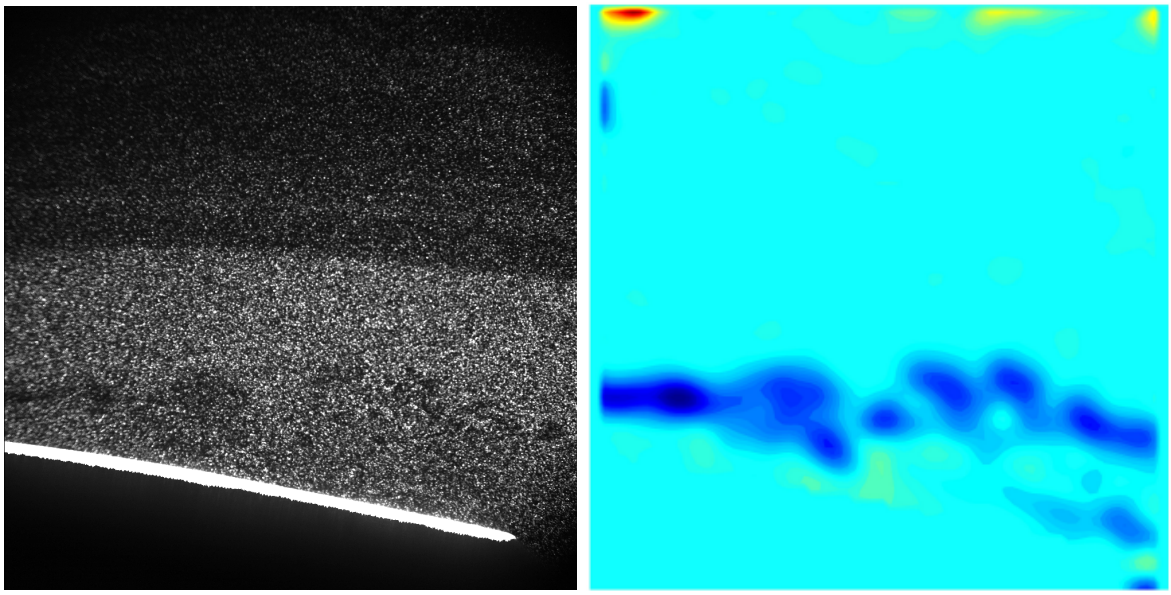

(a) Raw PIV image.

(b) Vorticity plot.

Figure 5.36: Turbulent flow structures in raw image and field plot for View # 3, $Re = 10.0 \cdot 10^4$, FSTI case A.

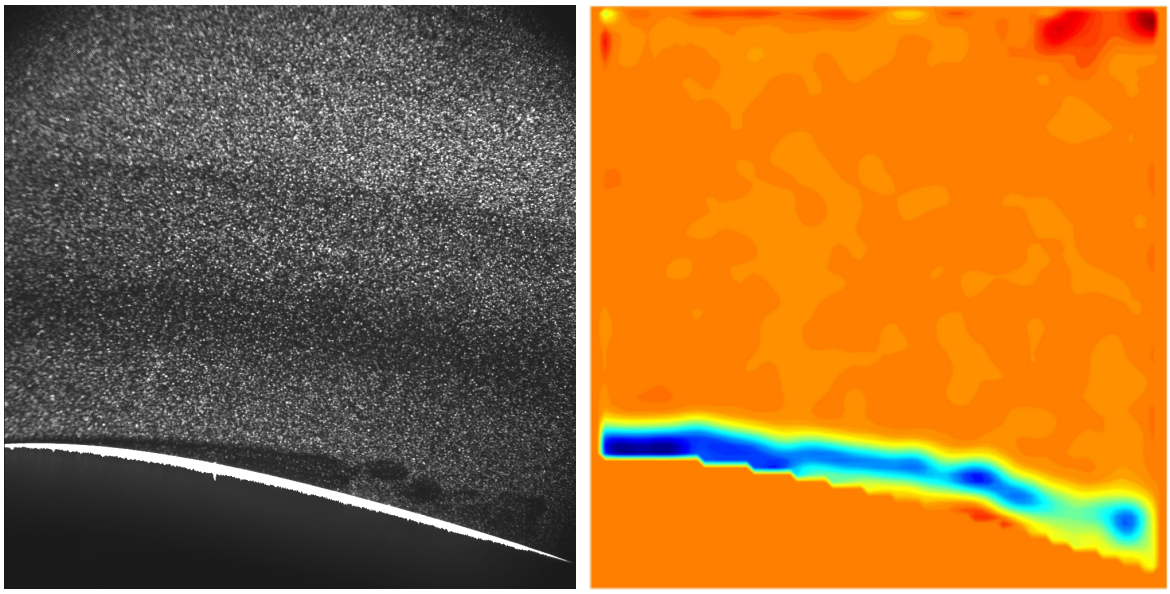

(a) Raw PIV image.

(b) Vorticity plot.

Figure 5.37: Turbulent flow structures in raw image and field plot for View # 2, $Re = 20.0 \cdot 10^4$, FSTI case A.

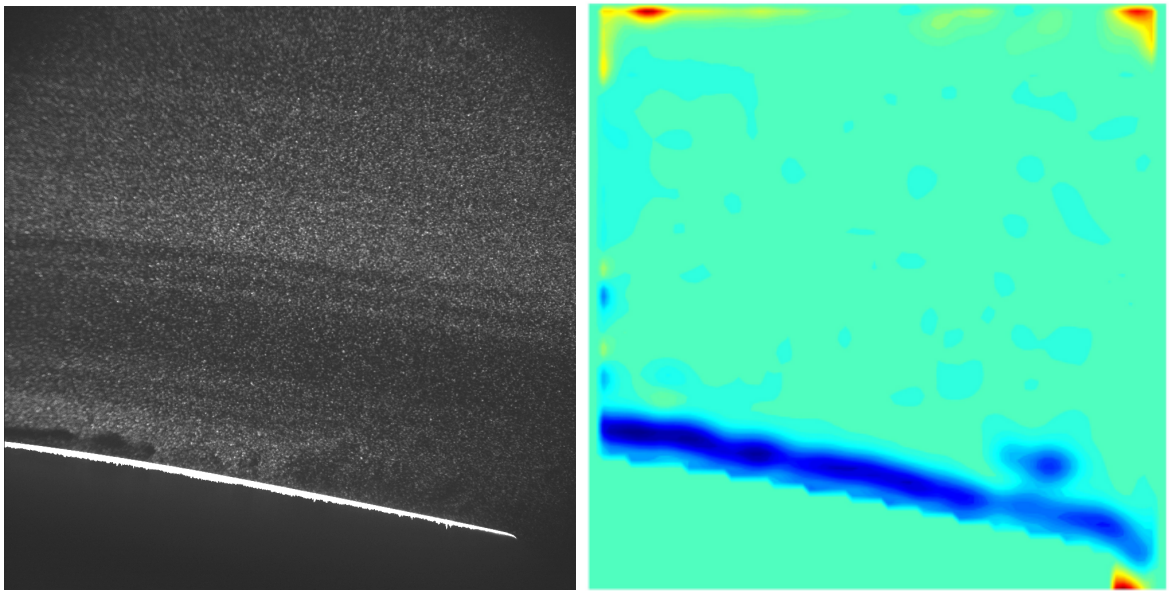

(a) Raw PIV image.

(b) Vorticity plot.

Figure 5.38: Turbulent flow structures in raw image and field plot for View # 3, $Re = 30.0 \cdot 10^4$, FSTI case A.

Chapter 6

Discussion

6.1 Summary of Flow Visualization

The purpose of the smoke-wire visualization study is to investigate the detailed transition and separation characteristics on low pressure turbine blades. The locations of separation and transition are determined to be approximately 45% and 77% of the suction surface length, respectively, based upon the smoke streamlines observed in the images, and appear to be independent of Re, turning angle, and free-stream turbulence intensity. The maximum size of the separation bubble is found to decrease with increasing Re, turning angle, and free-stream turbulence intensity. While the trends are consistent with previous research, these values indicate earlier separation than those of Murawski, the PIV measurements of the current study, and the flat plate study of Volino and Hultgren [11, 17]. This may be indicative of the difficulty of accurately determining quantitative values from qualitative images. Nonetheless, the smoke-wire technique has been demonstrated as a valid means of quantitatively determining the locations of separation and transition over a low pressure turbine blade at low to moderate FSTI for the purpose of determining the field of interest for more robust PIV measurements, and as a qualitative measurement of the height of the separation region.

6.2 Summary of Pressure Measurements

The pressure measurements were taken in order to obtain the pressure coefficient plots and compare the suggested separation points for the various test cases with those determined from the smoke-wire flow visualization experiments. The pressure coefficient plots indicate the flow separates around 60% SSL for each of the nine test cases studied. This value supports the current

PIV results as well as the work of Volino and Hultgren [17]. The separation point as determined from the pressure coefficient does not appear to move much for this small range of Re and all three exit angles. Compared to theory, however, the plots indicate a marked decrease in the magnitude of the pressure gradient, breaking from the theoretical curve at roughly 30% SSL. This disparity is undoubtedly due to the extremely low Re range of the current experiments in comparison to the theoretical calculation of the design curve. The pressure gradient for the experimental flow conditions is not expected to match the design curve for the PAK-B. Note that an XFoil calculation at these low Re numbers indicates a similar break from the design curve as discussed in Appendix B.

6.3 Summary of PIV Measurements

The purpose of the *preliminary* PIV runs was to show the validity of the PIV setup and processing (§5.1.1). The raw images from these runs offer some of the most vivid shots of the separation region over low pressure turbine blades to date. The resulting profiles and RFP contours show-cased the full flow field and bi-directional capabilities of the PIV method employed. The early runs also illustrated the value of the single image pairs for the study of unsteady flow structures.

The detailed PIV study (§5.1.2) solidifies the findings of the earlier flow visualization and pressure experiments and sheds new light on the effect of Re and FSTI on the separation region over low pressure turbine blades. The field plots clearly illustrate the geometry of the region of separation. The separation point location is considered to be the left-most negative u-velocity component near the blade wall for the cases where separation is clearly indicated in the plots. The values are listed in terms of %SSL in Table 6.1. There is no significant movement of the separation point with an increase in Re in this range, but the flow appears to separate later with an increase in FSTI. Further insight into the effect of Re and FSTI on the separation region is gained by inspecting the area of reversed flow for the different cases. The average area of reversed flow is listed in cm^2 in Table 6.2. The standard deviation for each set of 112 image pairs is also indicated as a gage of how unsteady the separation region size is. For high Re and FSTI, the area drops to insignificant values accountable to the few *bad* vectors in the output files. Plotting the area of the reversed flow against the Re for the three values FSTI clearly illustrates the relative importance of Re and FSTI with regard to separation. A plot of the summed areas from camera views one and three are shown in Figure 6.5 where it has been non-dimensionalized by suction surface length squared (SSL^2). This can be taken as the total size of the separation bubble. The error bars indicate the standard deviation and is a measure of the degree of variation of separation bubble size over the

run. The figure indicates that at a Re of $20.0 \cdot 10^4$ the size of the region of reversed flow is about the same as for a lesser Re and FSTI case B or C. In fact, no separation region is indicated by the field plots for Re higher than $10.0 \cdot 10^4$, and only at the lowest Re is there any indication of separation for FSTI case B. When Re is taken into account by multiplying the separation bubble area by Re/SSL^2, it is noted that the size of the separated region is approximately linear versus Re, except in the cases of laminar flow (low FSTI and $Re < 10 \cdot 10^4$). This is shown in Figure 6.5. The anomaly of the low FSTI points at low Re is of course due to the lack of transition present in the separated region preventing the flow from quickly reattaching. Stated in dimensional terms, for turbulent flow the product of the free-stream velocity and separation bubble size varies linearly with velocity. This may be useful as a guideline in issues related to blade design or CFD validation.

The point of separation and the area of reversed flow determined for each image pair indicate how the flow structures change with time for a given set of conditions, something not possible with averaged single-point measurements taken with a uni-directional hot-wire. The profile plots also show the size and movement of the separation region, and are a better indication of reattachment length than the field plots. The velocity profiles are also a better indicator of the separation point for higher Re and FSTI cases. The locations of transition and reattachment are not easy to track with the PIV results. Transition is clearly observed in the raw image files, and further analysis based upon intermittency may allow for a better understanding of the effect of Re and FSTI on transition.

6.4 Conclusions of the Study

The separation point was determined to be between 63.4% SSL and 67.6% SSL based on the velocity measurements. This is consistent with the flat plate study of Volino, where separation was observed between 63% and 67% SSL, though not with the work of Murawski, where the separation point was observed further downstream between 74% and 81% of the axial chord. Murawski observed not only later separation, but also more movement of the separation point with increasing Re. The cause of these differences probably stems form the tunnel conditions and the how the data was acquired. Though Murawski and Volino each used hot-wire probes, it is possible that Murawski could not place the probe as close to the blade surface. The aspect ratio and the number of blades in Murawski's cascade is also different than the cascade for the current study [17] [11]. Volino also determined separation at a Re of $30.0 \cdot 10^4$, which was not clear in the present study based upon the reversed flow region. However, the velocity profiles do indicate an inflection point from around 67% SSL and apparent reattachment near the trailing edge for the clean tunnel case.

The variation in the size of the separation region with time and varying Re and FSTI are valuable for numerical code validation. Contaminated flow during hot-wire measurements downstream of the turbulence grid makes deriving the transition start and end points from intermittency unlikely, however, the transition location based upon smoke-wire and PIV flow visualization is consistent with previous studies.

6.5 Future Work

Further analysis of existing data may improve the quality of the various plots and profiles determined in the current study. The window size may be decreased to increase the accuracy of the PIV algorithm near the blade wall. The hot-wire measurements taken downstream of the turbulence grid may also be filtered in order to minimize the effect of the contamination and facilitate a calculation of the transition start and end locations via a method similar to that of Volino and Hultgren [17]. The tangential velocity profiles may also be determined for other locations along the suction surface length, allowing a more accurate determination of the separation point, especially in the cases of higher Re and FSTI. Each pair of images recorded may be inspected more carefully in order to study unsteady effects such as the shedding vortices observed at the transition point for the lower Re flow cases in the current study.

Several modifications to the PIV setup may further advance knowledge of separated flows over the low pressure turbine blade cascade model with more experiments. By introducing a smooth cylinder upstream of the cascade and moving it in phase with typical wake disturbances from other blade sections in a gas turbine engine will improve the validity of the cascade model. The camera magnification may also be increased in order to increase the resolution in the smallest separation regions for higher Re and FSTI cases; this may be particular helpful in measuring separation in regimes of increased Re and FSTI.

$Re \cdot 10^4$	$FSTI$	$\%SSL$
3	1%	63.4
5	1%	63.72
10	1%	64.85
3	5%	67.6

Table 6.1: Separation point in terms of SSL for the flow visualization experiments.

		View # 1		View # 3		Total area	
$Re \cdot 10^4$	FSTI	Area (cm^2)	StdDev	Area (cm^2)	StdDev	area/SSL^2	area$\cdot Re/SSL^2$
3	A	0.81	0.12	3.04	0.63	0.0166	0.500
5	A	0.81	0.17	2.58	0.76	0.0150	0.734
10	A	0.39	0.10	1.40	0.48	0.0077	0.775
20	A	0.25	0.02	0.25	0.04	0.0022	0.433
30	A	0.18	0.04	0.34	0.06	0.0022	0.676
3	B	0.33	0.08	0.31	0.10	0.0029	0.083
5	B	0.45	0.05	0.45	0.05	0.0039	0.195
10	B	0.34	0.09	0.41	0.03	0.0032	0.325
20	B	0.25	0.07	0.30	0.05	0.0024	0.476
30	B	0.24	0.04	0.33	0.06	0.0025	0.740
3	C	0.29	0.06	0.25	0.03	0.0023	0.070
5	C	0.45	0.05	0.46	0.06	0.0039	0.197
10	C	0.21	0.03	0.24	0.04	0.0019	0.195
20	C	0.23	0.04	0.25	0.04	0.0020	0.416
30	C	0.47	0.14	0.31	0.06	0.0033	1.013

Table 6.2: Area of the reversed region for varied Re and FSTI from the PIV experiments.

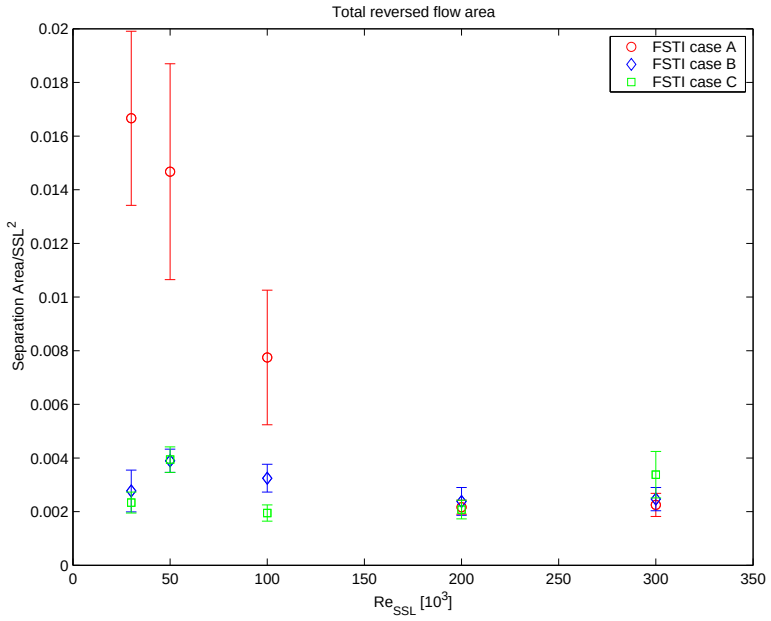

(a) Non-dimensionalized using SSL.

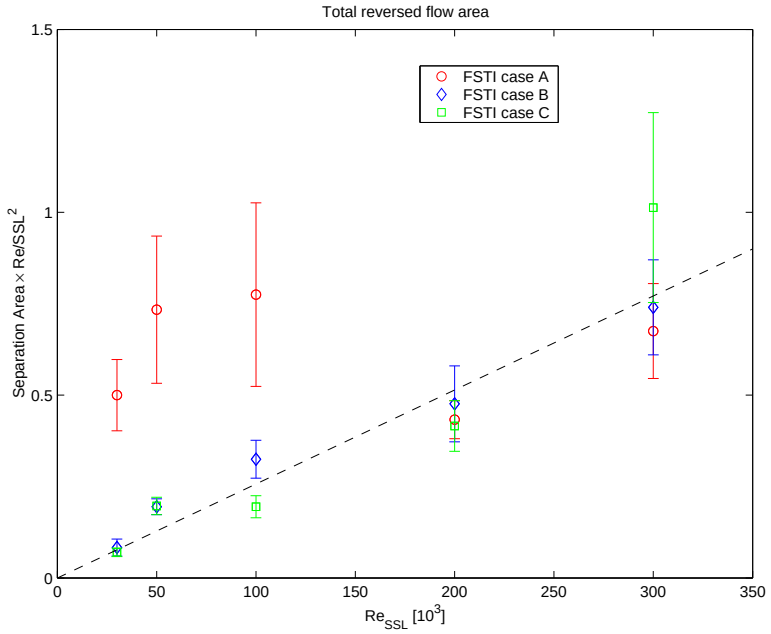

(b) Non-dimensionalized using SSL and Re.

Figure 6.1: Approximate area of reversed flow normalized by SSL^2 and $SSL^2 \cdot Re$ with increasing Re and FSTI.

Appendix A

Tow Tank Experiments

Prior to wind tunnel testing, a mock turbine blade cascade was tested in a tow tank facility to investigate the diagnostic tools. These results are presented below.

A.1 Test Facilities

The tow tank is approximately 4.0 m long by 0.38 m wide and deep, with a capacity of approximately 1000 gallons. A carriage is pulled along two rails spanning the length of the tank with a syncromesh pulley and timing belt system to prevent slippage. A 1.6 kW (2 hp) motor drives the pulley up to 5 m/s. A three-blade cascade was mounted to the carriage with two streamlined struts between endplates. Before each run the fluid was quiescent and essentially turbulence free; along with the inadequate cascade arrangement, this makes any results from the tow tank runs valuable only in testing the diagnostics.

The water is seeded with 40 micron diameter silver-coated hollow glass spheres. For the preliminary tow tank runs, a 5 W Argon-Ion laser was used to create a laser sheet across a portion of the tank as shown in figure A.1. For higher Re runs a 50 mJ pulsed Nd:YAG laser is used in sync with the camera to avoid the streaky images that result from higher speed runs with continuous illumination. A Pulnix TM-6701 with a square pixel CCD array (648x484 pixels) and a frame rate of 60/120 Hz, or a Sony XC-55 (640x480 pixels, 30 Hz) are positioned perpendicular to the laser sheet. The images were captured using a Matrox Pulsar or Meteor II PCI frame grabbing software with a PC in real-time. The Pulnix was mounted on a tripod and images were acquired for an instant as the carriage passed in front of the camera for preliminary results. For later runs, the remote head Sony camera was attached to the outside of the carriage to allow measurement of unsteady flow characteristics, as shown in figure A.2. WaLPT as described below is used to extract

two-dimensional velocity and vorticity fields from the images.

A.2 Turbine Blade Models

Turbine blade models with an approximate chord length of 114 mm, a span of 203 mm and a suction surface length of 152 mm have been constructed using an SLA at the Rapid Prototyping Laboratory at the University of Kentucky. The geometry of the blade is based upon the Pratt & Whitney PAK-B. For the tow tank runs two of the three blades in the cascade were molded from the original SLA model as shown in figure A.3. The third blade also has a clear trailing edge extension formed to the pressure side of the blade to direct the flow in the turned direction behind the middle blade. As previous studies have reported, however, trailing edge extensions alter the pressure gradient and thus the tow tank runs are not run at realistic operating conditions [11].

A.3 Tow Tank Results

For the first snapshot tow tank runs in the proof of concept stages of our research, several runs produced clear illustrations of separation on the suction surface of the middle blade. Figure A.4 shows the velocity and vorticity plot for a run at a Re_{SSL} of 13,000. Since the experiment was conducted in the tow tank, the FSTI is essentially zero. Separation can clearly be seen, but the resolution in these measurements is not great enough to adequately describe the separation bubble characteristics in detail. The image shows the capability of the DPIV process in determining the velocity field near the blade wall, however. It should be noted that even for these roughly modeled runs the separation bubble and vorticity diminished with increasing Re as expected.

Further tow tank runs allowed for unsteady measurements with the use of the "flying PIV" configuration (figure A.2). With these runs it was possible to average the velocity and vorticity fields for a sample of several image pairs. The size of this sample was dependent upon the quality of the images and the speed of the run. For faster runs, the carriage speed reduces the amount of time the cascade spends in the region of optimal laser sheet intensity consequently reducing the number of image pairs with sufficient illumination. Figure A.5 shows the resulting velocity and vorticity field plots for an average of 15 image pairs at a Re_{SSL} of approximately 38,000 based on suction surface length. The plot is another example of how the PIV technique has enabled us to study the separation region itself. It should be noted that this separation region appeared to be a steady flow characteristic based upon the examination of the individual image pairs.

To further test our procedure, we re-processed this sample isolating a smaller region around

the separation bubble to increase the resolution in that area. The result is the plot shown in figure A.6. This ability will be useful in the more rigorous wind tunnel PIV tests where a similar detailed study of much smaller separation bubbles will be necessary.

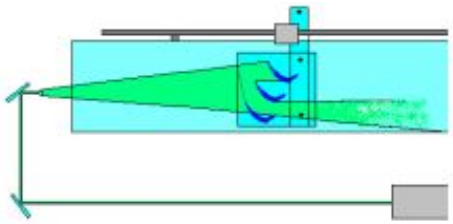

Figure A.1: Optical arrangement for tow tank experiments.

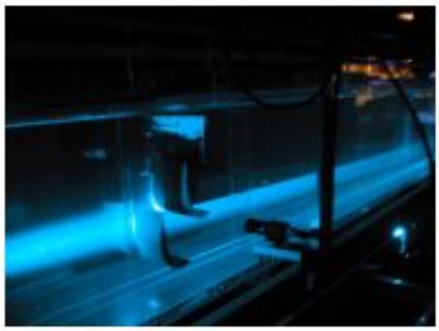

Figure A.2: Photograph of "flying PIV" configuration showing carriage mounted camera.

Figure A.3: 3 blade tow tank cascade.

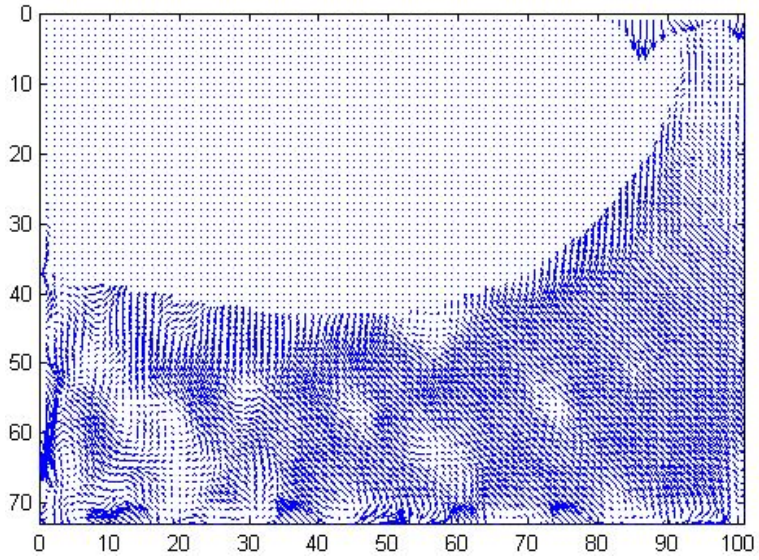

(a) **Velocity.**

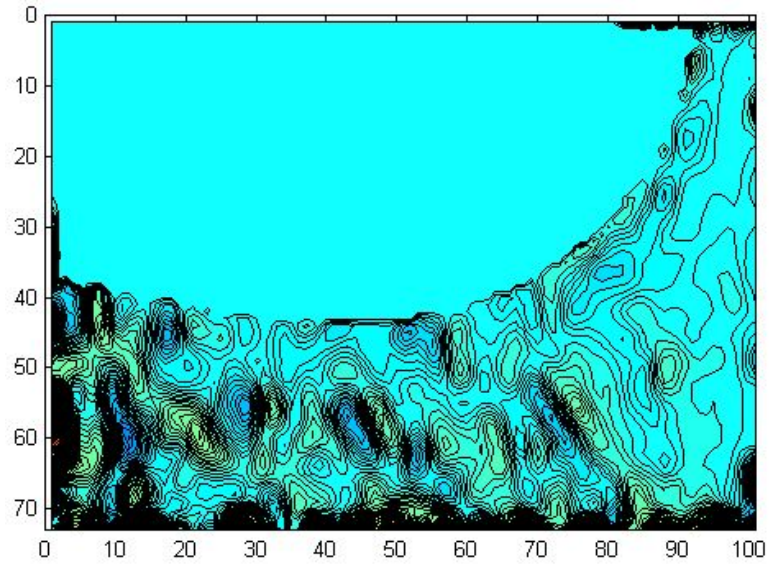

(b) **Vorticity.**

Figure A.4: Instantaneous velocity and vorticity plots for $Re_{SSL} = 1.3 \cdot 10^4$.

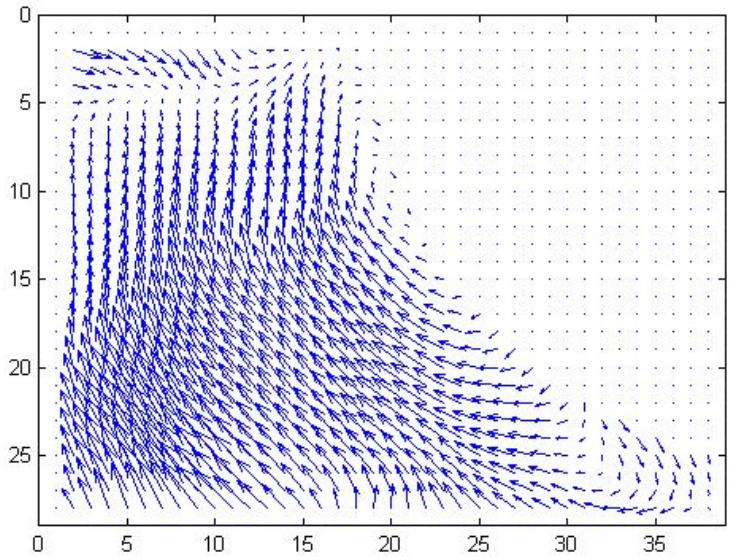

(a) **Velocity.**

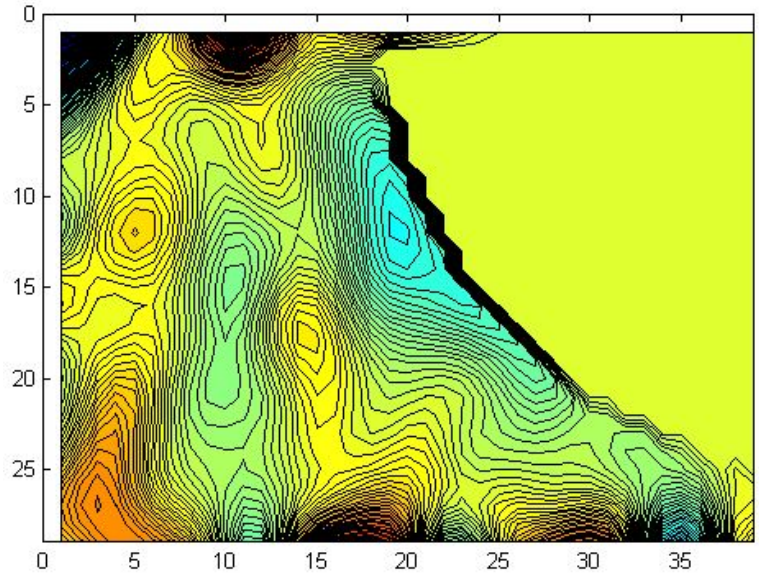

(b) **Vorticity.**

Figure A.5: Averaged velocity and vorticity plots for $Re_{SSL} = 3.8 \cdot 10^4$.

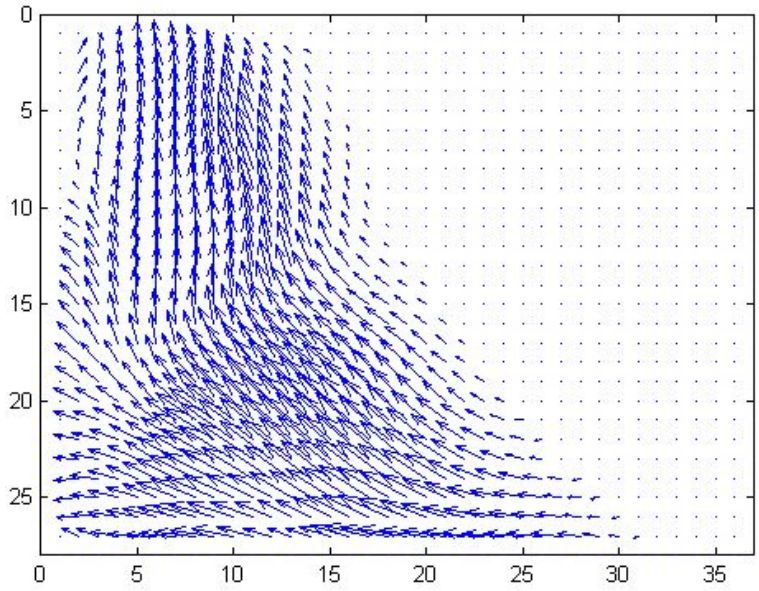

(a) **Velocity.**

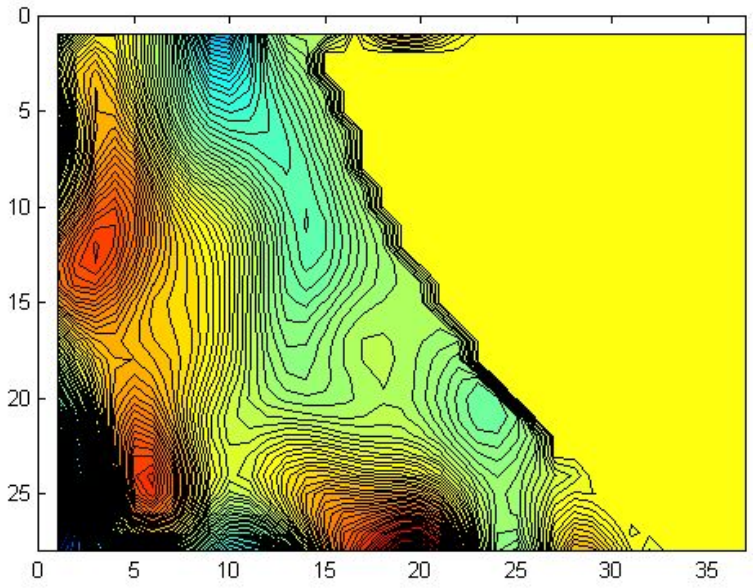

(b) **Vorticity.**

Figure A.6: Averaged velocity and vorticity plots for $Re_{SSL} = 3.8 \cdot 10^4$ at increased magnification.

Appendix B

LPT Airfoil Model Using an Inverse Design Method

After wind tunnel testing, XFoil v. 6.93 software is used to a model the PAK-B cascade with an airfoil. The airfoil is then examined under different conditions in XFoil and compared with previous studies. These results are presented below.

B.1 Generating the Airfoil Geometry

In "traditional" airfoil design, airfoils are designed by generating the geometry first and determining the resultant pressure curve. The inverse design method takes the pressure curve as input and generates the geometry directly. We have used the inverse design method on the PAK-B C_p curve to generate an equivalent single foil geometry suitable for future studies of separation.

Using XFoil, it is possible to modify the velocity curve of a standard airfoil to match that of the theoretical PAK-B turbine blade. First, the standard velocity curve for the NACA 0012 is generated. Then points are added to modify the shape of the velocity curve over the upper surface of the airfoil as shown in Figures B.1(a) and B.1(b). Only the curve on the upper surface is modified because the flow under the airfoil is not expected to have a significant effect on the pressure gradient over the upper surface. The inverse solver in XFoil is then used to generate the airfoil geometry corresponding to the prescribed velocity curve on the upper surface as shown in Figure B.2.

B.2 Airfoil Performance

Once the airfoil geometry has been generated with the inverse calculation, a viscous analysis of the pressure coefficient, boundary layer, skin friction coefficient, and the displacement and momentum thicknesses may be executed for different flow conditions. The airfoil is analyzed for zero angle of attack and a Re_c from $5 \cdot 10^4$ to $30 \cdot 10^4$ as in the previous experiments. Note that the Reynolds number is now based upon the chord length, c, of the airfoil. The separation point is then deduced from these plots along with the relative size and geometry of the separation region. Regions of reversed flow are clearly identified by a negative skin friction coefficient, and the transition point is output by XFoil in terms of percent chord.

The default analysis in XFoil models the FSTI of the flow over the airfoil as that encountered in a typical clean wind tunnel. The FSTI may be increased by varying the factor of the frequency of velocity fluctuation above which XFoil considers the flow to be turbulent. Since this value is not resolved into a FSTI parameter that is directly comparable to that used in previous studies, this value is adjusted until the point of the onset of transition is consistent with the expected location based upon the results of Volino [17].

B.3 Results

The pressure distribution and boundary layer profiles for the various analyses are shown in Figures B.3(a) through B.3(f). The pressure distribution for the low Re cases clearly indicates a predicted separation point between 50% c and 60% c. The boundary layer profiles also illustrate inflection points and reversed flow within the boundary layer for the clean cases for Re of $5 \cdot 10^4$ and $10 \cdot 10^4$. For the increased FSTI cases, reversed flow is only clear from the boundary layer profiles for a Re of $5 \cdot 10^4$.

The displacement and momentum thicknesses for the XFoil analyses are shown in Figures B.4(a) through B.4(f). These plots are a good indicator of the growth of the boundary layer and the effect of Re and FSTI on the size of the separation region. The clean cases show that the size of the boundary layer increases steadily for Re of $5 \cdot 10^4$ and $10 \cdot 10^4$. At a Re of $5 \cdot 10^4$ the maximum size of the boundary layer near the trailing edge is about 7.5% c. For a Re of $30 \cdot 10^4$ the boundary layer grows to a maximum of about 0.7% c before decreasing and then growing again to the trailing edge. The sudden drop indicates the point of transition and the subsequent growth of the turbulent boundary layer. For the increased FSTI cases the size of the boundary layer decreases significantly for each case, and transition is observed at a Re of $10 \cdot 10^4$.

The skin friction coefficients are shown in Figures B.5(a) through B.5(f). These plots suggest reversed flow where the skin friction coefficient is negative, and thus offer a good indicator of separation and reattachment of the flow. For the lowest Re and FSTI the skin friction is first negative around 58% c and remains negative for the length of the airfoil. By increasing the FSTI and holding Re at $5 \cdot 10^4$ transition is induced earlier and the skin friction nearly achieves a positive value again at the trailing edge. Fot the highest Re and low FSTI case the skin friction coefficient indicates a very small region of reversed flow beginning around 62% c and reattachment near 75% c. For the highest Re and FSTI case, where transition is predicted around 67% c, the skin friction coefficient drops at 67% c, but remains positive over the length of the airfoil.

B.4 Discussion

The results of the XFoil analysis are encouraging. The prediction of the separation point and the relative size of the region of reversed flow are consistent with PIV measurements of the current study and the flat plate study by Volino [17]. Further, if future testing verifies the accuracy of the airfoil model, the skin friction plots generated in XFoil may provide a better indication of reattachment than the PIV measurements alone. The predictions of the onset of transition for the various test cases in particular are remarkably consistent with those offered by Volino [17]. The transition locations from the XFoil output and the flat plate study for each test case are presented in Table B.1. The results of the XFoil analysis suggest the possibility of simplifying the wind tunnel study by replacing the cascade model with an airfoil resulting in a pressure distribution matching that of the theoretical PAK-B blade. While more robust validation of XFoil predictions is necessary before the airfoil model may progress to the wind tunnel, this preliminary study certainly warrants further development of this novel concept.

	$Re_S SL/Re_c$	Volino	XFoil
Low FSTI	50,000	1.0	1.0
	100,000	0.88	0.88
	200,000	0.76	0.78
	300,000	0.76	0.74
High FSTI	50,000	0.85	0.85
	100,000	0.78	0.76
	200,000	0.72	0.70
	300,000	0.66	0.67

Table B.1: Tracking the point of onset of transition (% SSL and x) with XFoil.

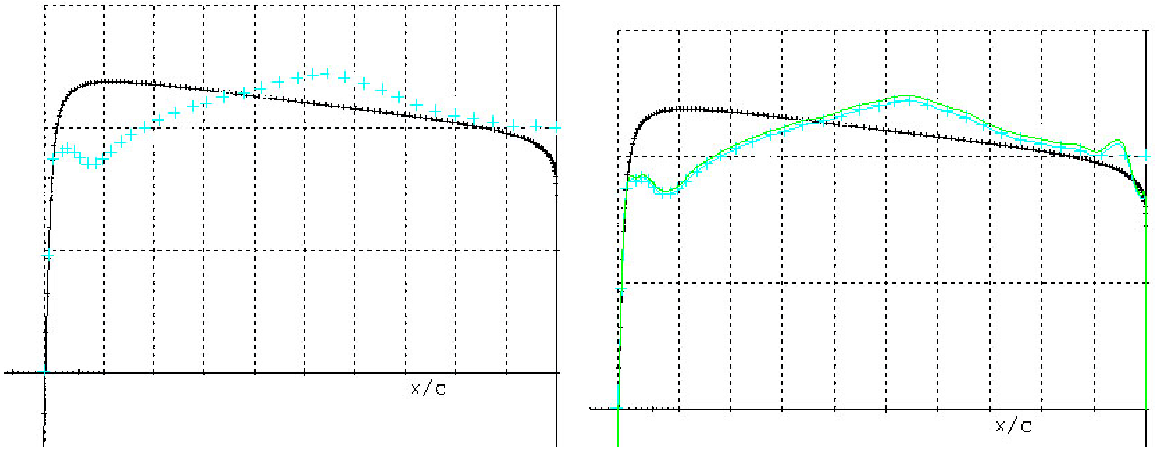

(a) (b)

Figure B.1: Modifying the velocity curve for the NACA 0012 in XFoil

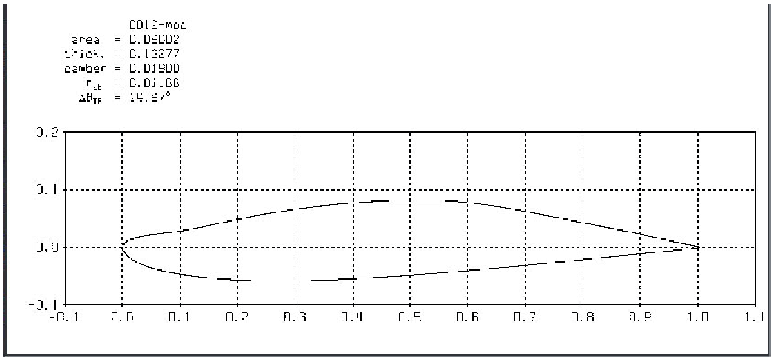

Figure B.2: Airfoil geometry generated by inverse calculation in XFoil

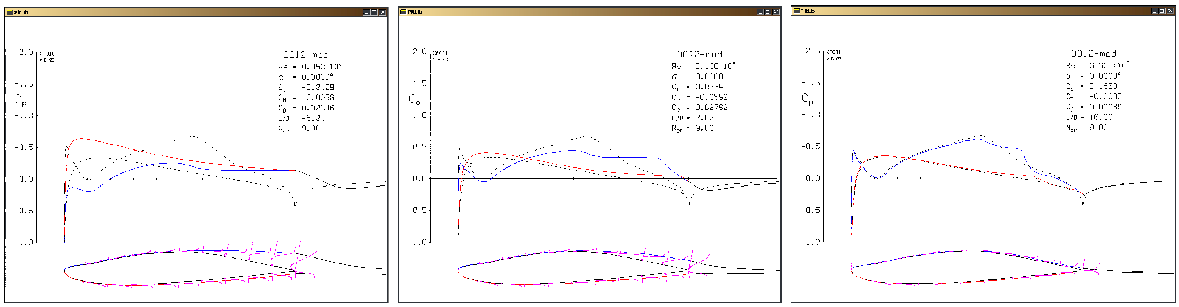

(a) $Re = 5 \cdot 10^4$, $n_{\text{crit}} = 9.0$ (b) $Re = 10 \cdot 10^4$, $n_{\text{crit}} = 9.0$ (c) $Re = 30 \cdot 10^4$, $n_{\text{crit}} = 9.0$

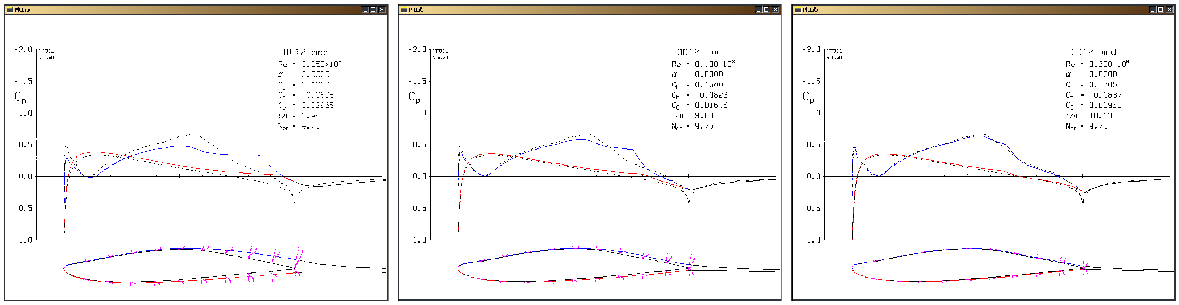

(d) $Re = 5 \cdot 10^4$, $n_{\text{crit}} = 4.75$ (e) $Re = 10 \cdot 10^4$, $n_{\text{crit}} = 4.75$ (f) $Re = 30 \cdot 10^4$, $n_{\text{crit}} = 4.75$

Figure B.3: Predicted pressure coefficients and boundary layer profiles for various Re, n_{crit}

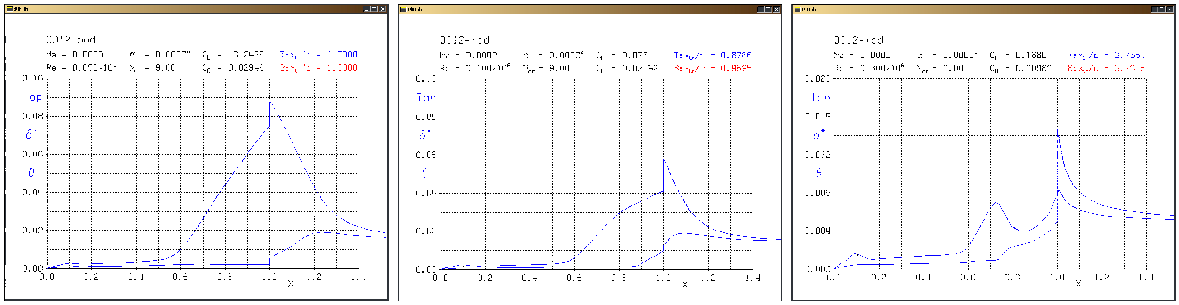

(a) $Re = 5 \cdot 10^4$, $n_{\text{crit}} = 9.00$ (b) $Re = 10 \cdot 10^4$, $n_{\text{crit}} = 9.00$ (c) $Re = 30 \cdot 10^4$, $n_{\text{crit}} = 9.00$

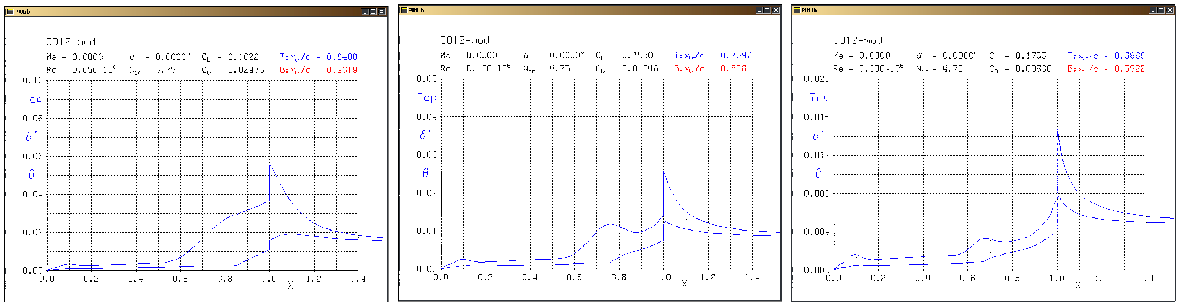

(d) $Re = 5 \cdot 10^4$, $n_{\text{crit}} = 4.75$ (e) $Re = 10 \cdot 10^4$, $n_{\text{crit}} = 4.75$ (f) $Re = 30 \cdot 10^4$, $n_{\text{crit}} = 4.75$

Figure B.4: Predicted displacement and momentum thicknesses for various Re, n_{crit}

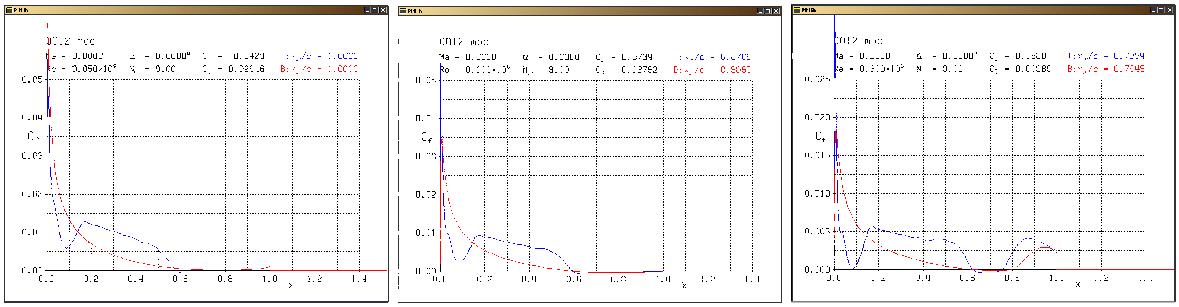

(a) $Re = 5 \cdot 10^4$, $n_{\text{crit}} = 9.00$ (b) $Re = 10 \cdot 10^4$, $n_{\text{crit}} = 9.00$ (c) $Re = 30 \cdot 10^4$, $n_{\text{crit}} = 9.00$

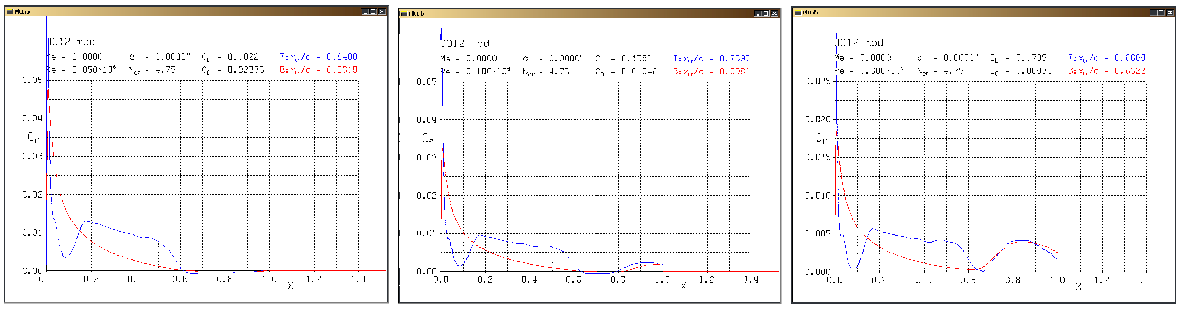

(d) $Re = 5 \cdot 10^4$, $n_{\text{crit}} = 4.75$ (e) $Re = 10 \cdot 10^4$, $n_{\text{crit}} = 4.75$ (f) $Re = 30 \cdot 10^4$, $n_{\text{crit}} = 4.75$

Figure B.5: Predicted skin friction coefficient for various Re, n_{crit}

Appendix C

MATLAB Scripts and Input Files

C.1 MATLAB Scripts

The following MATLAB scripts were used in the processing of the output data. The first script modified the raw mask generated with the XCap frame grabber in order to obtain 8-bit mask files to be used in WaLPT. This script also outputs the coordinates of the points on the blade boundary for later use in determining normal vectors at various locations on the suction surface. The initial post-processing script reads the WaLPT output files and generates the fields plots of vorticity, velocity, and RFP. The profile extraction script reads the curve data from the mask script and the WaLPT output files to determine the velocity profiles at a variable number of stations along the blade surface for the component of velocity parallel to the blade. Similarly, the parallel components of RMS velocity and vorticity are plotted on variable local normals along the blade surface. Also included is a sample WaLPT input file [15].

C.1.1 Mask Generation

```
%FIRST MASK
function turb_mask(run);
run=int2str(run);
path=strcat('f:\blades\piv\masks\');
rawmask=strcat(path,'mask',run,'-raw.bin');
maskfile=strcat(path,'mask',run,'-8bit.bin');
curvefile=strcat(path,'curve',run,'-8bit.bin');

nxc=1008;
nyc=1018;

% load 10 bit xcap image as 16 bit image
fid=fopen(rawmask,'r');
```

```
mask=fread(fid,[nxc,nyc],'int16');
st=fclose(fid);

% display raw image
figure(1);
colormap(gray);
imagesc(mask),axis off,title('raw image  nyc ->');

% set values in array to floor and ceiling of the raw xcap image
for i=1:nxc;
    for j=1:nyc;
        if mask(i,j)>250;
            mask(i,j)=255;
        else
            mask(i,j)=0;
        end
    end
end

% display floored image
figure(2);
colormap(gray);
imagesc(mask),axis off,title('floored image'),axis equal;

% check orientation
% for i=1:30,
%     for j=1:100,
%         mask(i,j)=255;
%     end
% end

% find blade edge and fill above it

paint=0;
for i=1:nxc;
    for j=1:nyc;
        if paint==1;
            mask(i,j)=0;
        end
        if mask(i,j)==0;
            paint=1;
        end
    end
    paint=0;
end

paint=0;
for j=1:nyc;
    for i=nxc:-1:nxc/2;
        if paint==1;
            mask(i,j)=0;
        end
```

```
        if mask(i,j)==0;
            paint=1;
        end
    end
    paint=0;
end

paint=0;
for j=1:nyc;
    for i=1:nxc/2;
        if paint==1;
            mask(i,j)=0;
        end
        if mask(i,j)==0;
            paint=1;
        end
    end
    paint=0;
end

%save the mask file
fid=fopen(maskfile,'w');
fwrite(fid,mask,'int8');
st=fclose(fid);

% display mask
figure(3);
colormap(gray);
imagesc(mask),axis off,title('mask image');

% clean up the curve of the blade wall
paint=0;
for i=1:nxc;
    for j=1:nyc;
        if paint==1;
            mask(i,j)=255;
        end
        if mask(i,j)==0;
            paint=1;
        end
    end
    paint=0;
 end

%save the curve file
fid=fopen(curvefile,'w');
fwrite(fid,mask,'int8');
st=fclose(fid);

% display curve
figure(4);
colormap(gray);
```

```
imagesc(mask),axis off,title('curve image');
```

C.1.2 Initial Post-processing

```
function turbine_piv
% program to average mining data sets

ntot=112;   %number of tensor files
set=30; % data set (Re)
reg=1; % region (1,2,3)
cdn=1; % condition: 1=clean, 2=grid at 7.5, 3=grid at 15

%set condition string
if cdn==1,
    cdnstr='cln';
elseif cdn==2,
    cdnstr='75';
elseif cdn==3,
    cdnstr='15';
end

%set base path of files
basepath=strcat('f:\blades\piv\tensors\',int2str(set),'\',cdnstr);
matfile=strcat('f:\blades\piv\matfiles\mat',int2str(set),'-',int2str(reg),'-',cdnstr,'.mat');

%conversion info - spatial and temporal scales to give units in cm/s
scale=216  %pixels/cm
if set >= 100,
    pulse=10;  %pulse timer in microseconds for high Re cases
else
    pulse=100; %pulse timer in microseconds for low Re cases
end

%conversion factors to cm/s
convel=(scale*pulse/1000000);
convor=(pulse/1000000);

%check image

%check array size
k=1; [ny,nx]=tensfunc2(set,reg,cdn,k,basepath);
%set size of arrays
%nx=83;ny=82;
%create empty arrays
uav=zeros(ntot,nx,ny);
vav=zeros(ntot,nx,ny);
vortav=zeros(ntot,nx,ny);
contav=zeros(ntot,nx,ny);
un=zeros(nx,ny);
vn=zeros(nx,ny);
vorn=zeros(nx,ny);
```

```
conn=zeros(nx,ny);
corn=zeros(nx,ny);
ctr=zeros(nx,ny);
sep=zeros(nx,ny);
urms=zeros(nx,ny);
dvdxn=zeros(1,ny);

%characteristic velocity based on 5400 fpm (~30 m/s)
uf=30;

%read in data files
for i=1:ntot,
   % i=38;
   [u,v,vort,cont,corr,dvdx]=tensfunc(set,reg,cdn,i,basepath);
   un=u+un;
   vn=v+vn;
   vorn=vort+vorn;
   conn=cont+conn;
   corn=corr+corn;
   uav(i,:,:)=u;
   vav(i,:,:)=v;
   vortav(i,:,:)=vort;
   contav(i,:,:)=cont;
   dvdxn=dvdxn+dvdx(nx,:);
   neg_pixels=0;
   for j=1:nx
      for k=1:ny
         if u(j,k) < 0,
            neg_pixels=neg_pixels+1;
            ctr(j,k)=ctr(j,k)+1;
         end
      end
   end
   % calculate the area of the region of separation in camera view (grid)
   total_size=size(u);
   long=total_size(1);
   wide=total_size(2);
   total_area=long*wide;
   fract_neg_area(i)=neg_pixels/total_area;

   % determine the point of separation

   % eliminate values nearest blade surface
   for kk=1:ny
      flag=0;
      for k=nx:-1:1
         if u(k,kk)~=0
            if flag==0
               u(k,kk)=0;
            end
            flag=1;
         end
```

```
      end
   end
   exit=0;
   sep_point_d(i)=0;
   sep_point_o(i)=0;
   for over=47:ny,
      for down=40:nx,
         if u(down,over)<0 & exit==0,
            sep(down,over)=0;
            sep_point_d(i)=down;
            sep_point_o(i)=over;
            exit=1;
         else
            sep(down,over)=255;
         end
      end
   end
end

%%%%%%%%%%%%%% PROCESSING %%%%%%%%%%%%%%%%%%%

%set edge regions to zero if need be
un(:,1)=0; vn(:,1)=0; vorn(:,1)=0; ctr(:,1)=0;
un(:,2)=0; vn(:,2)=0; vorn(:,2)=0;
un(1,:)=0; vn(1,:)=0; vorn(1,:)=0;
un(:,ny-1)=0; vn(:,ny-1)=0; vorn(:,ny-1)=0;
un(:,ny)=0; vn(:,ny)=0; vorn(:,ny)=0;

% eliminate values nearest blade surface
for kk=1:ny
    flag=0;
    for k=nx:-1:1
        if un(k,kk)~=0
            %k,kk
            if flag==0
                un(k,kk)=0;
                vn(k,kk)=0;
                ctr(k,kk)=0;
            end
            flag=1;
        end
    end
end

% for the 1st camera view, need more clean-up at blade wall
if reg==1,
    for kk=1:ny/2
        flag=0;
        for k=nx:-1:1
            if un(k,kk)~=0
                %k,kk
                if flag==0
```

```
                    un(k,kk)=0;
                    vn(k,kk)=0;
                    ctr(k,kk)=0;
                end
                flag=1;
            end
        end
    end
end

%calculate averages
un=un/ntot;
vn=vn/ntot;
vorn=vorn/ntot;
conn=conn/ntot;
corn=corn/ntot;
dvdxn=dvdxn/ntot;
ctr=ctr/ntot;

%scale data
un=un/convel;
vn=vn/convel;
vorn=vorn/convor;

%calculate Re based on average velocity
%REDO FOR TURBINE BLADE, BASE ON VELOCITY MAG and SSL TO COMPARE WITH RE ABOVE
umean=mean(mean(un(:,:)));
re=umean*15.24/0.151;
fprintf('\n Approximated average u velocity is
%6.2f cm/s\n Re based on this is %5.0f\n',umean,re);

% play with FFT
% ctf=fft2(un);
% size(ctf);
% nfft=length(ctf);
% power=abs(ctf(1:nfft/2)).^2;
% freq=(1:nfft/2)/(nfft/2)*0.5;

%plot(ctf,'ro')
%plot(1./freq,power)

fprintf('\nThinking....')

%calculate rms turbulence
for j=1:nx
    fprintf('.')
    for k=1:ny
        dum1=0; dum2=0; dum3=0;
        for i=1:ntot
            dum1=sqrt(un(j,k)^2+vn(j,k)^2);
            dum2=sqrt(uav(i,j,k)^2+vav(i,j,k)^2);
            dum3=(dum1-dum2)^2+dum3;
```

```
        end
        urms(j,k)=sqrt(dum3)/ntot;
    end
end

%skin friction coef.
mu=0.0000185;
shear=mu*dvdxn;
cf=shear/(0.5*1.23*uf^2);
%cf=cf(1,12:82);
%size(cf)

%% PLOTTING

offset=-10;
xllim=offset;
yllim=offset;
xulim=nx-offset;
yulim=ny-(offset);
%yllim=20;
%yulim=50;

%new colormap
jet2=abs(jet-1);

mag=sqrt(un.^2+vn.^2);
%mag=un;

%vertices for patch command for slab (if needed)
xc=9; yc=27;
x=[1 81 81 xc xc 1];
y=[45 45 40 40 yc yc];

%% PLOTS
figure(1);
colormap jet;
contourf(mag,20),axis equal,axis([xllim xulim yllim yulim]),
title('Velocity & Velocity Magnitude'),axis ij,shading flat;
colorbar; %gtext('m/s');
hold on;
quiver(un,vn,5,'w'),axis equal,axis([xllim xulim yllim yulim]),axis ij
hold off;

figure(2);
colormap jet;
contourf(vorn,50),axis off, axis equal,axis([xllim xulim yllim yulim]),
title('Vorticity'),axis ij,shading flat;
colorbar; %gtext('s^{-1}');

%vort_flow=strcat('f:\blades\piv\figs\vort',int2str(set),'-',int2str(reg),'-',cdnstr,'.eps');
%print('-depsc',vort_flow)
```

```
figure(3);
colormap jet;
contourf(ctr,50),axis off,axis equal,axis([xllim xulim yllim yulim]),
title('Reverse Flow Probability (Flow Direction \rightarrow)'),axis ij;,shading flat;
colorbar;
%patch(x,y,'k');

%rev_flow=strcat('f:\blades\piv\figs\rev',int2str(set),'-',int2str(reg),'-',cdnstr,'.eps');
%print('-depsc',rev_flow)

figure(4);
colormap jet;
contourf(urms,50),axis off, axis equal,axis([xllim+2 xulim-2 yllim yulim]),title('RMS Velocity
Variation'),axis ij;,shading flat;
colorbar;
%patch(x,y,'k');

figure(5);
colormap jet;
contourf(conn,50),axis off, axis equal,axis([xllim xulim yllim yulim]),
title('Continuity (as a check of 3-D effects): Run 4'),axis ij,shading flat;
colorbar;

figure(6);
colormap jet;
contourf(corn,[0 .1 .2 .3 .4 .5 .6 .7 .8 .9 1.0]),axis off,
axis equal,axis([xllim xulim yllim yulim]),
title('Average PIV Correlation: Run 4'),axis ij;
colorbar;

figure(7);
colormap jet;
quiver(un,vn,5),axis equal,axis([xllim xulim yllim yulim]),title('Velocity'),axis ij

%vec_flow=strcat('f:\blades\piv\figs\vec',int2str(set),'-',int2str(reg),'-',cdnstr,'.eps');
%print('-depsc',vec_flow)


% x = [0 53 0];
% y = [21 0 0];
% patch(x,y,'k');
% x = [60  60 0 0];
% y = [60 42 34 60];
% patch(x,y,'k');
% hold off;

%skin friction plot
%walldist=linspace(0,1,ny);
%figure(7);
%plot(walldist,cf,'md')%,axis([-0.2 5.6 -0.015 0.01]);%,axis ij;
%ylabel('Cf');
%xlabel('N');
```

```
uso=15;

walldist=linspace(0,1,nx);
figure(8);
plot(un(:,10),walldist,'kx-'),axis ij;%,axis([-0.2 5.6 -0.015 0.01]);%,axis ij;
ylabel('velocity profile');
xlabel('Downstream Distance'); title('Velocity Profiles');
hold on;
plot(un(:,20)+uso,walldist,'bx-')
plot(un(:,30)+2*uso,walldist,'kx-');
plot(un(:,40)+3*uso,walldist,'bx-');
plot(un(:,50)+4*uso,walldist,'kx-');
plot(un(:,60)+5*uso,walldist,'bx-');
%plot(un(:,70)+6*uso,walldist,'kx-');
grid on;
hold off;

figure(9);colormap gray;
image(sep),axis equal;
ylabel('Flow Region');
xlabel('Downstream Distance'); title('Separation Points');

% output all variables in workspace
fprintf('saving all variables in workspace...');
save(matfile);

return;
%end of main routine

%%%
```

```
    bat=strcat('.00',bat);
else
    if batch < 100
        bat=strcat('.0',bat);
    else
        bat=strcat('.',bat);
    end
end

%set condition string
if cdn==1
    cdnstr='cln';
elseif cdn==2
    cdnstr='75';
elseif cdn==3
    cdnstr='15';
end

%set tensor file name
lptfile=strcat('tensor',set,'-',reg,'-',cdnstr,bat);

%SET PATHS AND FILE NAMES
path=strcat(basepath,'\');
rdfile=strcat(path,lptfile);

% read data file into header and tensor arrays

fprintf(' Reading single tensor file %s in %s\n',lptfile,path)

fid=fopen(rdfile,'r');
header=fread(fid,64,'int16');
version=header(1);                % walpt version number (starting with 300)
nxc =header( 2) ; nyc =header( 3); % camera size
nxuv=header( 4) ; nyuv=header( 5); % velocity array size
nxw =header( 6) ; nyw =header( 7); % window sizes in pixels
nxs =header( 8) ; nys =header( 9); % step sizes in pixels
nxf =header(10) ; nyf =header(11); % flow region size in pixels
xf  =header(12) ; yf  =header(13); % flow region offset in pixels
nbits=header(14);                 % pixel depth of original flow images
% utensor=[nxuv,nyuv,7]
% read tensor components from file in succession
e1=fread(fid,[nxuv,nyuv],'float'); % u
e2=fread(fid,[nxuv,nyuv],'float'); % v
e3=fread(fid,[nxuv,nyuv],'float'); % du/dx
e4=fread(fid,[nxuv,nyuv],'float'); % dv/dx
e5=fread(fid,[nxuv,nyuv],'float'); % du/dy
e6=fread(fid,[nxuv,nyuv],'float'); % dv/dy
e7=fread(fid,[nxuv,nyuv],'float'); % correlation
st=fclose(fid);

%rotate fields
e1=e1.';
```

```
e2=e2.';
e3=e3.';
e4=e4.';
e5=e5.';
e6=e6.';
e7=e7.';

% Check and replace the "missing" 1000 in velocity
% fields with zeros (option XXXX in walpt).
% (This option is for use with IDL or similar programs.)

for i=1:nyuv
    for j=1:nxuv
        if e1(i,j) > 999
            e1(i,j) = 0;
        end
        if e2(i,j) > 999
            e2(i,j) = 0;
        end
    end
end

%Items to return
corr=e7;

% Calculate vorticity,continuity

vorticity=e5-e4;    %du/dy-dv/dx
continuity=e3+e6;   %du/dx+dv/dy

%return velocity gradient for wall skin friction calculation
%(in this case, dv/dx)

dvdx=e4;

return

%%%%%%%%%%%%%%%%%%%%%%%%%%%%%%%%%%%%%%%%%%%%%%%%%%%%%%%%%%%%%%%%%%%%%%%%%%%%%%%

function [nx,ny]=tensfunc2(set,reg,cdn,batch,basepath)
%reads tensor file and returns array size

set=int2str(set);
reg=int2str(reg);
bat=int2str(batch);

% file and path names

%set extension
if batch < 10
    bat=strcat('.00',bat);
else
```

```
    if batch < 100
        bat=strcat('.0',bat);
    else
        bat=strcat('.',bat);
    end
end

%set condition string
if cdn==1
    cdnstr='cln'
elseif cdn==2
    cdnstr='75'
elseif cdn==3
    cdnstr='15'
end

%set tensor file name
lptfile=strcat('tensor',set,'-',reg,'-',cdnstr,bat);

%SET PATHS AND FILE NAMES
path=strcat(basepath,'\');
rdfile=strcat(path,lptfile);
lptima1=strcat('image1.lpt');lptima2=strcat('image2.lpt');
imfile1=strcat(path,'image','1-',reg,'-',cdnstr,'.lpt')
imfile2=strcat(path,'image','2-',reg,'-',cdnstr,'.lpt');
%imfile2=strcat(path,lptima2);

% read data file into header and tensor arrays

fprintf(' Reading tensor file %s in %s to determine array size\n',lptfile,path)

fid=fopen(rdfile,'r');
header=fread(fid,64,'int16');
version=header(1);                % walpt version number (starting with 300)
nxc =header( 2) ; nyc =header( 3); % camera size
nxuv=header( 4) ; nyuv=header( 5); % velocity array size
nxw =header( 6) ; nyw =header( 7); % window sizes in pixels
nxs =header( 8) ; nys =header( 9); % step sizes in pixels
nxf =header(10) ; nyf =header(11); % flow region size in pixels
xf  =header(12) ; yf  =header(13); % flow region offset in pixels
nbits=header(14);                 % pixel depth of original flow images
% utensor=[nxuv,nyuv,7]
% read tensor components from file in succession
e1=fread(fid,[nxuv,nyuv],'float'); % u
e2=fread(fid,[nxuv,nyuv],'float'); % v
e3=fread(fid,[nxuv,nyuv],'float'); % du/dx
e4=fread(fid,[nxuv,nyuv],'float'); % dv/dx
e5=fread(fid,[nxuv,nyuv],'float'); % du/dy
e6=fread(fid,[nxuv,nyuv],'float'); % dv/dy
e7=fread(fid,[nxuv,nyuv],'float'); % correlation
st=fclose(fid);
```

```
nx=nxuv;
ny=nyuv;

%open up image to check IPX routine
% fid=fopen(imfile1,'r');
% image1=fread(fid,[nxc,nyc],'int16');
% st=fclose(fid);
% fid=fopen(imfile2,'r');
% image2=fread(fid,[nxc,nyc],'int16');
% st=fclose(fid);

% 'ticker'
% figure(10);shg;newplot;
% colormap(hot) %also try gray
% imagesc(image1.'),axis off,axis equal
% figure(11);shg;newplot;
% colormap(gray)
% imagesc(image2.'),axis off,axis equal

return
```

C.1.3 Profile Extraction

```
% interpolation of velocity profile
function turbine_profiles(go);
% check normals and set go=1 when you want to interpolate and plot profiles
%  ************************************************************************
% ****** find perpendicular lines for interpolation of velocity profile *******
%  ************************************************************************
   spacing=60;                 % how many pixels (horiz) between each normal line?
   lines=15;                   % how many normal lines?
    firstline=4;      % choose which lines to plot
    lastline=13;
    u_cutoff=10;          % what %SSL to plot up to for each plot
    v_cutoff=10;
    rms_cutoff=10;
    vort_cutoff=10;
            u_step=1;    % %SSL in between each profile plotted
            %v_step=0.35;
    rms_step=40;
    vort_step=700;

    rey=30; % data set (Re)
    reg=2; % region (1,2,3)
    cdn=1; % condition: 1=clean, 2=grid at 7.5, 3=grid at 15
    if reg==3,
        spacing=57;
        lines=15;
        firstline=3;
        lastline=12;
    end
```

```
% set condition string
if cdn==1
    cdnstr='cln';
elseif cdn==2
    cdnstr='75';
elseif cdn==3
    cdnstr='15';
end

maskpath='f:\blades\piv\masks\';
tenpath=strcat('f:\blades\piv\tensors\',int2str(rey),'\',cdnstr,'\');
normpath=strcat('f:\blades\piv\profiles\');
rdfile=strcat(tenpath,'tensor',int2str(rey),'-',int2str(reg),'-',cdnstr,'.001');

if cdn==1 & reg==1 & rey==30,
    curvefile=strcat(maskpath,'curve',int2str(reg),'-cln-8bit.bin');
    normalimage=strcat(normpath,'norm',int2str(reg),'-cln-8bit.bin');
    coords_x=strcat(normpath,'normal_x-',int2str(reg),'-cln.txt');
    coords_y=strcat(normpath,'normal_y-',int2str(reg),'-cln.txt');
    coords_n=strcat(normpath,'num-pts-',int2str(reg),'-cln.txt');
    alpha=strcat(normpath,'alpha-',int2str(reg),'-cln.txt');
    norm_length=strcat(normpath,'length-',int2str(reg),'-cln.txt');
elseif cdn==1 & reg==1 & rey==50,
    curvefile=strcat(maskpath,'curve',int2str(reg),'-cln-8bit.bin');
    normalimage=strcat(normpath,'norm',int2str(reg),'-cln-8bit.bin');
    coords_x=strcat(normpath,'normal_x-',int2str(reg),'-cln.txt');
    coords_y=strcat(normpath,'normal_y-',int2str(reg),'-cln.txt');
    coords_n=strcat(normpath,'num-pts-',int2str(reg),'-cln.txt');
    alpha=strcat(normpath,'alpha-',int2str(reg),'-cln.txt');
    norm_length=strcat(normpath,'length-',int2str(reg),'-cln.txt');
else
    curvefile=strcat(maskpath,'curve',int2str(reg),'-8bit.bin');
    normalimage=strcat(normpath,'norm',int2str(reg),'-8bit.bin');
    coords_x=strcat(normpath,'normal_x-',int2str(reg),'.txt');
    coords_y=strcat(normpath,'normal_y-',int2str(reg),'.txt');
    coords_n=strcat(normpath,'num-pts-',int2str(reg),'.txt');
    norm_length=strcat(normpath,'length-',int2str(reg),'.txt');
    alpha=strcat(normpath,'alpha-',int2str(reg),'.txt');
end

% read in the important variables from the tensor file
fid=fopen(rdfile,'r');
header=fread(fid,64,'int16');
nxc =header( 2); nyc =header( 3); % camera size
nxuv=header( 4); nyuv=header( 5); % velocity array size
nxw =header( 6); nyw =header( 7); % window sizes in pixels
nxs =header( 8); nys =header( 9); % step sizes in pixels
nxf =header(10); nyf =header(11); % flow region size in pixels
xf  =header(12); yf  =header(13); % flow region offset in pixels
st=fclose(fid);
```

```
    % load mask image
    fid=fopen(curvefile,'r');
    curvearray=fread(fid,[nxc,nyc],'uint8');
    st=fclose(fid);

    % determine the indices and slope at each local origin
    [normarray]=origins(curvearray,spacing,nxf,nyf,nxw,nyw,xf,yf,lines,coords_x,
coords_y,coords_n,alpha,rey,norm_length);

    % save normal image
    fid=fopen(normalimage,'w');
    fwrite(fid,normarray,'uint8');
    st=fclose(fid);

    % display curve with normal lines
    figure(1);
    imagesc(normarray.'),colormap(summer),axis on,axis equal,title('curve with normals');

    %  ***************************************************************************
    % ********* this routine finds and plots the profiles for the normals *********
    %  ***************************************************************************
    if go==1;
        %clf
        fprintf('\nReading...')
        Re=rey*1000; %based on suction surface length
        nu=1.51E-5;  %for tunnel
        SSL=0.1524;  %blade suction surface length in meters

        % conversion info - spatial and temporal scales to give units in m/s
        scale=216.22;    %pixels/cm for camera view
        if rey>50,
            pulse=10;    %pulse timer in microseconds
        else
            pulse=100;
        end

        SSLp=SSL*100*scale;   % SSL in pixels

        % conversion factors to m/s
        %convel=(scale*100*pulse/1000000);
        u_exit=Re*nu/SSL;  %m/s

        rpath1=strcat('f:\blades\piv\tensors\',int2str(rey),'\',cdnstr,'\');
        rpath2=strcat('f:\blades\piv\profiles\');
        matpath='f:\blades\piv\matfiles\';
        wpath=strcat('f:\blades\piv\profiles\');
        if cdn==1 & reg==1 & rey==30,
            coords_x=strcat(rpath2,'normal_x-',int2str(reg),'-cln.txt');
            coords_y=strcat(rpath2,'normal_y-',int2str(reg),'-cln.txt');
            coords_n=strcat(rpath2,'num-pts-',int2str(reg),'-cln.txt');
            alpha=strcat(rpath2,'alpha-',int2str(reg),'-cln.txt');
            norm_len=strcat(rpath2,'length-',int2str(reg),'-cln.txt');
```

```
elseif cdn==1 & reg==1 & rey==50,
    coords_x=strcat(rpath2,'normal_x-',int2str(reg),'-cln.txt');
    coords_y=strcat(rpath2,'normal_y-',int2str(reg),'-cln.txt');
    coords_n=strcat(rpath2,'num-pts-',int2str(reg),'-cln.txt');
    alpha=strcat(rpath2,'alpha-',int2str(reg),'-cln.txt');
    norm_len=strcat(rpath2,'length-',int2str(reg),'-cln.txt');
else
    coords_x=strcat(rpath2,'normal_x-',int2str(reg),'.txt');
    coords_y=strcat(rpath2,'normal_y-',int2str(reg),'.txt');
    coords_n=strcat(rpath2,'num-pts-',int2str(reg),'.txt');
    alpha=strcat(rpath2,'alpha-',int2str(reg),'.txt');
    norm_len=strcat(rpath2,'length-',int2str(reg),'.txt');
end
matfile=strcat(matpath,'mat',int2str(rey),'-',int2str(reg),'-',cdnstr,'.mat');
u_profile=strcat(wpath,'u_profile',int2str(rey),'-',int2str(reg),'-',cdnstr,'.txt');
v_profile=strcat(wpath,'v_profile',int2str(rey),'-',int2str(reg),'-',cdnstr,'.txt');
separation=strcat(wpath,'separation.txt');
fract=strcat(wpath,'fraction',int2str(rey),'-',int2str(reg),'-',cdnstr,'.txt');
rdfile=strcat(rpath1,'tensor',int2str(rey),'-',int2str(reg),'-',cdnstr,'.001');

% read in the important variables from the tensor file
fid=fopen(rdfile,'r');
header=fread(fid,64,'int16');
nxc =header( 2); nyc =header( 3); % camera size
nxuv=header( 4); nyuv=header( 5); % velocity array size
nxw =header( 6); nyw =header( 7); % window sizes in pixels
nxs =header( 8); nys =header( 9); % step sizes in pixels
nxf =header(10); nyf =header(11); % flow region size in pixels
xf  =header(12); yf  =header(13); % flow region offset in pixels
st=fclose(fid);

% read in averaged arrays (transposed!?) and areas for the run and scale to m/s
load(matfile,'un','vn','urms','vorn','ctr','fract_neg_area');
if reg==1,
    load(matfile,'sep_point_d','sep_point_o');
end
un=un.'/100;
vn=vn.'/100;

% read in the number and coords of points for each normal line in the flow region
pts=textread(coords_n,'%u\n');
xs=textread(coords_x,'%u\n');
ys=textread(coords_y,'%u\n');
a=textread(alpha,'%f\n');
len=textread(norm_len,'%u\n');

fprintf('\nInterpolating...')
% size of interpolated array
scale_x=(nxf-nxw)/nxuv;
scale_y=(nyf-nyw)/nyuv;
y_array=((1:(nyf-nyw)).')/scale_x;
x_array=(1:(nxf-nxw))/scale_y;
```

```
        % determine the point of separation from view #1
%         if reg==1,
%             fidsep=fopen(separation,'w+');
%             fprintf(fidsep,'Separation info for region-%1.0f rey-%3.0f grid-%s',reg,rey,cdnstr);
%             fprintf(fidsep,'\n   Location of separation point is %3.0fx
% 3.0fy',mean(sep_point_d),mean(sep_point_o));
%             fprintf(fidsep,'\n   Deviation of separation point is %3.0fx
% 3.0fy',std(sep_point_d),std(sep_point_o));
%             % calculate the average area of the separation region and how much it varies
%             total_area=length(x_array)*length(y_array);% num pixels in grid
%             sep_area=fract_neg_area*total_area/(scale^2);  % num of neg pixels conv to sq cm
%             fprintf(fidsep,'\n   Average size of separation region in square cm is
% 5.2f',mean(sep_area));
%             fprintf(fidsep,'\n   Standard deviation of size of separation region is
% 5.2f',std(sep_area));
%             st=fclose(fidsep);
%         end

        % interpolate the velocity components for each pixel in the tensor plot area
        u=interp2(un,y_array,x_array);
        v=interp2(vn,y_array,x_array);
        rms_int=interp2(urms.',y_array,x_array);
        vort_int=interp2(vorn.',y_array,x_array);

%         fidu=fopen(u_profile,'w');
%         fidf=fopen(fract,'w');
%         fidv=fopen(v_profile,'w');

        % extract the values of u and v at the pts on the normals
        last_j=0;
        fprintf('\nMaking profiles...')
        for i=1:length(pts);
%             fprintf(fidu,'%s %3.0f\n','*******line',i);
%             fprintf(fidv,'%s %3.0f\n','*******line',i);
            fraction=zeros(1,max(pts));
            u_temp=zeros(1,max(pts));
            v_temp=zeros(1,max(pts));
            rms_temp=zeros(1,max(pts));
            vort_temp=zeros(1,max(pts));
            for j=1:pts(i);
                next_j=last_j+j;
                fraction(j)=100*(len(i)/pts(i))*j/SSLp;
                u_temp(j)=(u(xs(next_j),ys(next_j)))*sin(a(i))+(v(xs(next_j),
ys(next_j))*cos(a(i)));
                v_temp(j)=(u(xs(next_j),ys(next_j)))*cos(a(i))+(v(xs(next_j),
ys(next_j))*sin(a(i)));
                rms_temp(j)=rms_int(xs(next_j),ys(next_j));
                vort_temp(j)=vort_int(xs(next_j),ys(next_j));
                if a(i)<0,
                    v_temp(j)=-v_temp(j);
                    u_temp(j)=-u_temp(j);
```

```
    end
end

% non-dimensionalize the tangential and normal velocity magnitudes
u_scale=u_temp/u_exit;
v_scale=v_temp/u_exit;

% trim the lines to plotted height (%SSL)
length(u_scale);
for k=1:length(u_scale),
    if fraction(k)<=u_cutoff,
        u_trim(k)=u_scale(k);
        fract_trim(k)=fraction(k);
    else
        u_trim(k)=0;
        fract_trim(k)=0;
    end
end

length(v_scale);
for gg=1:length(v_scale),
    if fraction(gg)<=v_cutoff,
        v_trim(gg)=v_scale(gg);
        fract_trim(gg)=fraction(gg);
    else
        v_trim(gg)=0;
        fract_trim(gg)=0;
    end
end

length(rms_temp);
for k=1:length(rms_temp),
    if fraction(k)<=rms_cutoff,
        rms_trim(k)=rms_temp(k);
        fract_trim(k)=fraction(k);
    else
        rms_trim(k)=0;
        fract_trim(k)=0;
    end
end

length(vort_temp);
for k=1:length(vort_temp),
    if fraction(k)<=vort_cutoff,
        vort_trim(k)=vort_temp(k);
        fract_trim(k)=fraction(k);
    else
        vort_trim(k)=0;
        fract_trim(k)=0;
    end
end
```

```
            % plot rms, velocity and vorticity profiles
            if i>=firstline & i<=lastline,
                figure(2);
                plot(rms_trim-rms_step*i,fract_trim,'bv','MarkerSize',3);
                xlabel('RMS');ylabel('% SSL');
                r=gca;
                hold on;
                if i==lastline,
                    hold off;
                end
                figure(3);
                plot(u_trim-u_step*i,fract_trim,'bv','MarkerSize',3);
                xlabel('u/Uexit');ylabel('% SSL');
                rr=gca;
                hold on;
                if i==lastline,
                    hold off;
                end
                figure(4);
                plot(vort_trim-vort_step*i,fract_trim,'bv','MarkerSize',3);
                xlabel('Vorticity');ylabel('% SSL');
                rrr=gca;
                hold on;
                if i==lastline,
                    hold off;
                end
            end
            % output to text file and plot
%             fprintf(fidu,'%6.5f\n',u_trim);
%             fprintf(fidf,'%6.5f\n',fract_trim);
%             fprintf(fidv,'%6.5f\n',v_trim);
            last_j=next_j;
        end
        hold off
        set(r,'XTickLabel','');
        set(rr,'XTickLabel','');
        set(rrr,'XTickLabel','');

        uprofile=strcat(wpath,'u_profile',int2str(rey),'-',
int2str(reg),'-',cdnstr,'.eps');
        rms_profile=strcat(wpath,'rms_profile',int2str(rey),'-',
int2str(reg),'-',cdnstr,'.eps');
        vort_profile=strcat(wpath,'vort_profile',int2str(rey),'-',
int2str(reg),'-',cdnstr,'.eps');

        print(3,'-depsc',uprofile);
        print(2,'-depsc',rms_profile);
        print(4,'-depsc',vort_profile);
%         st=fclose(fidu);
%         st=fclose(fidf);
%         st=fclose(fidv)
    end
```

```
%**************  sub functions for normals ****************
% return indices of each local origin based on spacing
function [normals]=origins(curve,d,xf,yf,xw,yw,xo,yo,l,
coordsx,coordsy,coordsn,alp,rn,norm_len);
% find the region processed in pixel space in a frame half of the window size
offset_x=xo+xw/2;
offset_y=yo+yw/2;
end_x=xf+xo-xw/2;
end_y=yf+yo-yw/2;

% find the starting origin
exit_loop=0;
for i=end_x:-1:offset_x;
    for j=end_y:-1:offset_y;
        if exit_loop==0,
            if curve(i,j)==0,
                first_x=i;
                first_y=j;
                exit_loop=1;
            end
        end
    end
end
% find another point a set horizontal distance from this origin
next_x=first_x;
next_y=first_y;

% initialize coordinate output files
fidx=fopen(coordsx,'w');
fidy=fopen(coordsy,'w');
fidn=fopen(coordsn,'w');
fidl=fopen(norm_len,'w');
fida=fopen(alp,'w');

for o=1:l,
    sprintf('%s\n%s\n%s\n%s\n%s%3.0f\n','writing normal coords to',coordsx,
'and',coordsy,'for line',o)
    %fprintf(fidx,'%s%3.0f%s%3.0f%s\n','****** normal_x #',o,
' from the right for run ',rn,' ******');
    %fprintf(fidy,'%s%3.0f%s%3.0f%s\n','****** normal_y #',o,
' from the right for run ',rn,' ******');
    line_x=zeros;
    line_y=zeros;
    i=next_x-(2*d);
    exit_loop=0;
    for j=end_y:-1:offset_y;
        if exit_loop==0,
            if i>0 & j>0,
                if curve(i,j)==0,
                    temp_x=i;
                    temp_y=j;
```

```
                exit_loop=1;
            end
        end
    end
end
% find a unit vector in the direction connecting the origin and temp point
dist=sqrt((next_x-temp_x)^2+(next_y-temp_y)^2);
uvx=(next_x-temp_x)/dist;
uvy=(next_y-temp_y)/dist;

% find point and slope for the next local origin
new_x=fix((uvx*d-next_x)*-1);
new_y=fix((uvy*d-next_y)*-1);
origin_x(o)=new_x;
origin_y(o)=new_y;
m(o)=-uvx/uvy;
alpha(o)=atan(uvx/uvy);
alphadeg(o)=alpha(o)*180/pi;
next_x=new_x;
next_y=new_y;

% find a line perpendicular to the blade surface from origin
exit_loop=0;
if m(o)<0 & abs(alphadeg(o))<87,
    for i=new_x:end_x;
        if exit_loop==0;
            x=i-new_x;
            j=new_y+fix(x*m(o));
            if j<end_y & j>offset_y & i<end_y & i>offset_x,
                curve(i,j)=0;
                line_x(x+1)=i-offset_x;
                line_y(x+1)=j-offset_y;
                lasti=i;
                lastj=j;
            else
                exit_loop=1;
            end
        end
    end
elseif m(o)>0 & abs(alphadeg(o))<87,
    for i=new_x:-1:offset_x;
        if exit_loop==0;
            x=i-new_x;
            j=new_y+fix(x*m(o));
            if j<end_y & j>offset_y & i>0 & i<end_y & i>offset_x,
                curve(i,j)=0;
                line_x(1-x)=i-offset_x;
                line_y(1-x)=j-offset_y;
                lasti=i;
                lastj=j;
            else
                exit_loop=1;
```

```
                end
            end
        end
    elseif abs(alphadeg(o))>87,
        for c=1:200;
            if exit_loop==0;
                x=c;
                i=new_x;
                j=new_y-4*x;
                if j>offset_y,
                    curve(i,j)=0;
                    line_x(x)=i-offset_x;
                    line_y(x)=j-offset_y;
                    lasti=i;
                    lastj=j;
                else
                    exit_loop=1;
                end
            end
        end
    end
    % calculate the total distance from local origin to last point
    norm_length(o)=sqrt((lasti-next_x)^2+(lastj-next_y)^2);

    % store coords of pts on normals
    num_pts=length(line_x);
    fprintf(fidn,'%5.0f\n',num_pts);
    fprintf(fidx,'%5.0f\n',line_x);
    fprintf(fidy,'%5.0f\n',line_y);
end
fprintf(fidl,'%5.0f\n',norm_length);
fprintf(fida,'%5.5f\n',alpha);
normals=curve;
st=fclose(fidx);
st=fclose(fidy);
st=fclose(fidn);
st=fclose(fidl);
st=fclose(fida);
return
```

C.2 Sample WaLPT Input File

The following is a sample input file used with WaLPT 3.22.

```
lptmode, 0=singlepass, 1=small to large, 2=large to small, 3= LPT
2 1 0 1
input file names ( one line per file )
list30-1-15.lst
tensor30-1-15
image size nxc, nyc, pixr
```

```
1008 1018 16 1.00
flow size, nxf, nyf
1008 1018
flow offset, xf, yf
0 0
window size, nxw, nyw, 2**n
32 32
amod, min, max windows dimensions 2**n, correlaltion level corlvl
1 8  32 0.50
step size, nxs, nys
12 12
window type, wtype 1-7, see source listing
1
peak type, ptype 0=grid,1=parabolic,2=gaussian
2
laundary type, ltype 0=no laundering,1=rejection
1
extension parameter, 0= none, zero padding, 1= smooth (nth order)
1
filter widths (1/) fltrwx,fltrwy; 0= no filtering, 1,2,.. higher ; nfil
10 10 3
wall parameters: nwalls, parex, motion, intflag, outmask
1 1 0 0 1
wall geometry file
c:\blades\PIV\masks\mask1-8bit.bin
motion parameters: dxcg, dycg ,rot
0.00 0.00 0.00
0.00 0.00 0.00
0.00 0.00 0.00
```

Bibliography

[1] G. K. Batchelor, *An Introduction to Fluid Mechanics*, Cambridge University Press, Cambridge, 1990.

[2] S. Batill and T. Mueller. "Visualization of Transition in the Flow Over an Airfoil Using the Smoke Wire Technique." *AIAA Journal,* **19**, pp. 340–345, 1981.

[3] J. W. Baughn, R. J. Butler, A. R. Byerley, and R. B. Rivir. "An Experimental Investigation of Heat Transfer, Transition and Separation on Turbine Blades at Low Reynolds Number and High Turbulence Intensity." *International Mechanical Engineering Congress and Exposition,* San Fransisco, CA, 1995.

[4] D. J. Dorney, J. P. Lake, P. I. King, and D. E. Ashpis. "Experimental and Numerical Investigation of Losses in Low-Pressure Turbine Blade Rows." *AIAA 38th Aerospace Sciences Meeting*, Reno, NV, 2000. Paper 2000-0737.

[5] M. Drela. "XFOIL: An Analysis and Design System for Low Reynolds Number Airfoils." Low Reynolds Number Aerodynamics. T.J. Mueller (Editor). Lecture Notes in Engineering No. 54, Springer Verlag, 1989.

[6] D. E. Halstead, D. C. Wisler, T. H. Okiishi, G. J. Walker, H. P. Hodson, and H.-W. Shin. "Boundary Layer Development in Axial Compressors and Turbines Part 1 of 4: Composite Picture." *International Gas Turbine and Aeroengine Congress and Exposition,* Houston, TX, 1995. Paper 95-GT-461.

[7] D. E. Halstead, D. C. Wisler, T. H. Okiishi, G. J. Walker, H. P. Hodson, and H.-W. Shin. "Boundary Layer Development in Axial Compressors and Turbines Part 3 of 4: LP Turbines." *International Gas Turbine and Aeroengine Congress and Exposition,* Houston, TX, 1995. Paper 95-GT-463.

[8] B. Hollon and J. D. Jacob. "Measurements of Transition and Separation on Low Pressure Turbine Blades." AIAA Paper No. 2001-0447, *39th AIAA Aerospace Sciences Meeting and Exhibit*, Reno, Nevada, January, 2001.

[9] R. E. Mayle. "The Role of Laminar-Turbulent Transition in Gas Turbine Engines." *Journal of Turbomachinery*, **113**, pp. 509–537, 1991.

[10] C. G. Murawski, R. Sondergaard, R. B. Rivir, T. W. Simon, K. Vafai, and R. J. Volino. "Experimental Study of the Unsteady Aerodynamics in a Linear Cascade with Low Reynolds Number Low Pressure Turbine Blades." *ASME International Gas Turbine & Aeroengine Congress & Exhibition*, Orlando, FL, 1997. Paper 97-GT-95

[11] C. G. Murawski, K. Vafai. "Effect of Variable Axial Chord on a Low-Pressure Turbine Blade." *Journal of Propulsion and Power,* **15**, 5, September-October 1999.

[12] S. Qiu and T. W. Simon. "An Experimental Investigation of Transition as Applied to Low Pressure Turbine Suction Surface Flows." *ASME Gas Turbo Expo 97*, Orlando, FL, 1997. Paper 97-GT-455.

[13] H. Schlicting, *Boundary Layer Theory*, McGraw-Hill, New York, 1987.

[14] C. H. Sieverding and P. Van Den Bosche "The Use of Coloured Smoke to Visualize Secondary Flows in a Turbine-Blade Cascade." *Journal of Fluid Mechanics,* **134**, pp/ 85–89, 1983.

[15] M. J. Sholl and Ö Savaş. "A fast Lagrangian PIV Method for Study of General High-Gradient Flows." *AIAA 35th Aerospace Meetings & Exhibits*. AIAA, 1997. Paper 97-0493.

[16] L. Tsuei and Ö Savaş. "Treatment of Interfaces in Particle Image Velocimetry." *Experiments in Fluids*, **29**, pp. 203–214, 2000.

[17] R. J. Volino and L. S. Hultgren. "Measurements in Separated and Transitional Boundary Layers Under Low-Pressure Turbine Airfoil Conditions." *Journal of Turbomachinery,* **123**, pp. 189–197, 2001.

[18] A. D. Young, *Boundary Layers*, AIAA Press, Washington DC, 1989.

Vita

Brian Hollon was born in South Lyon Michigan in 1978. He graduated from Pymatuning Valley High School in 1996 and briefly attended Lakeland Community College and the University of Toledo before attending the University of Kentucky. He received his B.S. in Mechanical Engineering from the University of Kentucky in 2000 before attending graduate school through the University Scholars program. As a graduate student, he served as a Teaching Assistant for EGR 101: Introduction to Engineering. He presented several talks and papers on his research and was a member of Pi Tau Sigma honorary fraternity for mechanical engineers. He released his first album with his band *Relative Frequency* in 2001.